Centrality Dependence of Antiproton Production in Proton-Nucleus Collisions at 17.5 and 12.3 GeV/c

A Dissertation

Presented for the

Doctor of Philosophy Degree

The University of Tennessee, Knoxville

Saskia Mioduszewski

December, 1999

Acknowledgments

First and foremost, I would like to thank my family for their constant and patient support throughout my graduate career. From my good friends, I received great support as well.

The people who have been my "bosses" have also been mentors to me. My adviser, Ken Read, has always helped me to focus on the big picture. I am very grateful for his farsighted guidance. He also helped me choose antiprotons as a thesis topic. Soren Sorensen's ever-challenging nature has always helped improve my work over the years. I also have to thank Soren for first sparking my interest in this field of physics when I worked for him as an undergraduate during the summer of 1992. Brian Cole, the experiment spokesperson, is responsible for coming up with the idea for the experiment and, together with Ron Soltz, the deputy spokesperson, has managed the building, data-taking, and analysis of the experiment. Both Brian and Ron have been closely involved in the analyses presented in this thesis.

I would also like to thank committee members Yuri Kamyshkov and Larry Townsend for working with me to improve this thesis.

None of the work in this thesis would have been possible without the work done by the entire E910 collaboration. I want to recognize the help of my fellow E910 students: Xihong Yang, Hiroyoshi Hiejima, and David Winter of Columbia University and Yagmur Torun of SUNY, Stony Brook.

The High Energy Reactions Group (HERG) at ORNL, led by Glenn Young, includes Frank Plasil, Ken Read, Terry Awes, Yuri Kamyshkov, Yuri Efremenko, Paul Stankus, Vince Cianciolo, and Shirley Ball. They have provided me with a great number of resources as well as an endless source of information to address my questions. The presence of Vince Cianciolo, who is also a member of E910, in the HERG group has been especially valuable to me. Vince was very helpful through discussions concerning the slow proton analysis in this thesis and the TOF calibrations necessary for the antiproton analysis. Paul Stankus, an antiproton expert himself, has also provided insight through many interesting discussions. Yuri Efremenko, my office-mate at ORNL, was always nearby to talk about physics. Shirley Ball has helped me with countless administrative problems. The System Manager, Charles Thomas, has been an enormous help with providing system resources to the E910 data analysis.

The other members of the University of Tennessee heavy ion physics group, besides Soren and Ken, are post-doc Kyle Pope, and students Jason Newby, Andy Glenn, and Sam Held (who recently graduated). Former post-doc Dave Morrison was in the group when I first began working with them. He taught me some of the finer points of emacs and first introduced me to PERL.

Last, but certainly not least, I would like to acknowledge the support of my friend Steffen Bass. He has given me great insight into the phenomenology of relativistic heavy ion physics.

The research resulting in this thesis has been supported by both the United States Department of Energy under contract DE-FG02-96ER40982 with the University of Tennessee and the University of Tennessee Science Alliance Program.

Abstract

Experiment 910, performed at the Brookhaven National Laboratory Alternating Gradient Synchrotron (BNL-AGS), is a fixed target proton-nucleus experiment. We analyze data for nominal beam momenta 12 GeV/c and 18 GeV/c and targets Au, Cu, and Be. We characterize events with the number of projectile collisions. A new model is presented to relate the number of "grey tracks" to the number of projectile collisions and compared to a previously established model. The results of the models are similar, but the new model is shown to better describe the data. We investigate antiproton production. In an attempt to disentangle the production mechanisms and reabsorption of antiprotons within the nucleus, yields of antiproton production are compared for different targets and beam momenta. For the first time, antiproton multiplicities are investigated as a function of the number of projectile collisions. Results show that the mean antiproton multiplicities tend to decrease with increasing number of projectile collisions. We compare results with cascade model predictions.

Contents

List of Tables

List of Figures

Chapter 1

Introduction

1.1 Relativistic Heavy Ion Physics

A primary goal of relativistic heavy ion physics is to study the nuclear equation of state. To achieve this, nuclear matter is probed under extreme conditions. It has been predicted that at high temperature and high baryon density, nuclear matter will undergo a phase transition to a phase in which quarks will be deconfined, called the Quark Gluon Plasma (QGP) [1]. Even earlier, such phase transitions of nuclear matter had been predicted to occur at high densities [2, 3]. Lattice QCD calculations predict a temperature of 150-200 MeV for this phase transition to occur [4, 5]. At a similar temperature, lattice QCD calculation have also predicted chiral symmetry restoration resulting in very small light quark masses [6].

At the Relativistic Heavy Ion Collider (RHIC) at Brookhaven National Laboratory, beams of Au nuclei at 100 GeV/nucleon will soon be collided to find evidence for the existence of the QGP. There are many proposed signatures of the QGP, including enhanced antimatter production. In order to recognize a signature of the QGP, we must first gain understanding of the physics processes that occur in $A + A$ collisions in the absence of the QGP. With multiple processes occuring simultaneously, $A + A$ collisions are not the simplest testing ground. Many of the physics processes present in $A + A$ collisions are also present in $p + A$ collisions. This thesis explores the specific processes of antiproton production and reabsorption in $p + A$ collisions.

1.2 The Physics in $p + A$ Collisions

The physics processes themselves can be studied in great detail in the $p + A$ environment, which is much less complicated than the $A + A$ environment. When dealing with only one projectile nucleon, one can study what happens to the projectile and its energy as it traverses the nucleus. We are particulary interested in the number of collisions that the projectile undergoes within the nucleus. The mean number of projectile collisions, $\overline{\nu}$, for a given impact parameter b can be estimated with the Glauber geometry [7],

$$\overline{\nu} = \sigma_{NN} \int_{-\infty}^{\infty} \rho(z, b) dz, \tag{1.1}$$

where ρ is the nuclear density and σ_{NN} is the inelastic free nucleon-nucleon cross section. The number of projectile collisions, ν, in a $p + A$ collision is the best characterization of the "centrality" of the event. Since this quantity cannot be directly measured, we relate the number of grey particles, N_g, in an event to ν. "Grey tracks" is a term that stems from emulsion experiments and, for E910, includes slow protons and slow deuterons. The definition of a grey track is more specifically stated in Section 3.2. Grey tracks are emitted as a result of projectile collisions, and therefore the number of grey tracks is correlated to the number of projectile collisions. In an analysis presented in Chapter 4, we attempt to extract ν on an event by event basis. We can then use ν to characterize events and present other observables as a function of event "centrality." This definition of centrality, as well as the relation between N_g and ν, is further discussed in Chapter 4.

1.3 Antiprotons in Heavy Ion Physics

Antiproton production is currently a topic of great interest in relativistic heavy ion physics. Enhanced antimatter production has been proposed as a signature of the Quark Gluon Plasma [8]. When chiral symmetry is restored, the light quark masses are expected to approach zero. The part of the quark mass present due to QCD interactions is expected to vanish, leaving only the mass of the "free"-quark (which is present due only to non-QCD interactions). This "free"-quark mass is small for u, d, and s quarks and their antiquarks ($\sim$5, 10, 150 MeV respectively) making it energetically more favorable for quark-antiquark creation. Thus, the restoration of chiral symmetry would result in an abundance of antiquarks. Three antiquarks can coalesce to form an antibaryon. In such a scenario, antiproton production would be enhanced.

1.3.1 Antiproton Production

The production of antiprotons has been of interest for over 40 years. Antiproton production was observed in proton-nucleus collisions at bombarding energies below the production threshold of antiprotons [9, 10, 11]. Assuming the antiproton is created in the first nucleon-nucleon collision (as in a "first collision model"), the simplest reaction is

$$p + N \longrightarrow p + N + p + \overline{p}. \tag{1.2}$$

To produce an antiproton in a collision between nucleons, the energy necessary in the center of mass frame is $4m_N$, or 3.75 GeV. This corresponds to a beam momentum of approximately 6.5 GeV/c in the lab frame. One explanation for production below the energy threshold given by Dorfan et. al. was that the Fermi motion of the nucleons contributed to the energy necessary for production [11]. This mechanism could not, however, account for the increased production rates observed in nucleus-nucleus collisions [12]. Subthreshold antiproton production in

$A + A$ collisions was first measured at the Bevelac by Carroll *et al* [13] in 1989. Shor, Perez-Mendez, and Ganezer [12] were able to fit subthreshold $\overline{p}$ production in $p+A$ collisions using a first collisions model which included the internal momentum of nucleons. However, when extending this model to $A + A$ collisions, they were not able to fit experimental data. This suggests that there are collective effects contributing to antiproton production in heavy ion collisions.

In the nuclear medium, the equation of motion for a particle is altered due to the interaction with surrounding matter. This interaction is taken into account by the particle self-energy [14]. The self-energy of a nucleon or an antinucleon causes its mass to be reduced, thus lowering the production threshold. This effect has been studied as a possible mechanism for subthreshold kaon production [15], as well as subthreshold antiproton production [16, 17]. The nucleon self-energy has a scalar part and a vector part. The vector part of the self-energy for the antiproton changes its sign relative to the proton self-energy under G-parity transformation [18, 16, 17, 19]. This leads to an attractive potential for the antiproton, thus lowering the energy of the proton-antiproton pair. This has also been studied as a mechanism for subthreshold $\overline{p}$ production in the references noted above.

Another possible mechanism for antiproton production in heavy ion collisions is a multi-step process. Since $p + A$ and, especially, $A + A$ collisions have multiple individual hadron-hadron collisions, they provide more opportunity for antiproton creation. This idea challenges the so-called "first collision models" which assume that only first collisions (between projectile nucleons and target nucleons) can provide enough energy for antiproton production near threshold. The validity of this assumption can be disputed if one considers a mechanism for storing the energy from a first collision to be used in a subsequent collision for creating an antiproton. Transport models have proposed that at energies near the production threshold, the dominant mechanism is an intermediate nucleon resonance state. This large, heavy resonance serves as an energy reservoir making it kinematically more favorable to produce a $p-\overline{p}$ pair in a subsequent collision [20]. In a similar argument, Koch and Dover study the importance of Δ resonances in $\overline{p}$ production using a hadrochemical model [21] which contains mostly nucleons, Δ (1232) resonances, and pions.

1.3.2 Antiproton Reabsorption

Opposing antiproton production is the process of reabsorption. The overall yield depends not only on the production mechanism but on the reabsorption as well. The antiproton has a large annihilation cross section, making it difficult for an antiproton to escape the baryon rich nucleus [22, 20]. Figure 1.1 shows the parametrization of the $p\overline{p}$ cross section suggested by Koch and Dover [21]. The parametrization is given by,

$$\sigma_{ann}^{p\overline{p}} = \sigma_0^N \frac{s_0}{s} \left[\frac{A^2 s_0}{(s-s_0)^2 + A^2 s_0} + B \right], \tag{1.3}$$

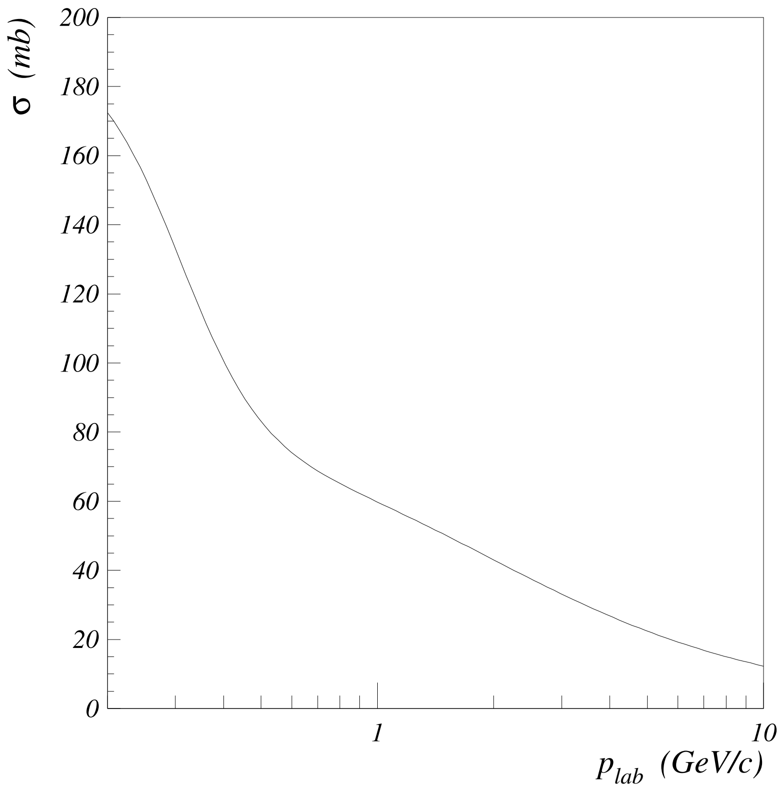

Figure 1.1: Parametrization of $p\overline{p}$ annihilation cross section by Koch and Dover.

where $\sigma_0^N = 120$ mb, $s_0 = 4m_N^2$, $A = 50$ MeV, and $B = 0.6$. These large annihilation cross sections could lead one to believe that the survival rate for antiprotons in the nuclear medium is close to zero. Transport models, which contain these cross sections, have also included a formation time for all particles coming out of a string fragmentation. String fragmentation, which is a high mass flux tube (or high mass baryon resonance state) that decays, is the dominant mechanism for particle production at AGS energies in RQMD [23] and UrQMD [24]. These models are described in detail in Chapter 6. Included in that chapter is a discussion of the formation time which reduces the rate of reabsorption, as well as an additional time delay for annihilation that is implemented in only RQMD.

1.3.3 Antiproton Studies in Thesis

Neither production nor reabsorption occuring in the nuclear medium are fully understood. Proton-nucleus collisions are, again, a clean environment for studying and attempting to untangle these opposing processes. It is particularly interesting to investigate antiproton yields as a function of the number of projectile collisions. The goal of this thesis and a major goal for E910 is to study the production and reabsorption of antiprotons by examining yields as a function of target size, beam momentum, and centrality.

Chapter 2 describes the experimental apparatus. Data reduction is described in detail in Chapter 3. Chapter 4 introduces our measure of centrality and outlines our method of extracting this quantity. Chapter 5 presents antiproton results, including yields as a function of target size, beam momentum, and centrality (as defined in Chapter 4). A brief discussion of recent results from other experiments is also included in Chapter 5. Chapter 6 describes the models which are used to compare to the data. Chapter 7 make comparisons to these models. Finally, Chapter 8 presents conclusions.

Chapter 2

The Experiment 910

2.1 General Experimental Apparatus

A schematic illustration of the experiment is shown in Fig. 2.1. The individual detectors are described in the sections that follow.

2.2 Beamline

Experiment 910 was performed in the A1 beam line at the AGS during the spring and summer of 1996. There were six proportional wire chambers along the beam line. These are discussed in greater detail in the next section. The beamline also included three Čerenkov counters for rejecting pions in the beam. In addition, there were two scintillating beam counters, S_1 and ST, used to define beam triggers and two veto counters used to tune the beam and reject upstream interac-

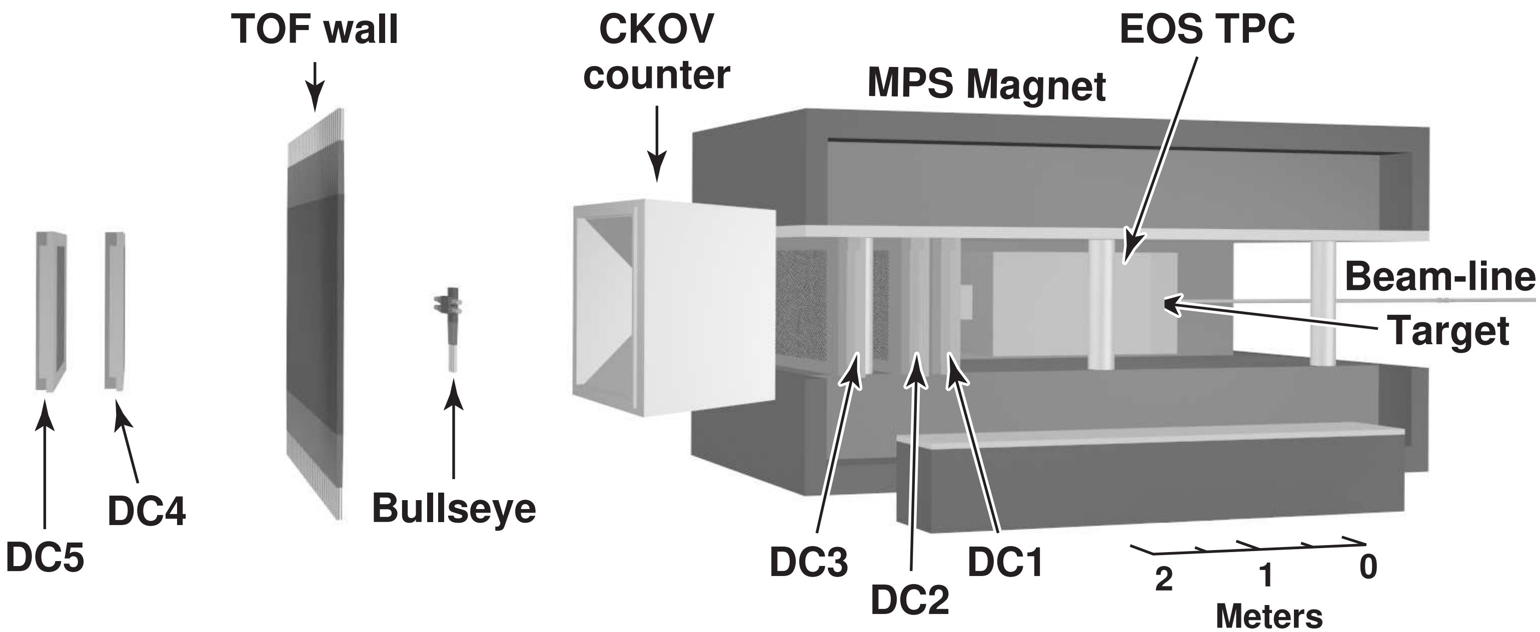

Figure 2.1: E910 spectrometer.

tions. There were two different interaction triggers used. For some of the data, an interaction was determined by the number of hits in the scintillating fiber detector placed directly downstream of the target. An event with 4 or more hits in the fibers satisfied the minimum bias trigger, and an event with 20 or more hits in the fibers satisfied the central interaction trigger. For other data, we used a bulls-eye scintillator, placed downstream of the Čerenkov detector with an aperture of 11×12 mrad, for a minimum bias interaction trigger only. For these data, the interaction trigger was defined as

$$S_1 \wedge ST \wedge \overline{V_1} \wedge \overline{V_2} \wedge \overline{C_1} \wedge \overline{C_2} \wedge \overline{C_3} \wedge \overline{PRE} \wedge \overline{BE}. \tag{2.1}$$

2.3 Beam Chambers

There are six beamline chambers, A1 to A6. The four most upstream chambers, A1 to A4, are used to determine the momentum of the beam. They consist of two half-cell staggered wire planes, with a pitch of 1/16 in, that give information about the horizontal position of the beam. A1 and A2 are located upstream of a series of six dipole magnets and a bend in the beamline. The bend is 7.02428°, and the integrated $\int Bdl$ is approximately 7.3 T·m for our nominal beam momentum of 18 GeV/c. A3 and A4 are located downstream of the six dipole magnets. Together, A1 through A4, give a bend-plane measurement necessary for the momentum reconstruction. The reconstructed momentum is used for diagnostic comparisons to the beam momentum measured in the TPC.

The other two chambers, A5 and A6, which are located just upstream of the target, are used to project the beam to the target plane. A5 and A6 have four planes each. Two planes measure the horizontal position of the beam and two measure the vertical position. The projected beam position at the target plane is used as an initial value in the algorithm for finding the primary vertex.

Table 2.1 lists the characteristics of the beamline chambers. The efficiency for A1 to A4 is defined as the percentage of events for which there was a hit in at least one of the two planes. For A5 and A6, the efficiency is the percentage of events for which there was a hit in at least one of the two planes in a pair (horizontal or vertical).

2.3.1 Calculating Beam Momentum Using A1-A4

The beam momentum is reconstructed using the measured beam deflection and the integrated effective dipole field strength. Since all four positions are required for the calculation, the momentum reconstruction efficiency is typically only 10%. The momentum resolution is approximately 2%. Figure 2.2 shows the distribution of the reconstructed momentum compared to the beam momentum recontructed in the time projection chamber (TPC). The reconstructed beam momentum is used as an initial seed for tracking beam tracks in the TPC. Since the momentum

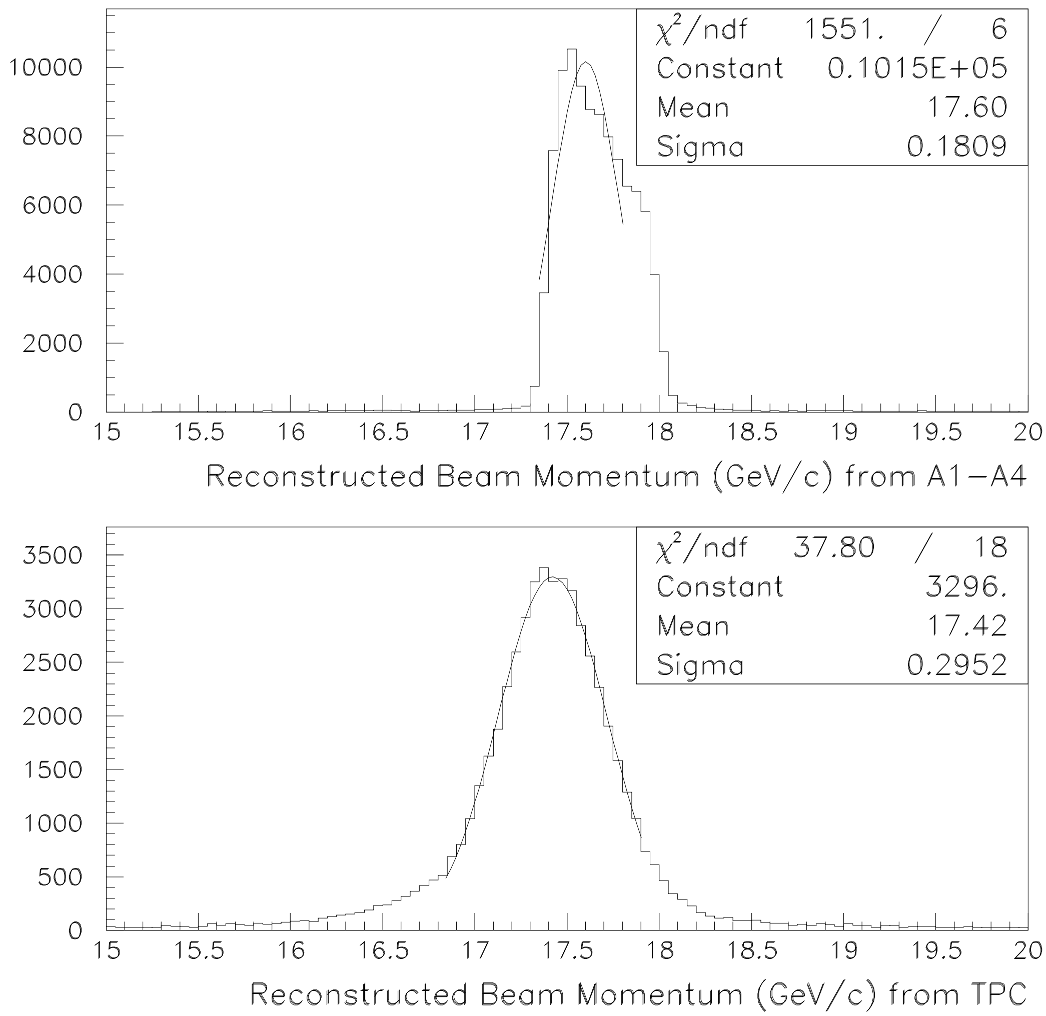

Figure 2.2: Reconstructed momentum using beamline chambers vs. TPC.

Table 2.1: Characteristics of the chambers along the beamline.

Chamber	No. of wires per plane	Position along beamline [m]	Typical efficiency [%]
A1	128	7.13 a	50
A2	128	1.25 a	85
A3	96	1.19 b	55
A4	96	24.35 b	45
A5 (horizontal)	64	10.36 c	90
A5 (vertical)	128	10.36 c	93
A6 (horizontal)	64	4.34 c	93
A6 (vertical)	96	4.34 c	96

a) position is relative to and upstream of the middle of first of the six dipole magnets.
b) position is relative to and downstream of the middle of the last the six dipole magnets.
c) position is relative to and upstream of the target plane.

reconstruction in the chambers is only 10% efficient, the reconstructed beam momentum is averaged over each run and stored. If the momentum is not available for a particular event, the run-averaged momentum is used.

2.3.2 Projecting Beam to Target Plane

The horizontal and vertical positions of the beam at A5 and A6 are used to project the beam to the target. Both vertical and horizontal positions at both chambers are required for vertex pointing, leading to an efficiency of 90% for this calculation. The horizontal width of the beamspot is approximately 2 cm, and the vertical width is 1.5 cm. Figure 2.3 shows a distribution of the projected vertex position at the target vs. the position reconstructed in the TPC. Similar to the

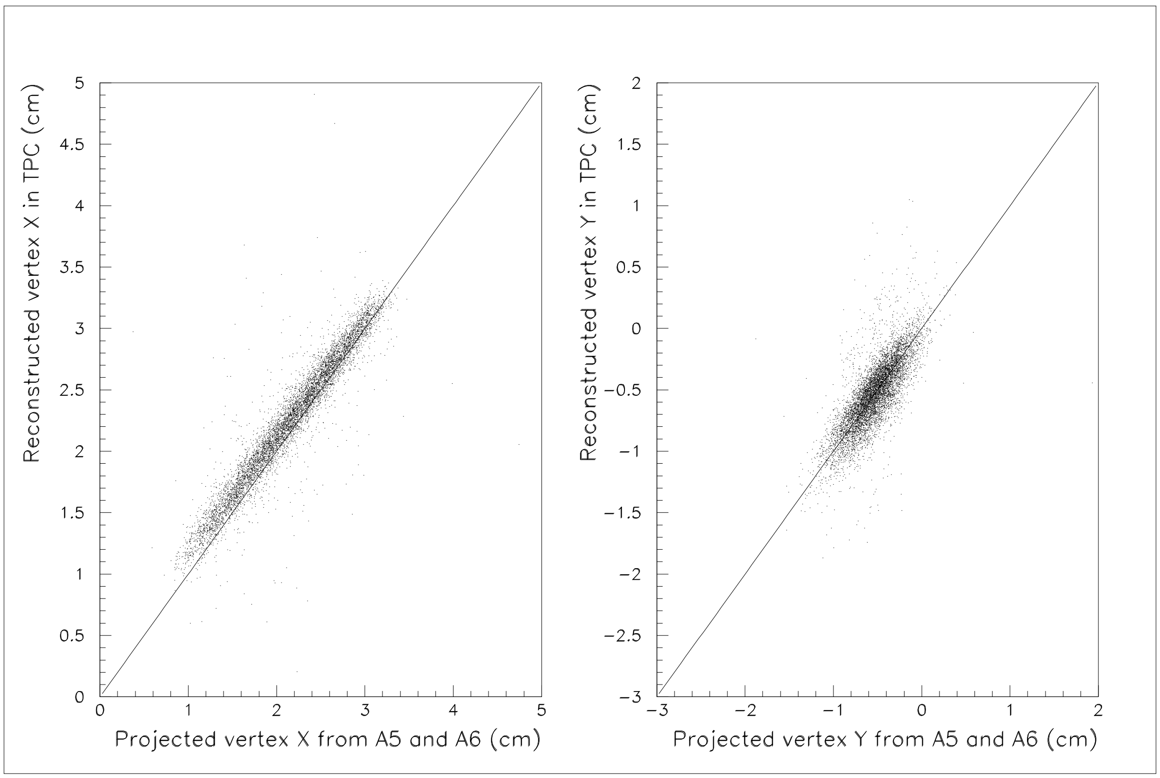

Figure 2.3: Reconstructed position using beamline chambers vs. TPC.

reconstructed beam momentum, the projected vertex position is used as an initial seed for tracking beam tracks in the TPC. Again, if the projected vertex position is not available for a particular event, the run-averaged position is used.

2.4 TPC

The time projection chamber (EOS TPC [25]) has an active drift volume of 96 x 75 x 154 cm^3 with a total of 15360 cathode pads (120 x 128). The TPC is situated in the center of the MPS magnet allowing for 3-dimensional tracking. The MPS magnet is a large C-shaped dipole magnet with a nominal central field of 0.5 T. The momentum resolution in the TPC for the "Minipass" (see Section 3.1) analysis was calculated to be $\delta p/p = 0.002 + 0.005p$ (GeV/c). The TPC operated at atmospheric pressure with P10 gas (90% Ar and 10% CH_4). The vertical electric field was 120 V/cm resulting in a drift velocity of approximately 5 cm/μs. A typical event in the TPC is shown in Fig. 2.4.

2.5 TOF

The Time-of-Flight wall is located approximately 8 m downstream of the target. It has 32 slats with photomultiplier readout at the top and bottom of the slats, for a total of 64 channels. Each slat has a scintillator that is 70 1/8" long, 6" wide, and 1 7/8" thick and two light guides (one on each end). There is photomultiplier

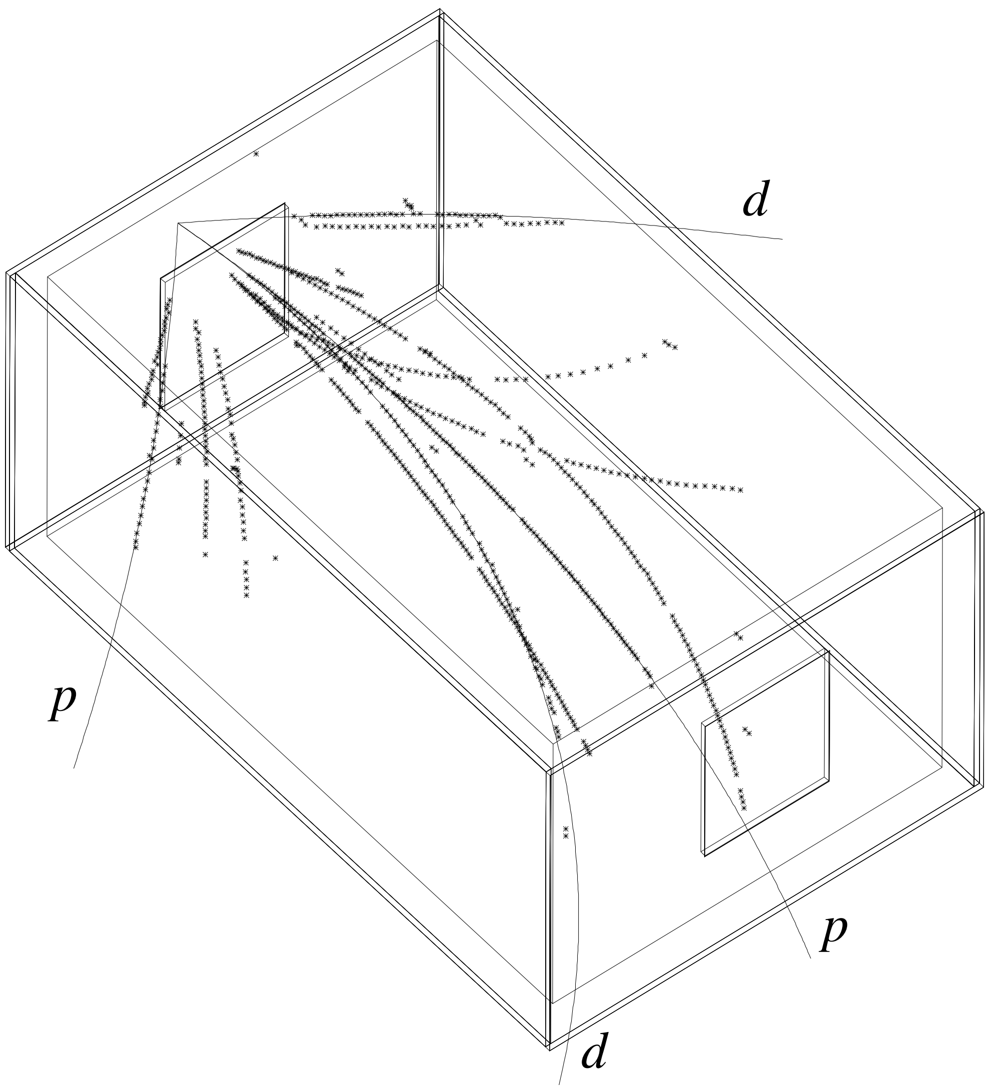

Figure 2.4: Event showing hits and fitted trajectories in the TPC. Indicated particle identities are based on measured ionization energy loss in the TPC.

readout at the top and bottom of each slat. The active area of the TOF wall is approximately 5×2 m^2.

2.5.1 TOF calibration

The TOF wall is the primary detector used for antiproton identification. Thus, the calibration of this detector has particular relevance to this analysis. There are five calibration constants to be determined for each slat: three gain factors, a time offset, and a slew constant. The gain factor for S1, the scintillator immediately upstream of the target, is assumed to be constant throughout the E910 run and has a value of 25 ps/ch. The remaining four constants are fit simultaneously for protons and pions using a least-square minimization. This method is employed on approximately five full-sized runs at a time (which is approximately equivalent to 50-100K events). This much data is necessary to have enough hits on each slat in order to obtain a reliable fit. After one pass through the data using this method, the total E910 data set is divided into three run periods. The end of a run period reflects a point in the E910 run where conditions affecting TOF calibrations changed significantly. Each of the two gain factors (top and bottom readout) for each TOF slat is averaged over a run period. These gain factors are then fixed for a second pass on the data using the least-squared minimization, this time fitting only the time offset and slew constant. These two remaining calibration constants are allowed to vary simultaneously in the fit and determined for each pair of 8 mm data tapes (approximately 5 full-sized runs).

2.5.2 TOF resolution

The resulting TOF resolution varies with momentum. Since the resolution is most critical in a region of momentum where the flight times of different particle species start to overlap, Fig. 2.5 shows the resolution for pions with $1.5 < p < 2.0$ GeV/c. The x-axis is the measured time-of-flight minus the expected time-of-flight assuming a pion mass. The small bump on the positive side of the peak represents the kaons and the large bump farther on the positive side represents the protons. The TOF resolution for pions in this momentum region is 160 ps. Figure 2.6 demonstrates the proton time-of-flight resolution for $3.0 < p < 3.5$ GeV/c is 164 ps. The peak on the negative side of the proton peak represents both pions and kaons.

2.6 CKOV

The E910 CKOV is a highly segmented gas threshold Čerenkov counter. It is located 4.8 m downstream of the target. It has 96 primary mirrors, half of which are in the upper panel and half in the lower panel. The 2 panels are $\pm 60°$ from the x-z plane. Each primary mirror focuses light on a phototube in the opposite panel. The CKOV ran with Freon-114 gas. The approximate threshold momenta for different particle species is shown in Table 2.2.

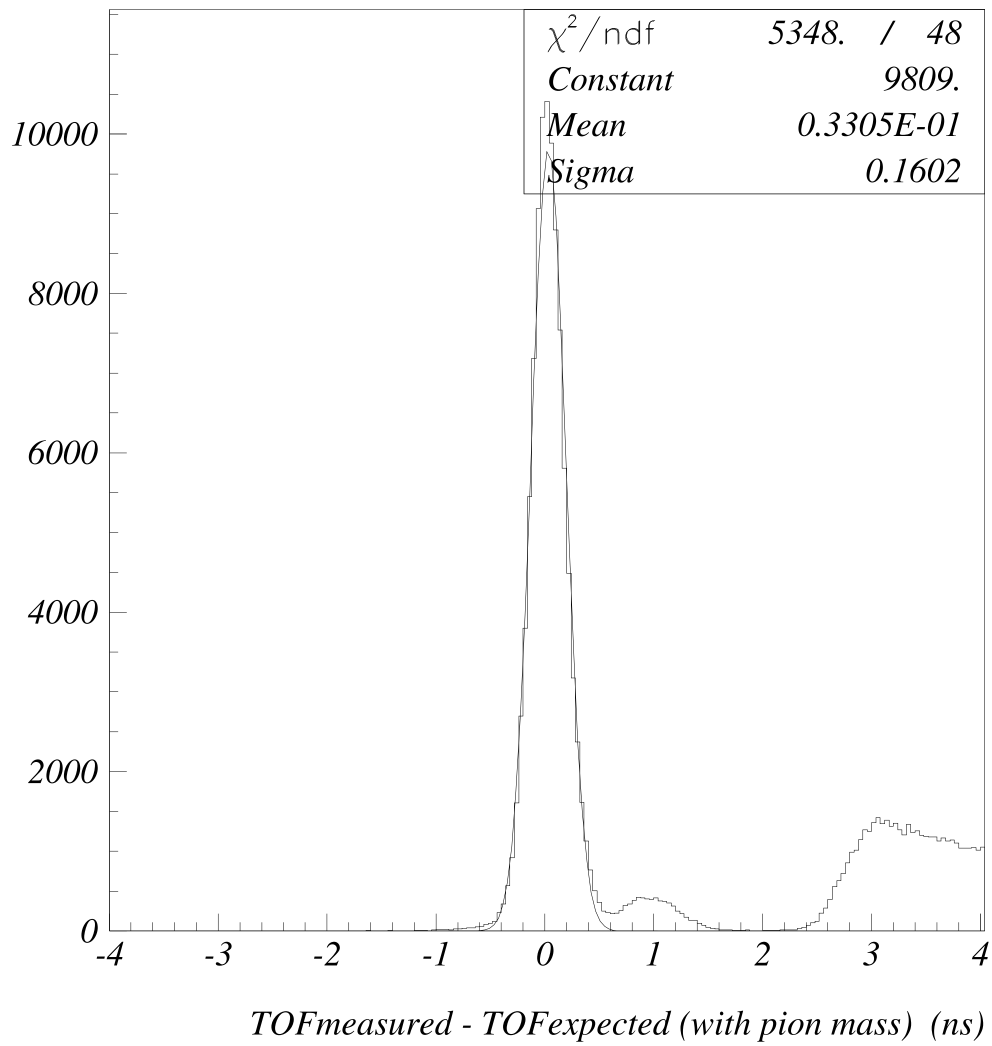

Figure 2.5: $\mathrm{TOF}_{measured}$ - $\mathrm{TOF}_{expected}$ assuming the mass of a pion for $1.5 < p < 2.0$ GeV/c.

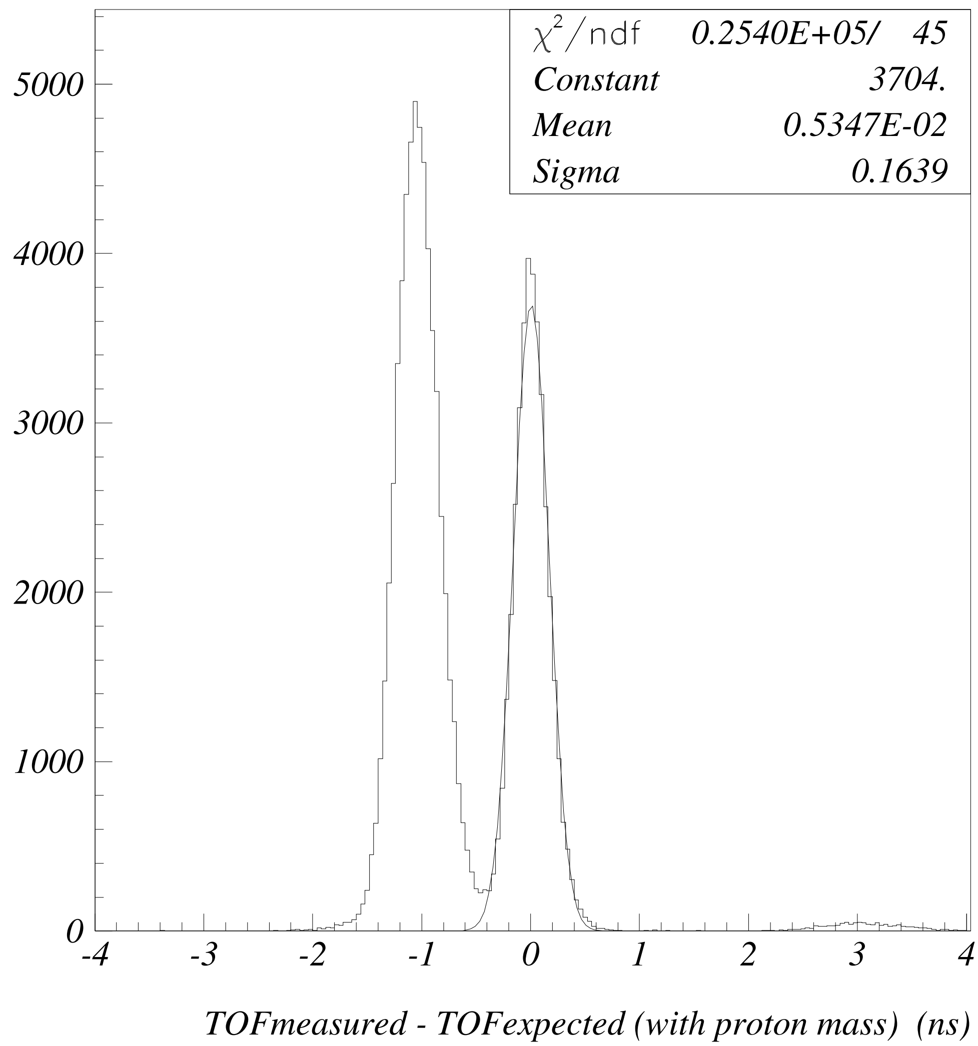

Figure 2.6: TOFmeasured - TOFexpected assuming the mass of a proton for $3.0 < p < 3.5$ GeV/c.

Table 2.2: Momentum thresholds for CKOV.

Particle	e	μ	π	K	p
Threshold (GeV/c)	0.009	1.9	2.5	9.0	17.1

2.7 Drift Chambers

There are five drift chambers, DC01 to DC05. DC01, DC02, and DC03 are within the MPS magnet directly downstream of the TPC. The remaining two chambers, DC04 and DC05 are on a stand located downstream of the TOF wall.

Each chamber contains 7 anode planes and 8 cathode planes (alternating). There are two X planes and one X' plane for measuring the horizontal coordinate of a track and one Y and one Y' plane for measuring the vertical coordinate. The X' and Y' planes are staggered with respect to X and Y by half of a cell. The cell width, the distance between anode wires, is 6.35 mm or 1/4 in. There is a field wire between each pair of anode wires operating at about 1.8 kV. There is a U plane, oriented at 30° to Y, and a V plane, oriented at $-30°$ to Y. The active area is 173×100 cm^2. Each chamber has a total of 1677 anode wires. The anode wires are 25 μm diameter Au-plated W. The cathode wires and field wires are 75 μm stainless steel. The cathode planes are operated at about 2.3 kV. The gas in the chambers is a mixture of 75% Ar, 12% Isobutane, and 13% Methylal.

Chapter 3

Data Reduction

3.1 Analysis Passes

An initial pass, the "Minipass," was performed on a fraction of the data. This pass included full tracking and particle identification in the TPC, as well as some preliminary (uncalibrated) particle identification information from the TOF and CKOV. Since slow protons and deuterons can be identified solely by their ionization energy loss in the TPC, the grey particle analysis was done entirely on the output of the Minipass. The next pass on the entire data set was the calibration pass, "Pass0." To minimize CPU time spent on this pass, only beam particles were tracked. Calibration constants for most detectors were obtained from Pass0. The TOF and CKOV detectors required tracking of all particles for full calibration. "Pass1" is an analysis pass in which full tracking and particle identification was performed on all of the data. Calibration constants for CKOV and TOF were obtained from the output of Pass1. The modules producing TOF and CKOV information were then run on the data again with all of the calibration constants. The antiproton analysis was done using Pass1 output. One last analysis pass, "Pass2," will be performed on the data. The primary goals of this pass are to compile all of the particle identification information to obtain a global particle identification and to produce data summary tables of the data for future analyses.

The two beam momenta used for this thesis analysis are nominally 18 GeV/c and 12 GeV/c. The actual average reconstructed beam momenta are 17.5 GeV/c and 12.3 GeV/c respectively. Although the data in this thesis will be presented referring to the nominal beam momenta, 18 and 12, for simplicity, the reader should be aware that the actual beam momenta are 17.5 and 12.3 GeV/c.

The remainder of the data reduction chapter is divided into two sections. The first describes the data reduction resulting in the final N_g multiplicity distributions. These distributions are used in Chapter 4 in an analysis to determine a relationship between the number of grey particles in an event and the mean number of projectile collisions for such an event. The second section describes the data reduction resulting in the final antiproton yields.

3.2 Grey Particle Distributions

The grey particle analysis was performed on the 18 GeV/c data taken with our most minimum bias trigger, the bullseye trigger. Since the scintillating fiber had to be placed between the target and the front of the TPC, the scintillating fiber trigger data has a slightly smaller geometric acceptance than the data taken with the bullseye trigger. The minimum bias, especially on the $N_g = 0$ events, from the bullseye trigger combined with the larger acceptance was the reason for using this data set to do the grey particle analysis. This is a small fraction of our total data set, but sufficient for this analysis due to the large number of grey particles.

To remove elastic events and events with only a beam particle from our data sample, we accept only events which contain two or more charged particles originating from the event vertex or a single charged particle with transverse momentum greater than 0.06 GeV/c and longitudinal momentum less than 12 GeV/c. We further require that the reconstructed vertex be within the target's x-y boundary, and have a z-position within 2.6 cm of the centroid for the Au and Cu targets, and 1.75 cm for the Be target. The number of events that remain after applying these cuts are given in Table 3.1.

Protons and deuterons are identified by their measured ionization energy loss in the TPC. Protons are required to be within 2.25 standard deviations of the mean proton dE/dx and farther than 1.5 σ from the mean pion dE/dx. The proton band

Table 3.1: Event statistics and forward angle cuts for all targets. Cuts for deuterons are in parentheses.

Target	*Events*	Forward cuts	protons	deuterons
Au	35520	0.98 (0.97)	56881	10622
Cu	49331	0.98 (0.96)	45784	6224
Be	100609	0.94 (0.94)	30622	3366

is separated from the pion band up to a momentum of 1.2 GeV/c. Deuterons are required to be within 2.25 σ of the deuteron dE/dx band and farther than 2.25 σ from the proton and pion bands. The electron/positron band intersects both the proton band and the deuteron band. Figure 3.1 shows the dE/dx distribution as a function of momentum with the lines showing the particle identification cuts for protons and deuterons.

To reject positrons which come from photon conversions in the target, we form a pair for each positive track that is within the positron dE/dx band using the negative track in the electron band which makes the smallest relative transverse momentum. If the relative transverse momentum, $q_T = \sqrt{(\mid 2.0(\vec{p_1} \times \vec{p_2}) / \mid \vec{p_1} + \vec{p_2} \mid \mid^2)}$, is less than 0.037 GeV/c, the positive track is removed from the analysis. Applying this pairing algorithm to tracks within a momentum region where the electron/positron band does not intersect with any band of another particle species gave an efficiency of identifying positrons of 30% for Cu and Au and 10% for Be. The contamination can be clearly seen in the $p - \cos\theta$ distribution in the

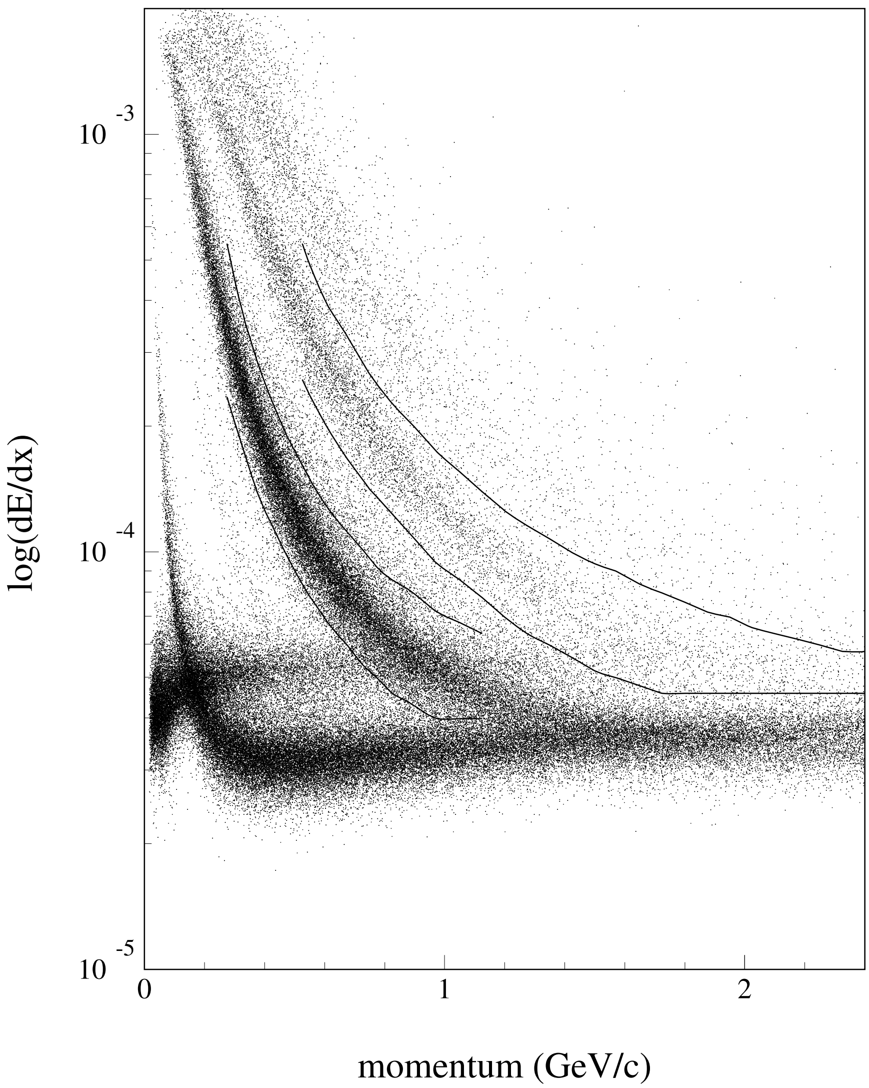

Figure 3.1: Distribution of dE/dx as a function of momentum. Lines indicate cuts described in text to identify protons and deuterons.

momentum region where the bands cross. For protons, the bands start to cross at approximately 0.7 GeV/c, and for deuterons, 1.3 GeV/c. In $\cos\theta$, the contamination is predominantly confined to the most forward angles. The majority of positrons are from π^0 decays. These are more forward peaked than the grey particle distribution. Therefore, we further apply cuts in the most forward region to reject positrons. The maximum allowed values of $\cos(\theta)$ are shown in Table 3.1. After these cuts, the remaining positron contamination was estimated to be approximately 5% in the N_g sample for Au and Cu and 12% for Be.

The acceptance is calculated for both protons and deuterons by analyzing simulated single tracks using the E910 analysis program. The momentum and angle are generated according to a sampling from raw data distributions. In the E910 analysis program, tracks and momenta are reconstructed. With the calculated acceptance (and tracking efficiency), the $p - \cos\theta$ distributions for both protons and deuterons are corrected. With the corrected distributions as input to the E910 analysis program, a second iteration of the acceptance calculation is performed. Acceptance corrected distributions for protons in momentum and angle are given in Fig. 3.2, shown only where the acceptance is greater than 10%. The angular distributions for all targets are nearly isotropic in the lowest bin, becoming progressively more forward peaked at higher momenta. The momentum distributions peak near 0.4 GeV/c for Au, and higher for the lighter targets. The projections in momentum for protons are shown in Fig. 3.3, and the projections in angle are

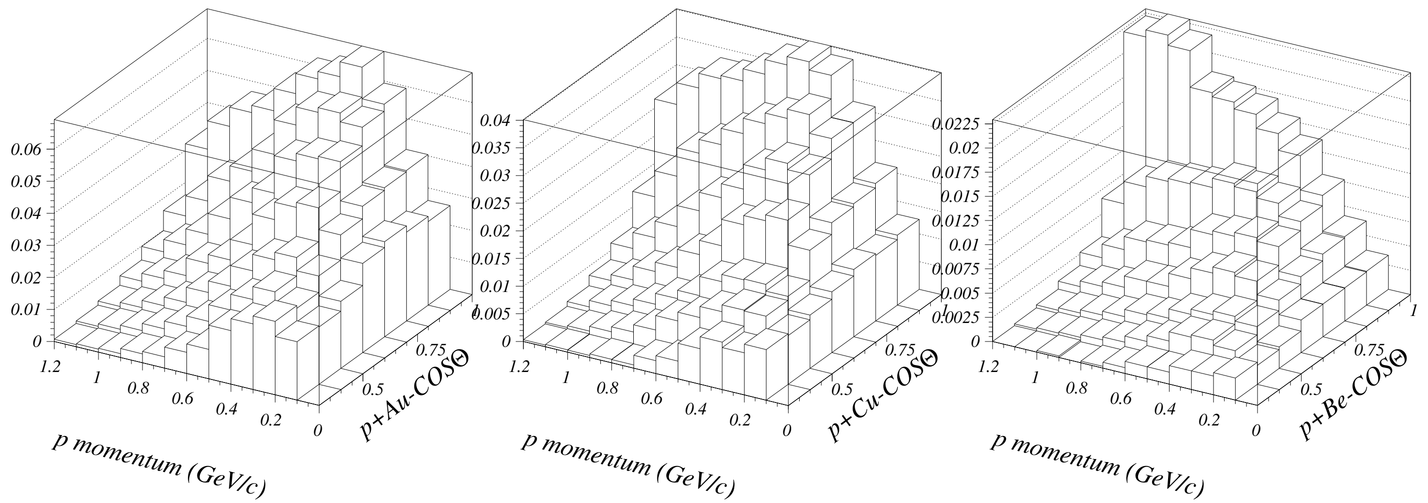

Figure 3.2: Acceptance corrected, event-normalized *momentum vs.* $\cos\theta$ distributions for protons for Au, Cu, and Be targets.

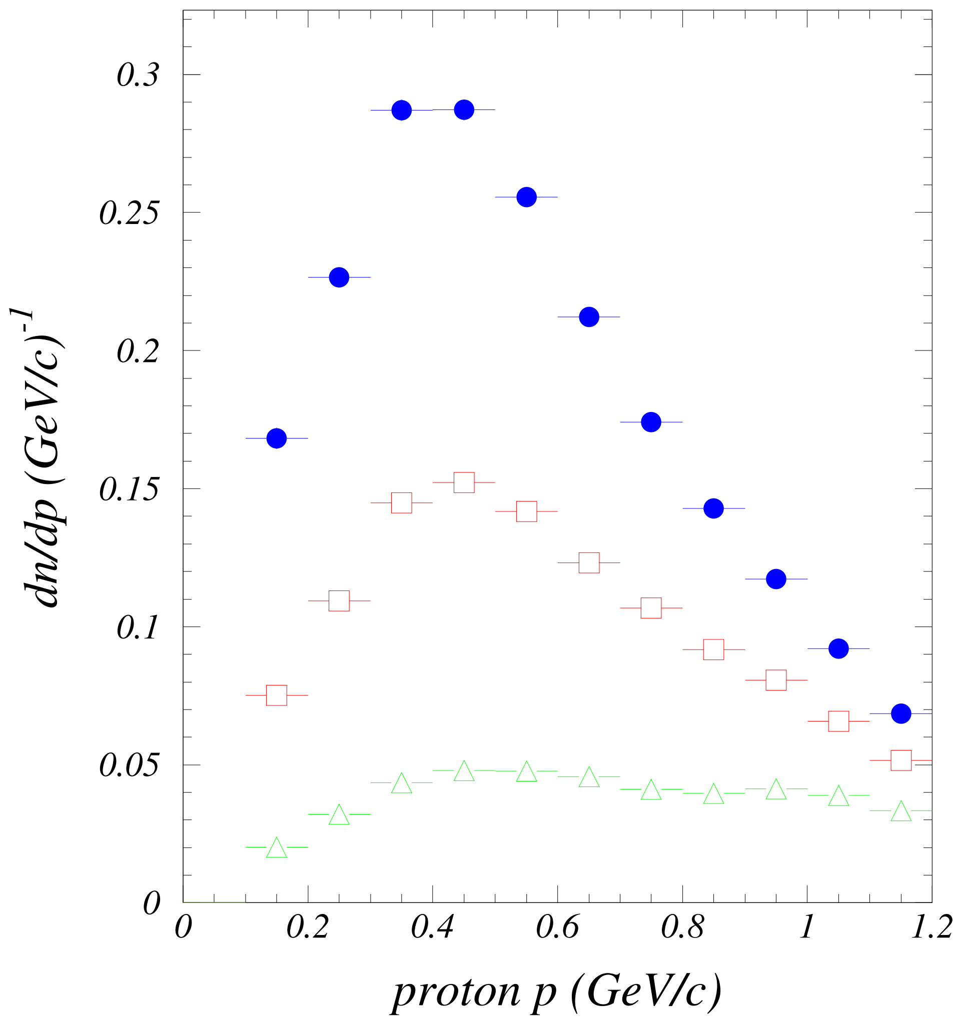

Figure 3.3: Acceptance corrected, event-normalized momentum distributions for protons. Solid circles for Au, open squares for Cu, and open triangles for Be target.

shown in Fig. 3.4. The momentum distributions for protons peak between 400 and 500 MeV/c. The peak is more pronounced for larger target size. The peak naturally falls at the limit of our particle identification capability. The angular distributions show the natural forward peaking of slow protons. For deuterons, the projections in momentum and angle are shown in Fig. 3.5 and 3.6. The momentum distributions for deuterons are peaked at a slightly lower momentum (between 300 and 400 MeV/c) than the proton momentum distributions. The deuteron momentum corresponds to an even lower proton momentum because a deuteron is formed by the coalescence of a proton and a neutron, each contributing to the deuteron momentum. The fraction of deuterons that are from the evaporation of the nucleus is larger than the fraction of protons that are evaporative protons. This can also be seen in the angular distributions. The deuterons are less forward peaked than the proton angular distributions.

Based on these distributions, we use a range of $0.25 < p < 1.2$ GeV/c for protons, and $0.5 < p < 2.4$ GeV/c for deuterons to define grey particles. The upper cuts are the limits of particle identification, 1.2 Gev/c for protons and 2.4 GeV/c for deuterons (see Fig. 3.1). The purpose of the lower momentum cut is to reject the evaporative protons/fragments. The value of the cut is consistent with the lower momentum cut for grey particles in the literature. It was chosen based on previous measurements of proton fragmentation spectra by the EOS collaboration for 1.2 GeV$\cdot A$ $Au + C$ collisions [26] and by a KEK group for 4 GeV/c $p + Pb$

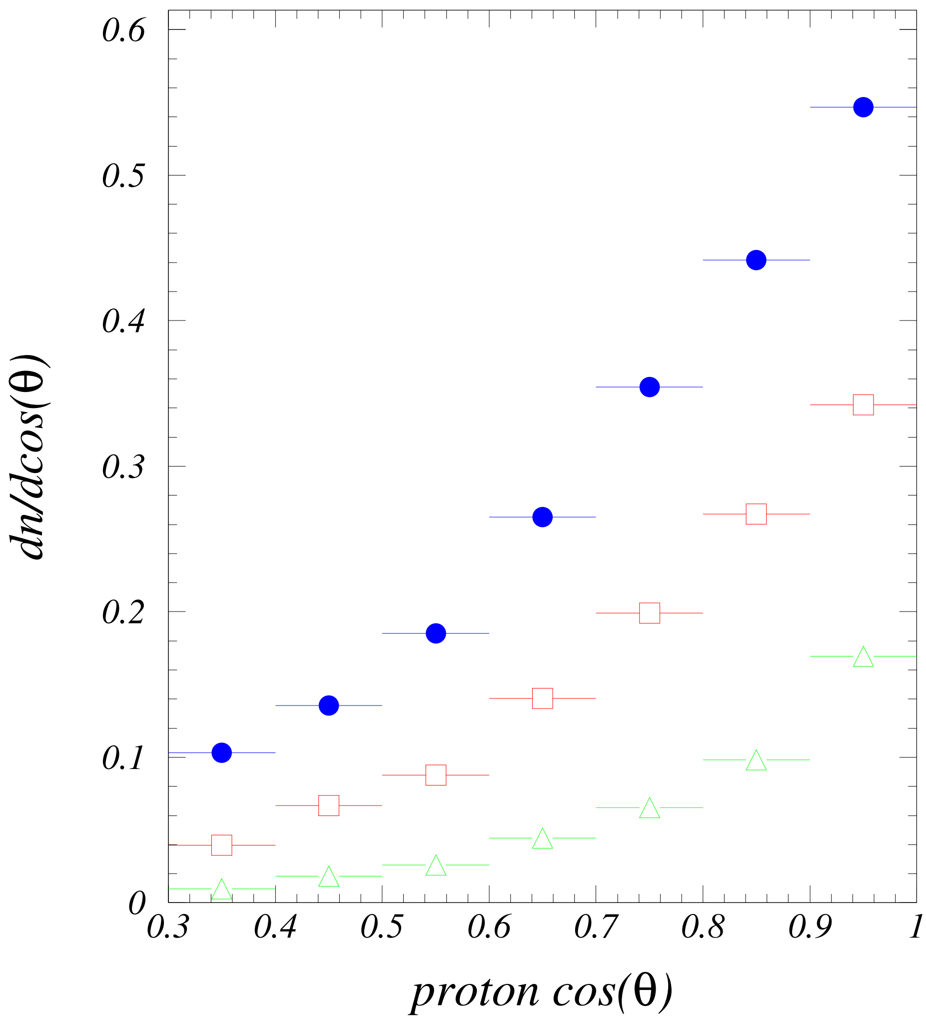

Figure 3.4: Acceptance corrected, event-normalized angular distributions for protons. Solid circles for Au, open squares for Cu, and open triangles for Be target.

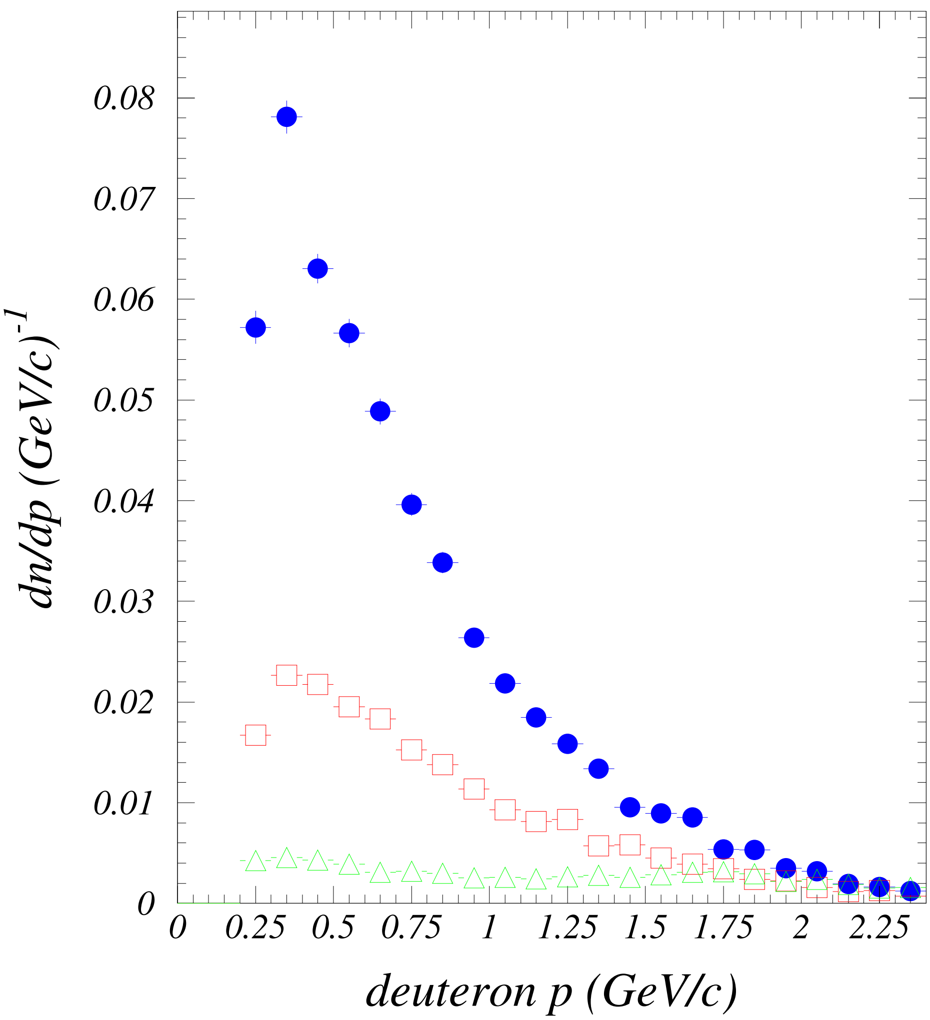

Figure 3.5: Acceptance corrected, event-normalized momentum distributions for deuterons. Solid circles for Au, open squares for Cu, and open triangles for Be target.

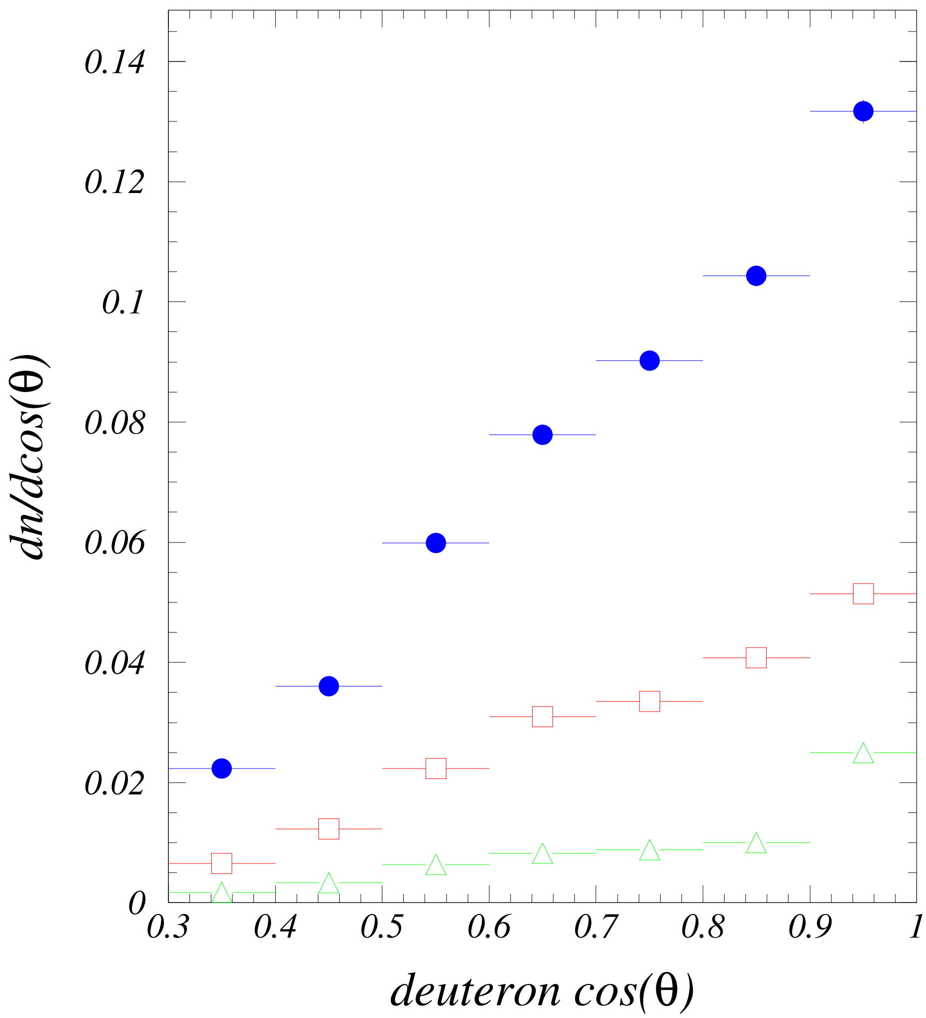

Figure 3.6: Acceptance corrected, event-normalized angular distributions for deuterons. Solid circles for Au, open squares for Cu, and open triangles for Be target.

collisions [27], and of spectra of fragments with Z $\geq$ 3 for 1-19 GeV/c $p + Xe$ collisions [28].

With this definition of a grey particle, Figs. 3.7 and 3.8 show the corrected momentum and angular distributions for different values of N_g for the Au target. The distributions do not shift toward larger angles and thus out of the TPC acceptance for large N_g. Such an effect would bias our determination of ν.

The distributions are corrected for target out contribution by subtracting the beam-normalized N_g distributions obtained from runs with an empty target holder. The normalization is done with the ratio of number of livebeam events with target in to the number of livebeam events with target out. The corrected distribution, dn/dN_g, is calculated with

$$\begin{aligned} \left(\frac{dn}{dN_g}\right)_{corrected} &= \frac{1}{N_{target\,IN}}\left(\frac{dN}{dN_g}\right)_{target\,IN} \\ &- \frac{(N_{livebeam})_{target\,IN}}{(N_{livebeam})_{target\,OUT}}\frac{1}{N_{target\,IN}}\left(\frac{dN}{dN_g}\right)_{target\,OUT}, \end{aligned} \tag{3.1}$$

where $N_{target\,IN}$ is the number of events passing the event cuts with the target in place.

Finally, we correct for the contribution from secondary interactions in the target (interactions of the projectile with a second nucleus). The correction is

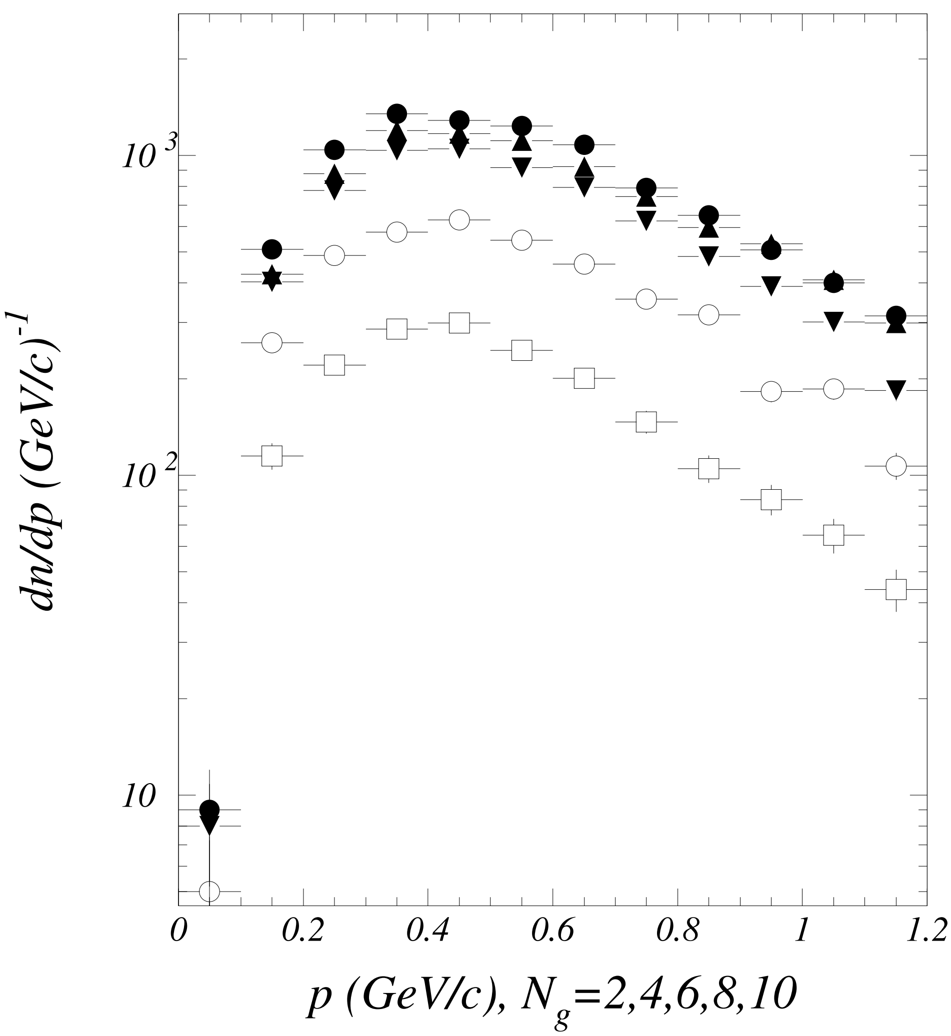

Figure 3.7: Momentum spectra of grey particles for events with $N_g = 2$ (closed circles), 4 (closed triangles), 6 (closed upside-down triangles), 8 (open circles), 10 (open squares).

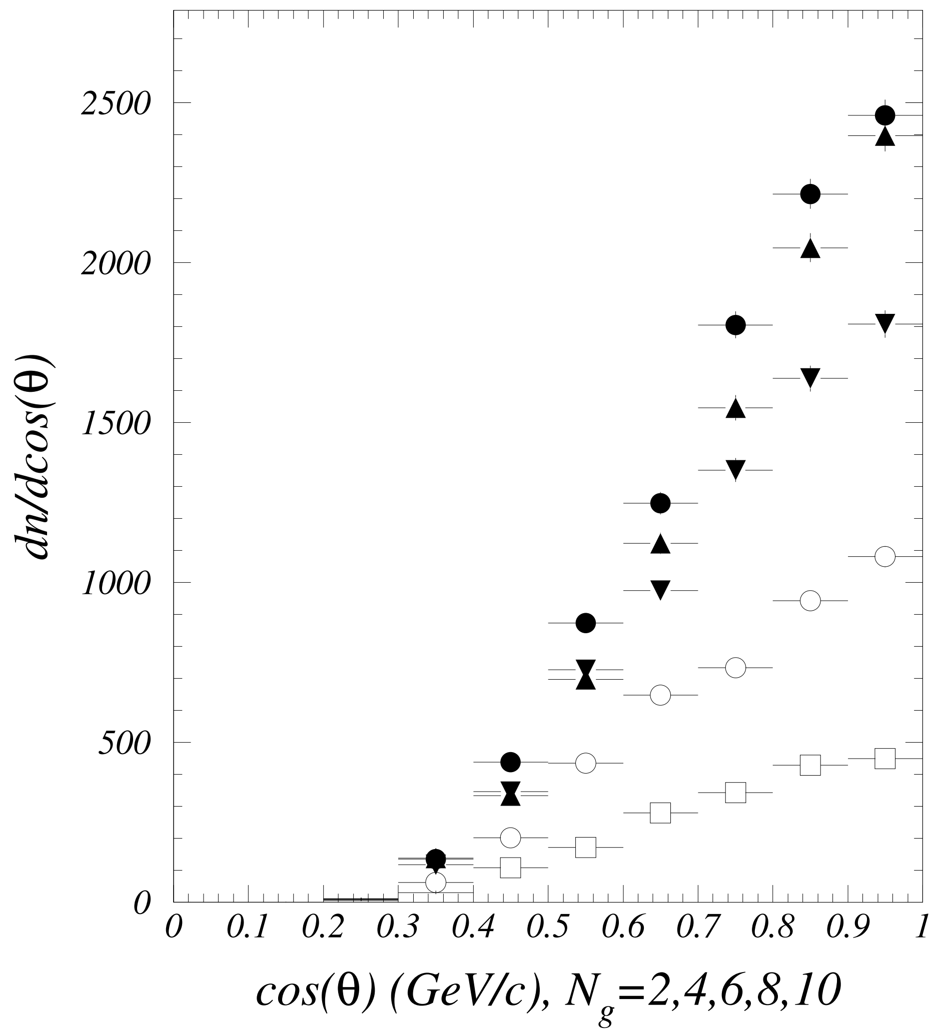

Figure 3.8: Angular distributions (not event-normalized) of grey particles for events with $N_g = 2$ (closed circles), 4 (closed triangles), 6 (closed upside-down triangles), 8 (open circles), 10 (open squares).

performed iteratively, according to Eq. 3.2,

$$P_{n+1}(N_g) = e^{\frac{x}{x_0}} P_n(N_g) - \frac{x}{x_0} \sum_{i=0}^{N_g} P_n(i) P_{measured}(N_g - i), \tag{3.2}$$

where x_0 is the p-A interaction length and x is the interaction thickness of the target. Convergence is rapid and only a few iterations are required. Corrections for tertiary interactions have been calculated and found to be negligible. The final distributions of slow protons and slow deuterons for all three targets are shown in Fig. 3.9.

3.3 Antiproton Analysis

3.3.1 Reduction of Scintillating Fiber Trigger Data

The antiproton analysis includes all sufficiently large data sets for which the scintillating fiber was used as the trigger. Large statistics are needed to do the analysis, and the majority of the data was taken with this trigger. The particular data sets that are sufficiently large for this analysis are the 18 GeV/c $p + Au$ data and the 12 GeV/c $p + Au$, $p + Cu$, and $p + Be$ data.

The scintillating fiber detector was placed directly downstream of the target. To reject interactions with the fibers rather than the target, there is a cut on the z-position of the primary vertex. Figure 3.10 shows the distribution of the z-position of the primary vertex. The large peak to the left of the line, which

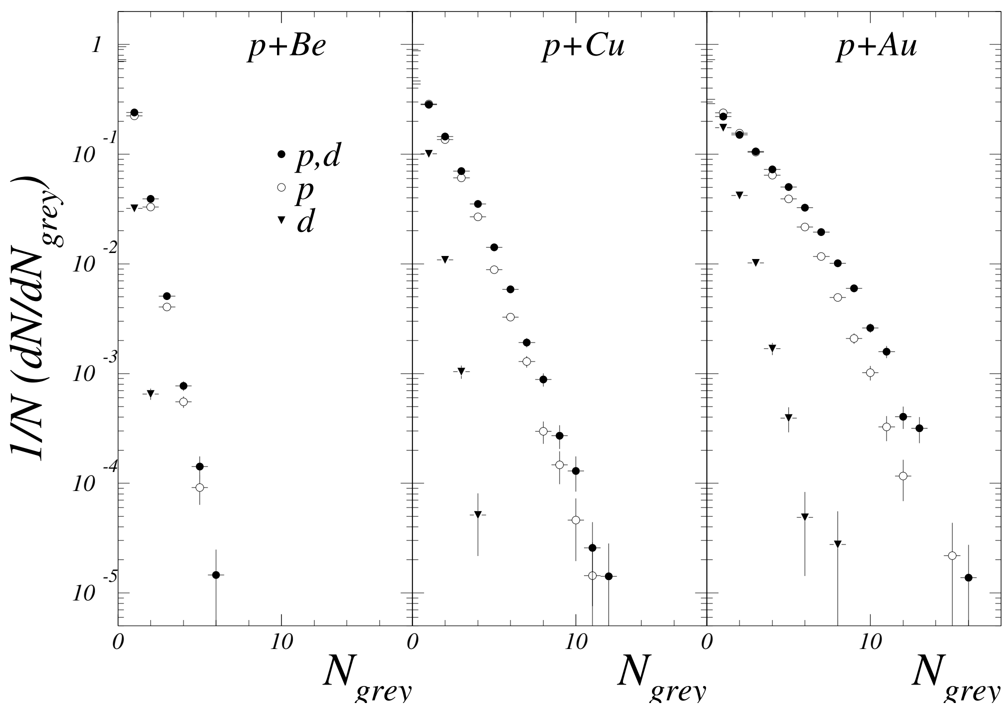

Figure 3.9: Event-normalized multiplicity distributions of protons (open circles), deuterons (triangles) and both protons and deuterons (dark circles).

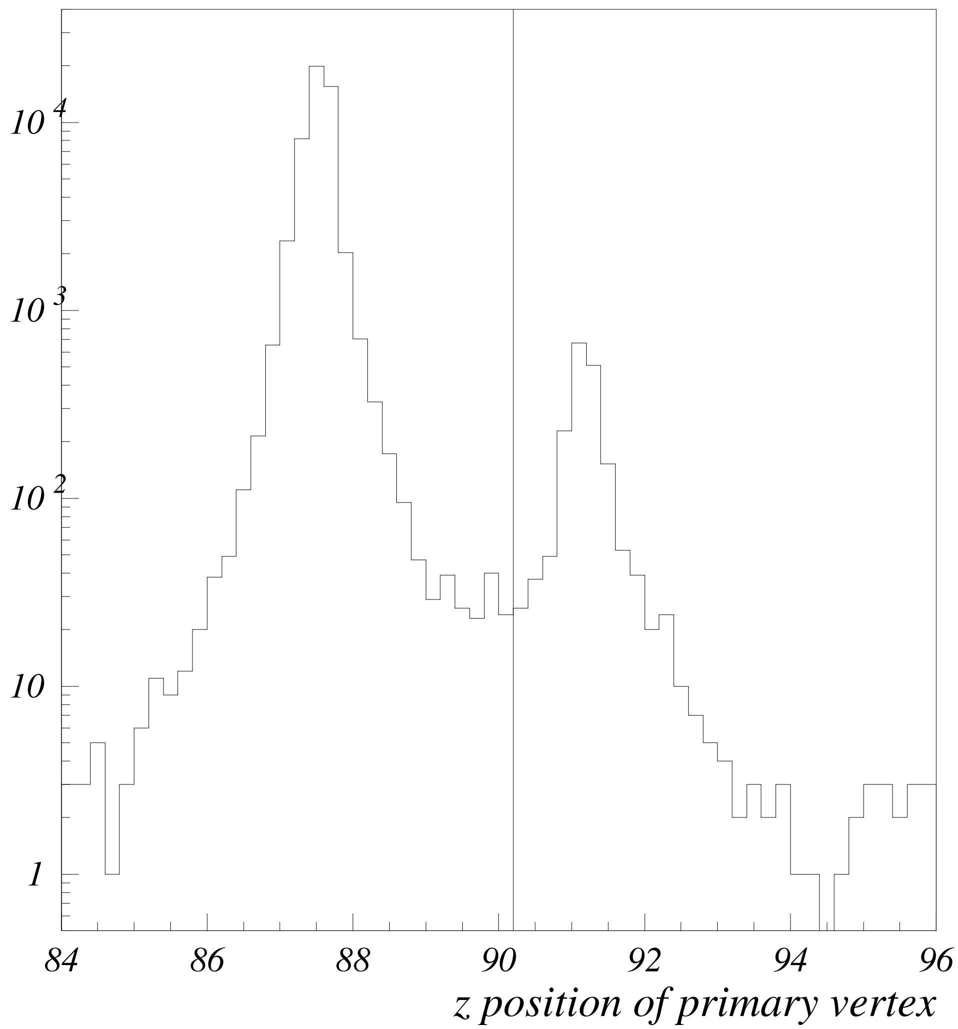

Figure 3.10: Distribution of z-position (in cm) of reconstructed event vertex (semi-log scale). The line indicates the position of the cut to reject interactions with scintillating fiber.

indicates the position of the cut for the 18 GeV/c beam momentum data, is at the z-position of the target. The peak to the right of the line is at the z-position of the scintillating fiber. To reject events with only the beam particle and elastic events, an event must have at least 2 charged particles or 1 charged particle with momentum less than 14.5 GeV/c (10.0 GeV/c for the 12 GeV/c beam momentum data) and transverse momentum greater than 90 MeV/c. For track quality, we require at least 10 hits in the time projection chamber (TPC) and that the track originated from the event vertex. To reduce background, we further require that the ionization energy loss is within 3 standard deviations of the proton dE/dx. In the relativistic rise region, the measured dE/dx must be greater than 1.5 standard deviations from the pion dE/dx. We also require that the CKOV did not fire. Quality cuts on the hits in the time-of-flight wall (TOF) include a cut on the difference in horizontal position between a swum track and the center of a hit TOF slat and a cut on the energy deposited in the TOF slat. A hit must be within 10 cm of the swum position of a track at the TOF wall. The energy deposited in the TOF slat must be greater than 0.7 times the gain peak and less than 1.7 times the gain peak.

All tracks are matched to the TOF wall with an 80% efficiency. To improve this efficiency, we imposed a cut on the number of hits in the drift chambers. Tracks with at least 5 hits in the drift chambers are accepted in the analysis. This cut increases the matching efficiency to $90\pm5\%$. The resulting matching efficiency calculated for all negative tracks originating from the primary vertex is shown in Fig. 3.11.

3.3.2 Identifying Antiprotons Using TOF

Antiprotons are identified using their time of flight. Figure 3.12 shows the momentum dependence of the difference between a track's measured time of flight and its expected time of flight assuming the particle is a proton. The particle bands are well separated up to 3.5 GeV/c. Momentum dependent cuts on the number of standard deviations of the measured time of flight from the expected time of flight of a proton are applied. Figure 3.13 shows the measured time of flight minus the expected time of flight for 0.5 GeV/c slices of momentum. The particle identification cuts are indicated with solid lines. Based on fits to these distributions, the background is estimated to be approximately 3-4%. The background counts versus signal counts within TOF particle identification cuts are given in Table 3.2 for each momentum slice.

3.3.3 Corrections to Data

The first correction applied to the data is the trigger efficiency correction. There were two trigger conditions for the scintillating fiber trigger, one for interactions and one for central interactions. These are described in Section 2.2. Each trigger condition has an efficiency dependent on the number of charged particles, $N_{charged}$,

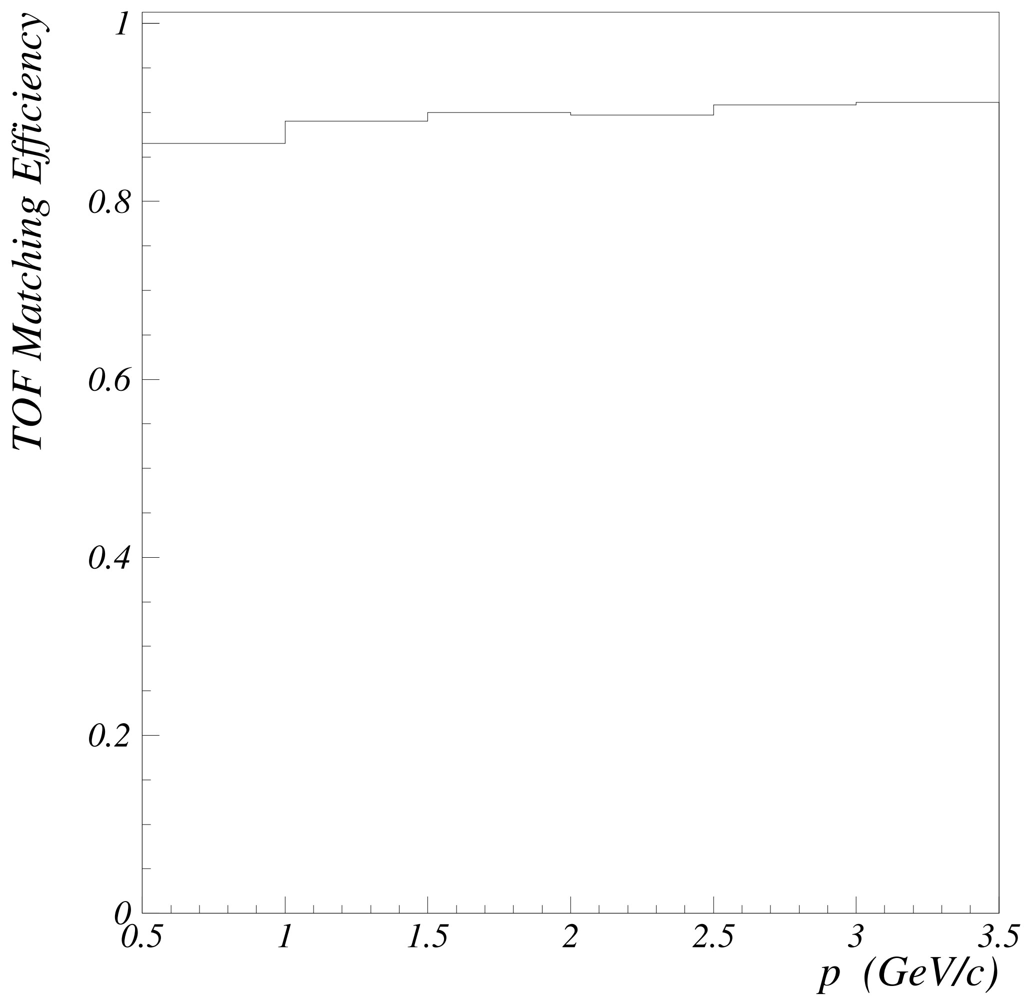

Figure 3.11: TOF matching efficiency.

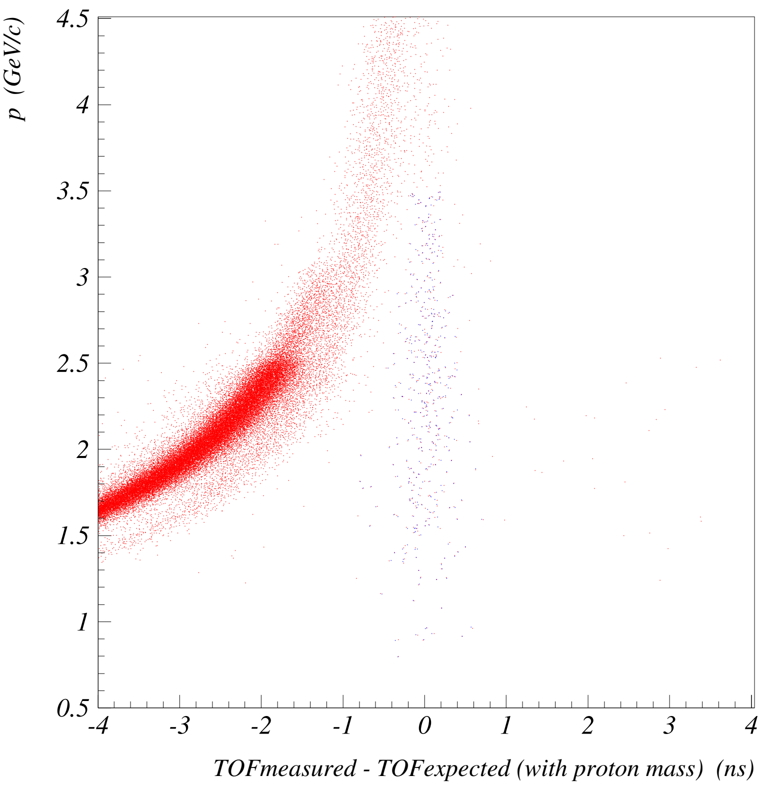

Figure 3.12: Particle identification of antiprotons for 18 GeV/c $p + Au$ data set.

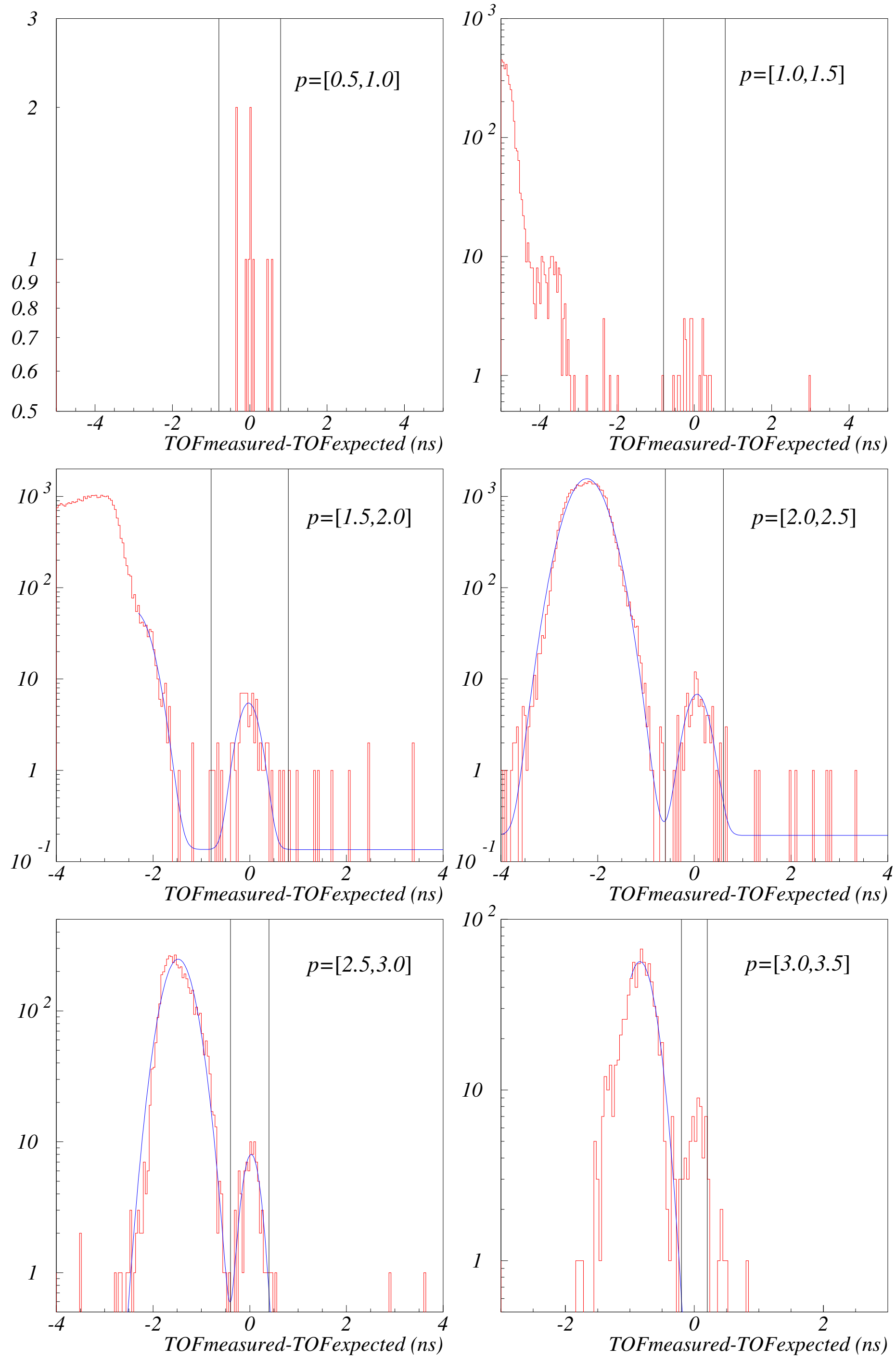

Figure 3.13: Particle identification cuts in slices of momentum (for 18 GeV/c $p + Au$ data set).

Table 3.2: Estimated background and $\overline{p}$ signal for each momentum slice based on fits shown in Fig. 3.13 (for 18 GeV/c $p + Au$ data set).

Momentum slice	Signal counts	Background counts
$0.5 < p < 1.0$ GeV/c	9	0
$1.0 < p < 1.5$ GeV/c	22	0
$1.5 < p < 2.0$ GeV/c	74	5.4
$2.0 < p < 2.5$ GeV/c	91	5.8
$2.5 < p < 3.0$ GeV/c	81	0
$3.0 < p < 3.5$ GeV/c	55	1

and the number of grey particles,N_g, in an event. The efficiency is calculated as a function of these two quantities using beam triggers. The data is corrected with the calculated efficiency based on the number of grey particles and the total number of charged particles in each event. The correction is most significant for events with $N_g = 0, 1, 2$ for interaction triggers and up to somewhat larger values of N_g for central triggers. For central triggers, the efficiency is so low for $N_g = 0$ events, that we do not include such events. Furthermore, central trigger events with $N_g = 1, 2$ in bins of $N_{charged}$ where the efficiency is less than 30% are also not included. The trigger efficiency is simply set to zero in these bins. After correction, the data must be weighted according to the scaledown of interaction triggers relative to central triggers. The scaledown factor was two, therefore the interaction trigger events are added to the central trigger events with a weight of two.

The acceptance for antiprotons is calculated with single track antiproton events generated through the E910 analysis program. The antiproton rapidity and transverse momentum are initialized by sampling from the uncorrected antiproton $y - p_T$ data distribution. Hits are simulated and tracks and momenta are reconstructed. Times of flight are simulated as well. The data are acceptance corrected within our $y - p_T$ coverage, which is shown in Fig. 3.14. In the $y = 1.0 - 1.2$ bin, the acceptance is slightly less than 10%, but there is still sufficient acceptance. Figure 3.15 shows the acceptance only in the region of $y - p_T$ where the acceptance is at least 8%, with the exception of the bin $1.8 < y < 2.0$, $0.7 < p_T < 0.8$ GeV/c. This bin has no acceptance because of the momentum cut, $p < 3.5$ GeV/c.

The data have also been corrected for the efficiencies of the following analysis cuts described above: the cut on the track's ionization energy loss in the TPC, the cut requiring that the CKOV did not fire, the cut on the difference between a TOF hit and the position of the swum track, the cut on the energy deposited in the TOF slat, and the cut on the number of hits in the drift chambers. The efficiency of these cuts is calculated with TOF-identified protons having times of flight within 400 ps of their expected times of flight, which is approximately 2.5 standard deviations. These measured times of flight are still well separated from the pion times of flight (see Fig. 2.6). Figure 3.16 shows the efficiency of the cuts in the 18 GeV/c $p + Au$ data set. It varies from 60% to 80% as a function of the transverse momentum. It is not dependent on rapidity.

The acceptance and efficiency corrected distributions are shown in Figs. 3.17

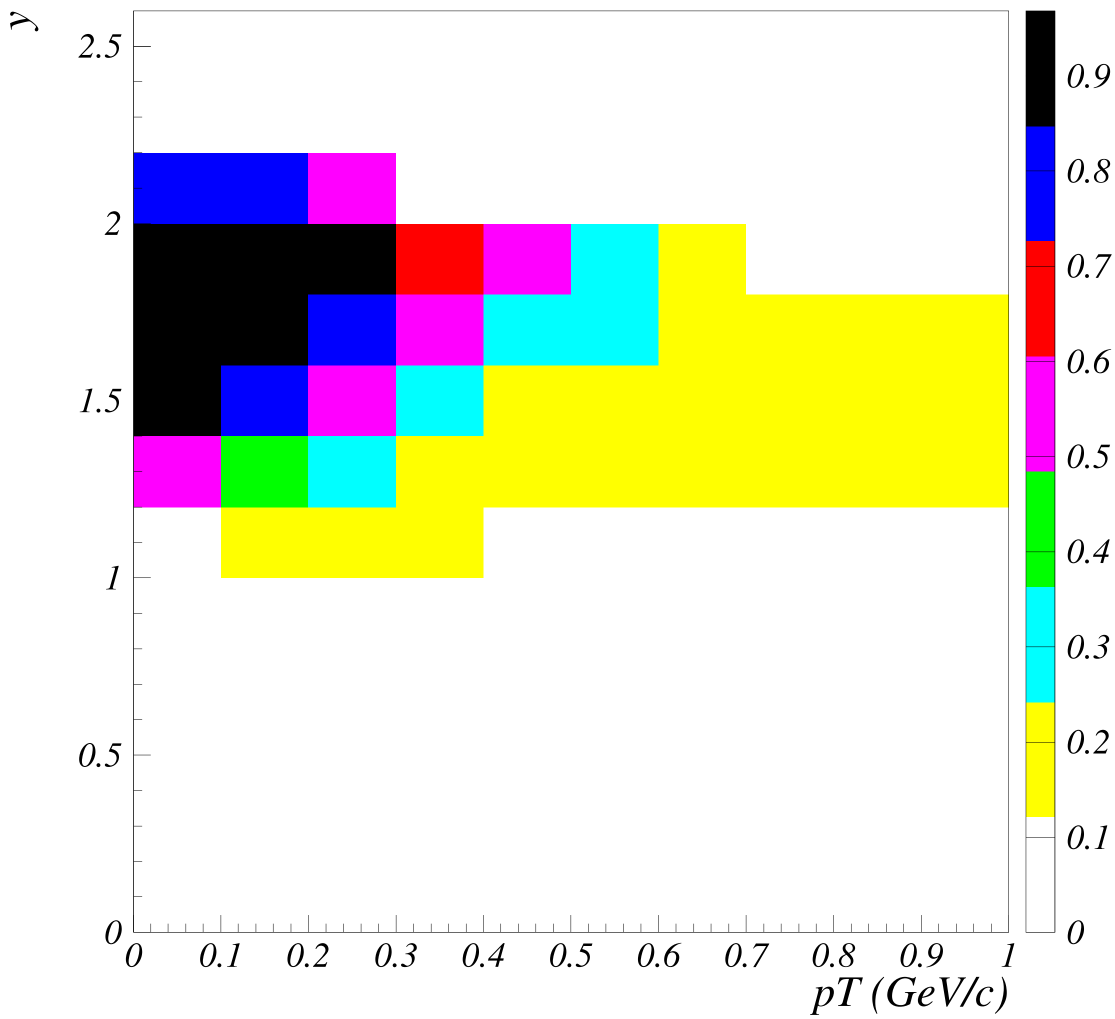

Figure 3.14: TOF acceptance.

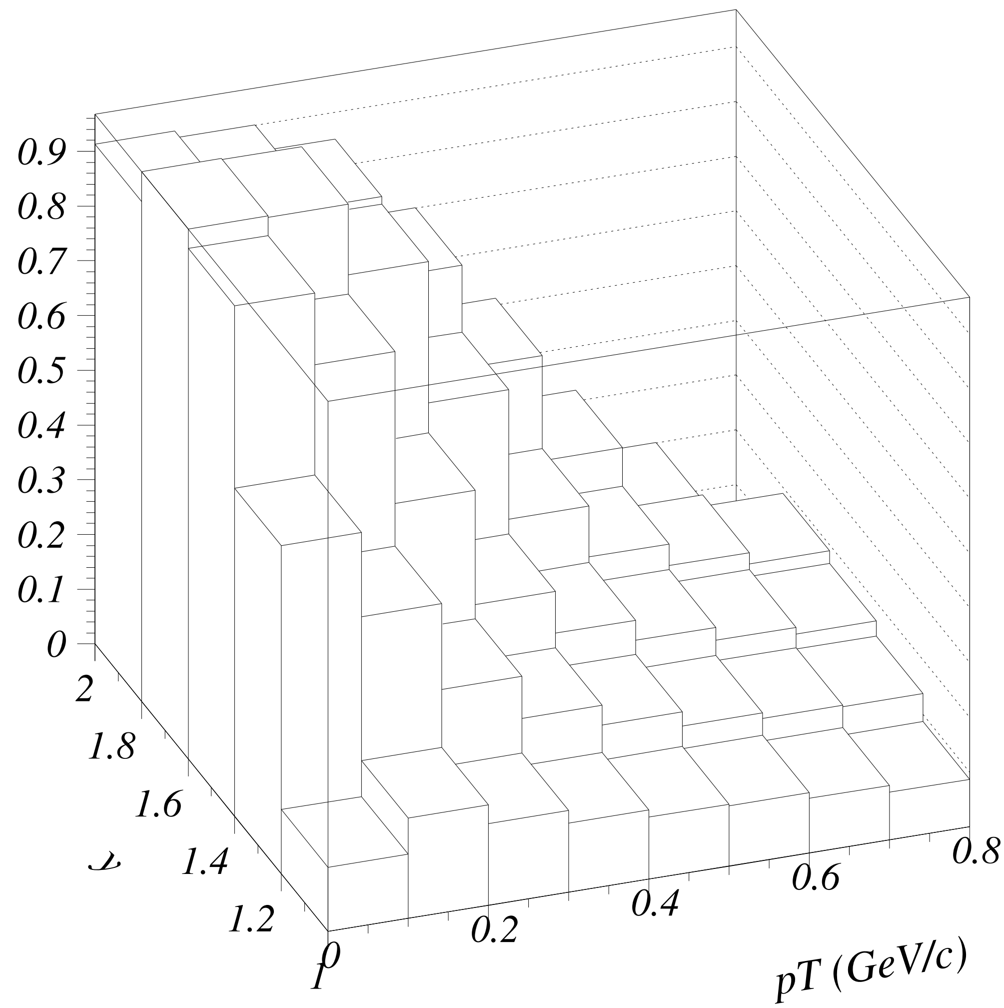

Figure 3.15: TOF acceptance for 10 $MeV/c < p_T < 0.8\ GeV/c$ and $1 < y < 2$ ($y - p_T$ region where acceptance is greater than 8%).

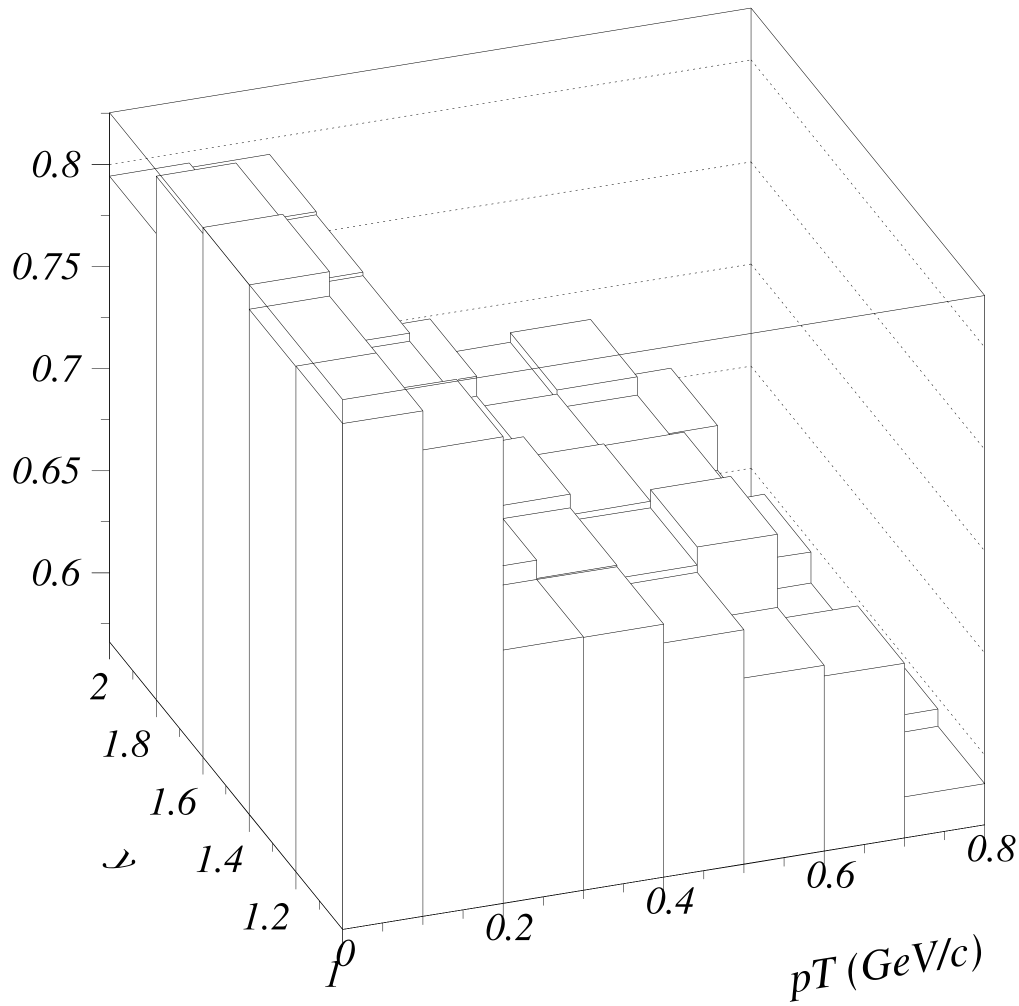

Figure 3.16: Efficiency of analysis cuts for 10 $MeV/c < p_T < 0.8$ GeV/c and $1 < y < 2$.

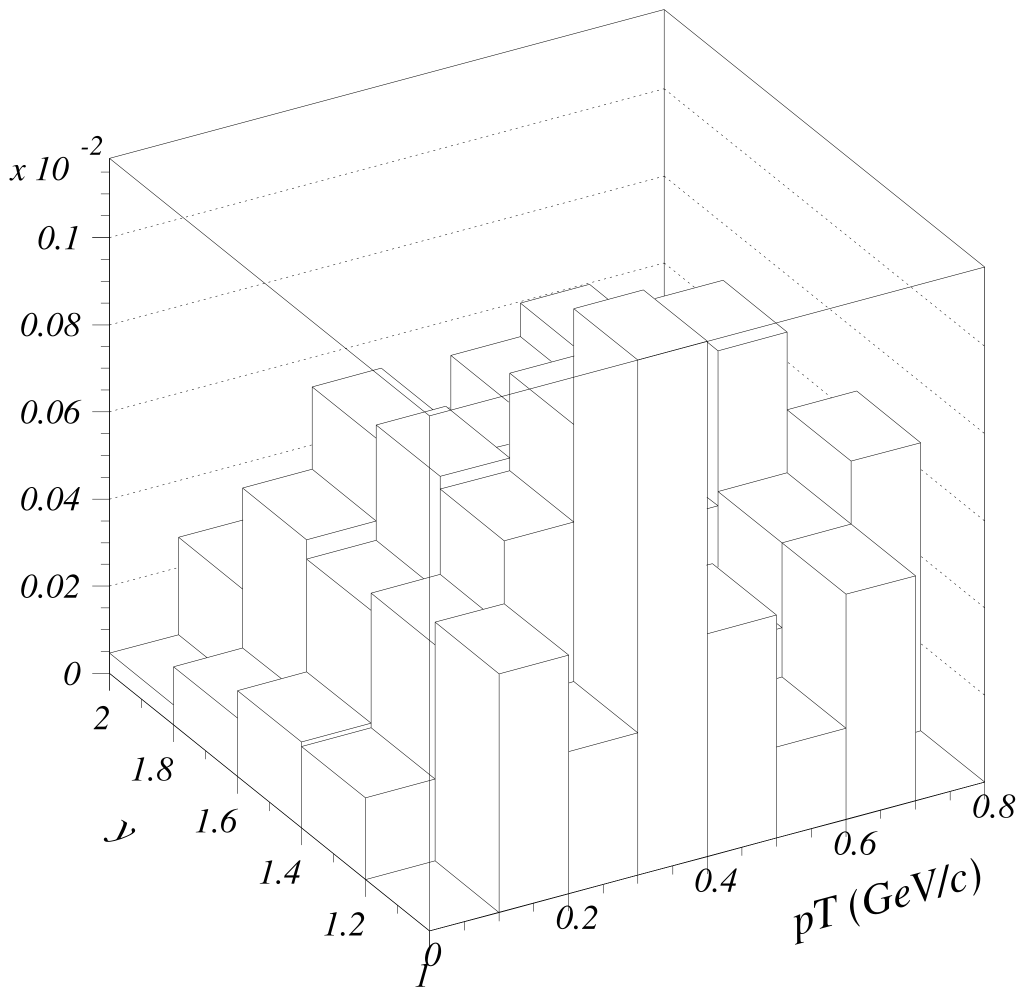

Figure 3.17: Acceptance and efficiency corrected, event-normalized $y - p_T$ distribution for 18 GeV/c $p + Au$ data.

and 3.18.

3.3.4 Antihyperon Contamination

A possible source of contamination to our sample of primordial antiprotons is antiprotons that are daughters of antihyperon decays. The main contribution to such contamination would be $\overline{\Lambda}$ (1116) decays. The most effective cut to reject antiprotons from decays is the requirement that a track is associated with the primary vertex. However, approximately 30% of the antiprotons in the 18 GeV/c $p + Au$ data set are also associated with a secondary vertex. The E910 cuts that associate secondary vertices are too loose to reject tracks associated with them. To investigate the $\overline{\Lambda}$ contamination, the invariant mass has been calculated for all pairs from possible secondary vertices for which an identified antiproton has been associated. Figure 3.19 shows this invariant mass distribution with the solid lines showing a window of 2 FWHMs centered on the mean mass of the $\overline{\Lambda}$ and the dashed lines showing a FWHM wide region outside of this window on each side. There are 16 counts within the window and 16 counts outside of the window, indicating no enhancement in the $\overline{\Lambda}$ mass region. The FWHM is calculated from the parameters resulting from the fits to the lambda invariant mass distribution shown in Fig. 3.20, using an analysis done by Xihong Yang [29].

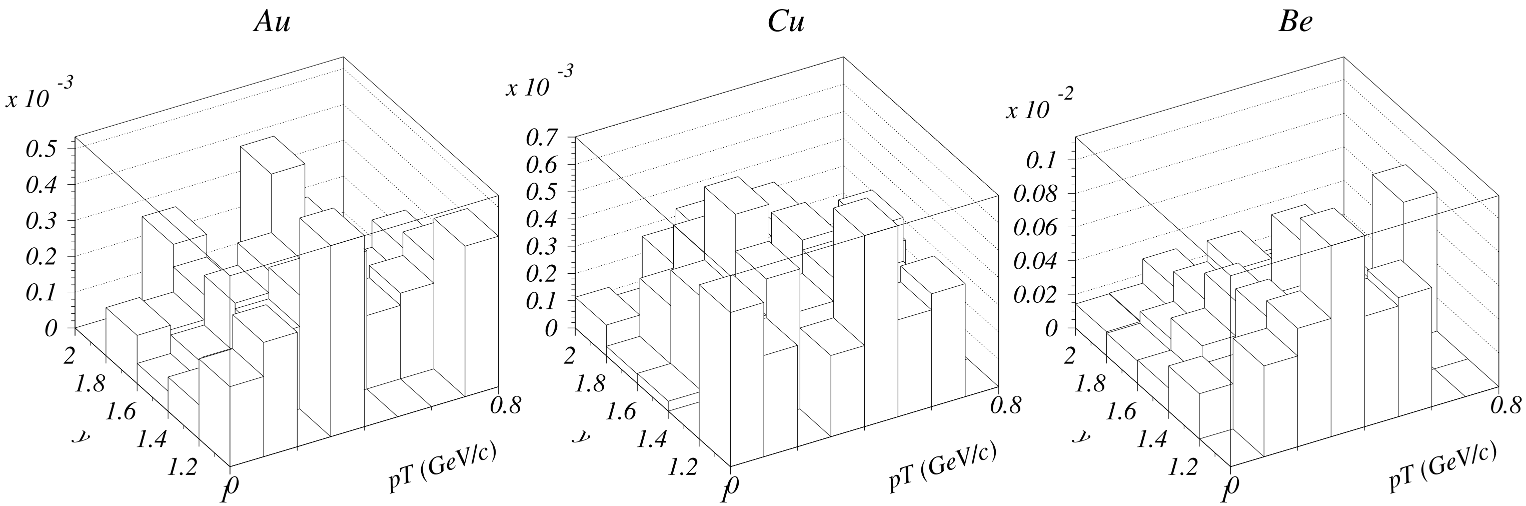

Figure 3.18: Acceptance and efficiency corrected, event-normalized $y - p_T$ distributions for 12 GeV/c $p + Au$, $p + Cu$, $p + Be$ data.

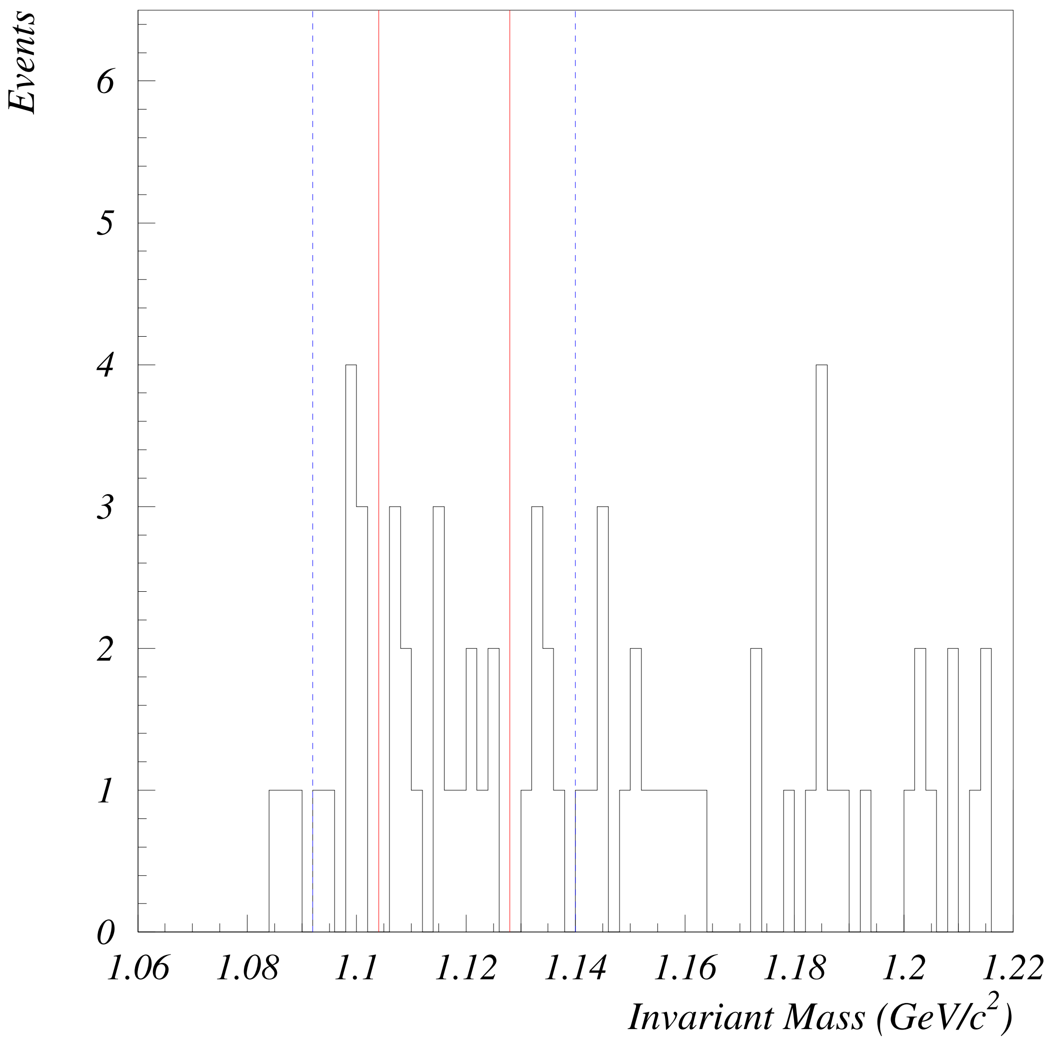

Figure 3.19: Invariant mass distribution of TOF-identified $\overline{p}$ and assumed π^+ associated with possible secondary vertices.

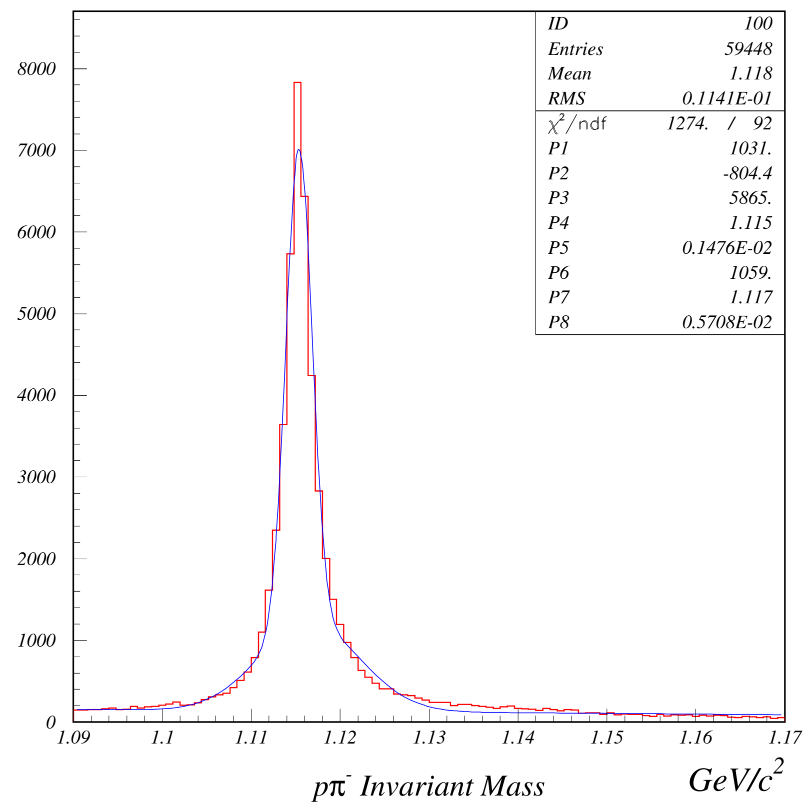

Figure 3.20: Invariant mass distribution of $p\pi^-$ pairs (courtesy of Xihong Yang [29]).

3.3.5 Systematic Errors

The largest source of systematic error is estimated to be the correction for the TOF matching inefficiency. The efficiency to match tracks swum through the magnetic field to the TOF wall with hits in the TOF is calculated for all negative tracks. Antiprotons may have a different matching efficiency than the negative pions. However, the negative tracks have a more similar hit distribution in x to the antiprotons than the positive tracks. Thus, it makes more sense to estimate the matching efficiency for antiprotons using negative tracks. The $y - p_T$ distributions for antiprotons are corrected uniformly for the calculated matching efficiency of 90%. The uncertainty in this correction is estimated to be 5%. The error associated with this correction is still small compared to the statistical errors. The uncertainty in our measurements is dominated by statistical errors.

Chapter 4

Using Slow Protons to Characterize Events

4.1 Centrality of $p + A$ Collisions

In studying the physics processes that occur in proton-nucleus collisions, we are interested in characterizing the "violence," or centrality, of a collision. In nucleus-nucleus collisions, the centrality of a collision is defined by the impact parameter which is deduced from the transverse energy or charged particle multiplicity measured in the event. The impact parameter is a measure of the violence of a $A + A$ collision because it is strongly correlated to the amount of participant versus spectator nuclear matter. In proton-nucleus collisions, the impact parameter is not so strongly correlated to the amount of participant matter; the number of collisions that the projectile undergoes within the nucleus is a better indication of the number of participants. Thus, the more appropriate definition of centrality in $p + A$ collisions is the number of projectile collisions, ν. This quantity is quite important because it can be used to characterize physical processes that occur within the nucleus with each collision that the projectile undergoes. It also provides a convenient method of relating measurements made with different target sizes to each other.

4.2 Using Slow Protons to Determine ν

As a result of the projectile collisions within the nucleus, nucleons are knocked out. Historically, from emulsion experiments, these knocked out particles were called "grey tracks." They are made up of mostly protons and deuterons and are emitted as a result of primary collisions, collisions between the projectile and target nucleons, secondary collisions, which are collisions between nucleons struck by the projectile and other target nucleons, and even tertiary or subsequent collisions in the cascade. The grey tracks are to be distinguished from the "black tracks," which are the evaporative fragments. They are called "black tracks" because they have a higher grain density than the grey tracks in an emulsion experiment. They are made up of protons, deuterons, and larger fission fragments and are more isotropically emitted than the grey tracks. In our experiment, we distinguish the "grey" particles from the evaporative fragments via the lower momentum cut discussed in Section 3.2.

The first emulsion experiment to relate the number of grey tracks, N_g, to the number of projectile collisions, ν, is described in reference [30]. The grey tracks were made up of mostly protons and deuterons with momenta between 0.3 and 1.0 GeV/c. Subsequently, this type of analysis was also done by counter exeriments [31, 32] and streamer/bubble chamber experiments [33, 34, 35, 36].

4.3 Analysis to Determine ν

E910 measures both slow protons and slow deuterons. Slow protons have momenta within $0.25 < p < 1.2$ GeV/c, and slow deuterons have momenta within $0.5 < p < 2.4$ GeV/c. Figures 4.1, 4.2, and 4.3 show the event-normalized number distributions of slow protons, slow deuterons, and both slow protons and deuterons for different targets.

To relate the number of grey particles, N_g, to the number of projectile collisions ν for a target with mass number A, we can write

$$P^A(N_g) = \sum_{\nu} \pi_A(\nu) P_{\nu}^A(N_g). \tag{4.1}$$

The probability distribution of ν, $\pi_A(\nu)$, can be calculated for a nucleus with mass number A using the Glauber Model [7]. The mean number of collisions is obtained

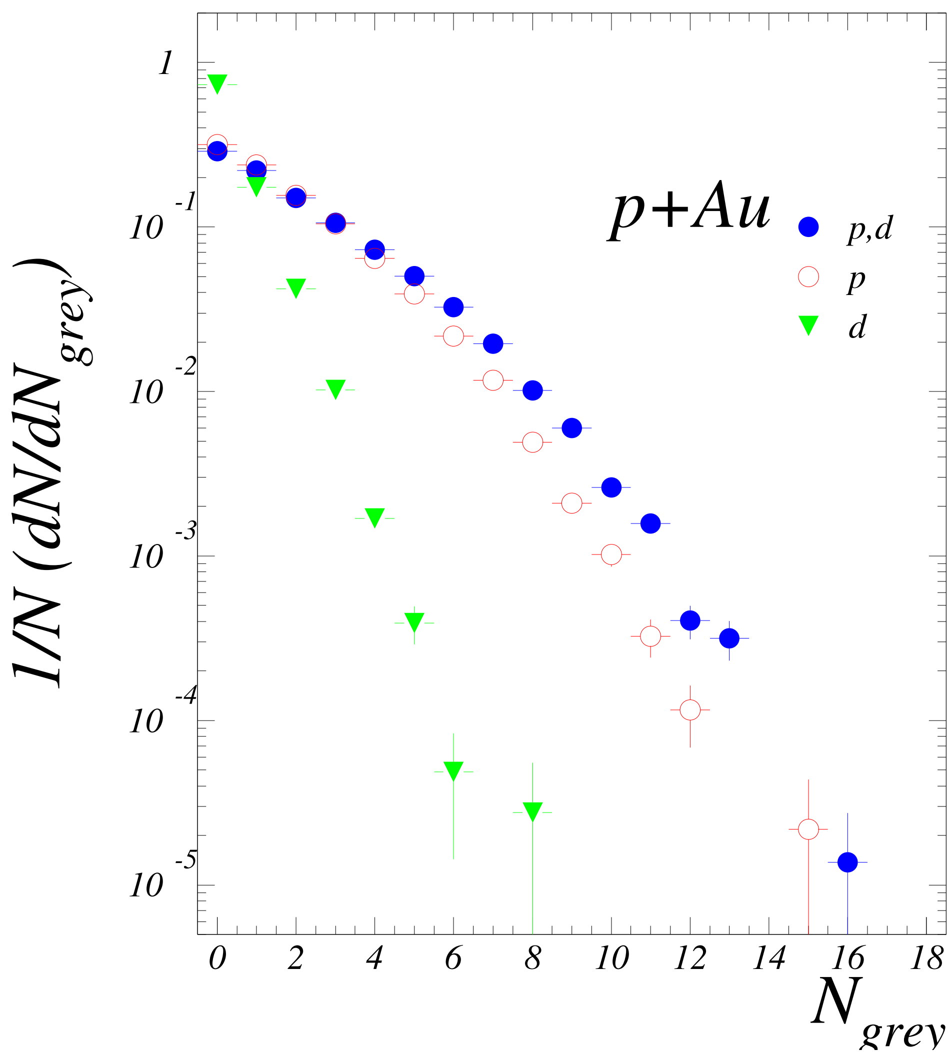

Figure 4.1: Event-normalized grey particle multiplicity distribution, $P(N_g)$, for Au nucleus.

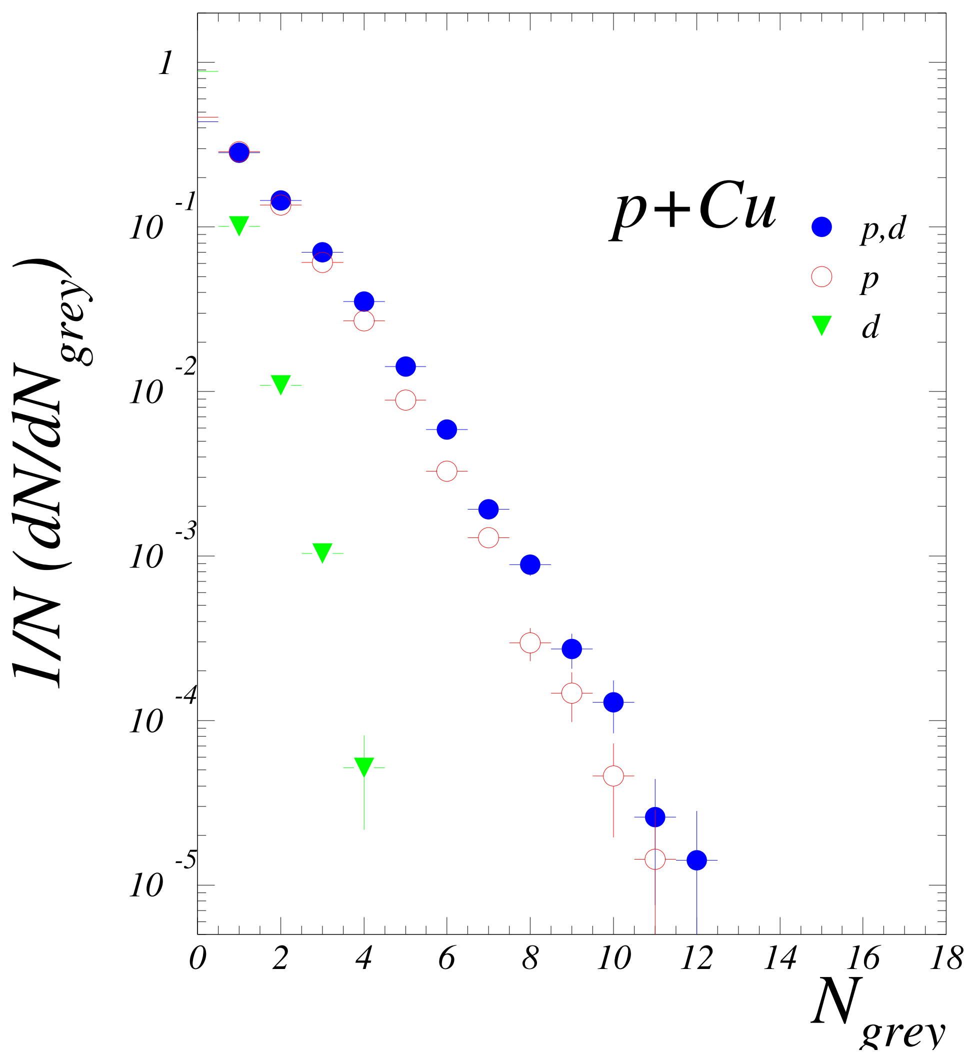

Figure 4.2: Event-normalized grey particle multiplicity distribution, $P(N_g)$, for Cu nucleus.

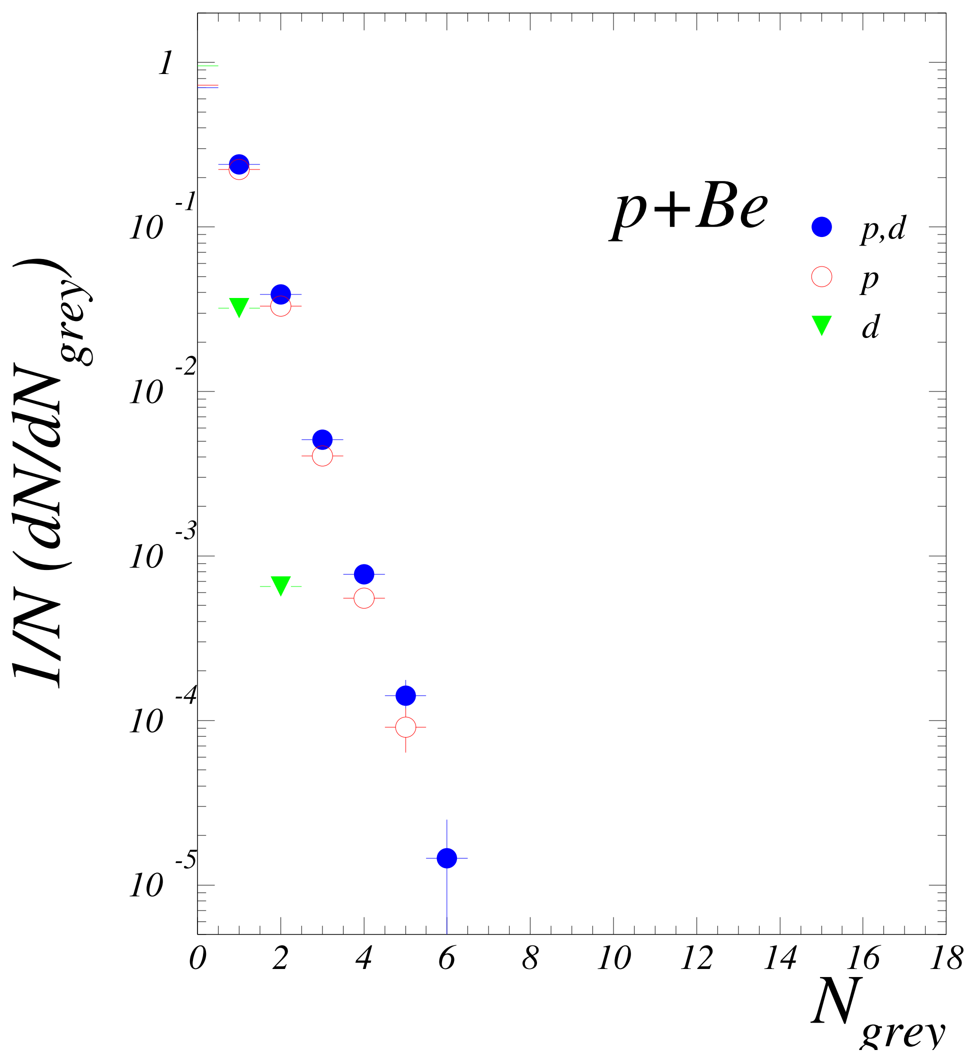

Figure 4.3: Event-normalized grey particle multiplicity distribution, $P(N_g)$, for Be nucleus.

from the following equation,

$$\overline{\nu} = \sigma_{NN} \int_{-\infty}^{\infty} \rho(z, b) dz, \tag{4.2}$$

by sampling over impact parameters within the range of the radius of the nucleus. The probability distribution is calculated with a binomial distribution with average value, $\overline{\nu}$. In this calculation, we assume a Woods-Saxon potential and an inelastic cross section of 30 mb. The calculation is done within the framework of the Hijing Model [37], an event generator based on the LUND geometry. The results of the calculation are shown in Fig. 4.4. As a comparison, the Glauber calculation was also done outside of the Hijing framework which is shown in Appendix A. There is very little difference.

The distribution, $P_{\nu}^{A}(N_g)$, is also model dependent. We have used two different models with somewhat different assumptions. The first is the Geometric Cascade Model (GCM) [38]. The GCM assumes that the number of grey particles "knocked out" as a result of the first projectile collision follows a geometric distribution.

$$P_{\nu=1}(N_g) = (1-X)X^{N_g}, \quad X = \frac{(< N_g >_A / < \nu >_A)}{(1+ < N_g >_A / < \nu >_A)}, \tag{4.3}$$

The other assumption is that every collision knocks out the same number of grey particles. Thus, the distribution of grey particles for ν independent interactions

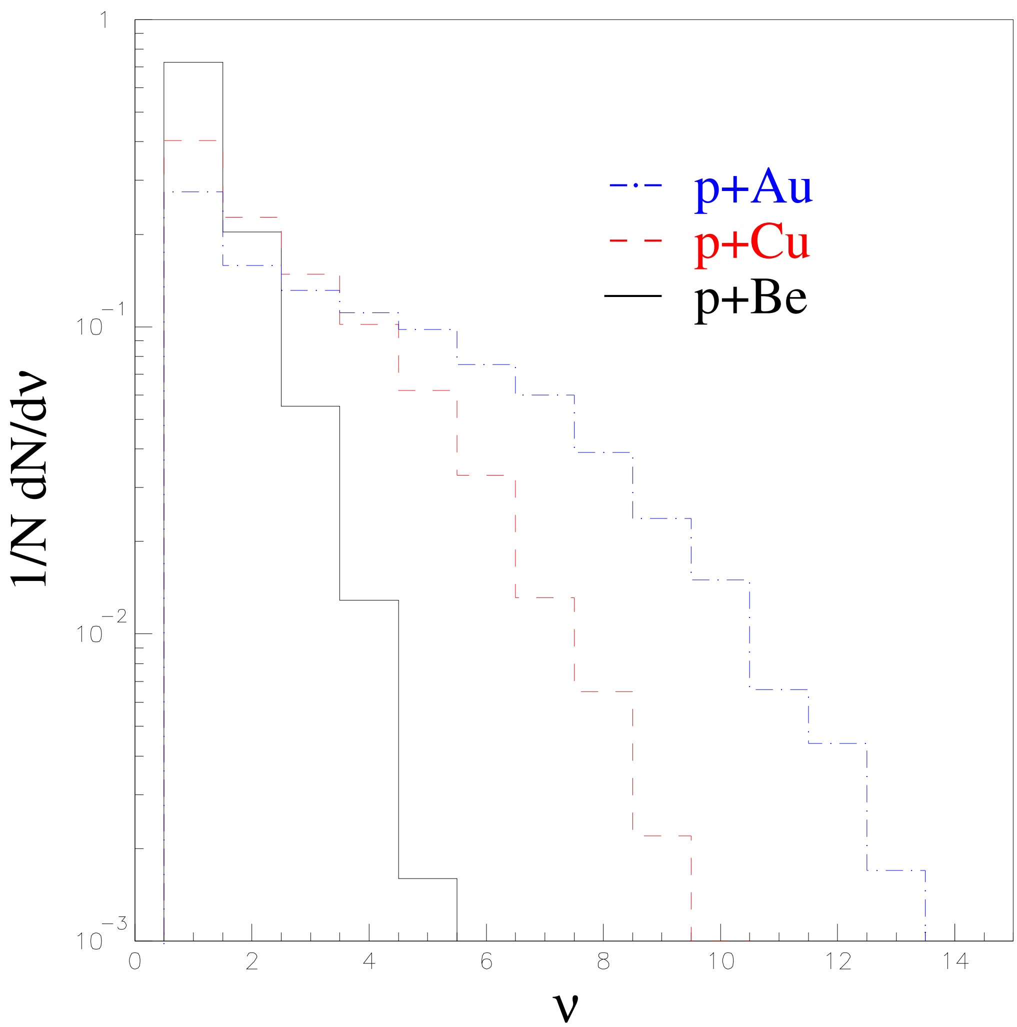

Figure 4.4: Probability distribution of ν, $\pi_A(\nu)$, from Hijing Glauber calculation, where A = 9, 65, and 197.

becomes

$$P_\nu^A(N_g) = \begin{pmatrix} N_g + \nu - 1 \\ \nu - 1 \end{pmatrix} (1-X)^\nu X^{N_g}. \tag{4.4}$$

This is a negative binomial distribution.

The full distribution of $P^A(N_g)$ is given by a weighted sum over $\pi(\nu)$, (Eq. 4.1). The fits to $P(N_g)$ for all three targets are shown in Fig. 4.5 with the dashed lines. The results of the fits are given Table 4.1. The mean number of collisions for a given number of grey particles is then given by,

$$\overline{\nu}(N_g) = \frac{\sum\limits_\nu \nu P_\nu(N_g)\pi(\nu)}{\sum\limits_\nu P_\nu(N_g)\pi(\nu)}. \tag{4.5}$$

The right panels of Fig. 4.6 show these values of $\overline{\nu}(N_g)$ as well as the dispersions as a function of N_g for all three targets. The GCM has been used by several experiments successfully to characterize data [38, 30, 33, 34, 39, 31].

Historically, an alternate model related the number of collisions to the number of grey tracks with a quadratic relationship proposed by Hegab and Hüfner [40, 41],

$$\overline{N_g}(\nu) \propto \nu^2. \tag{4.6}$$

The assumptions leading to this relationship are that each nucleon struck by the projectile follows the same trajectory as the projectile and that each secondary collision, as well as a fraction of the primary collisions, contributes to N_g. This

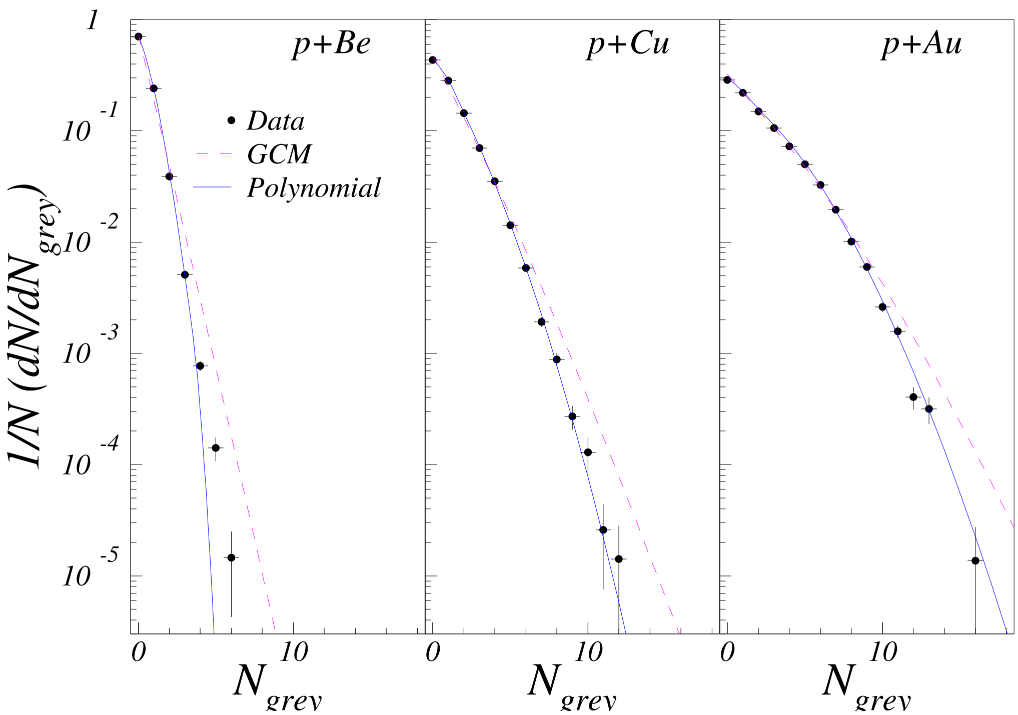

Figure 4.5: GCM (dashed) and Polynomial (solid) fits to $P(N_g)$ distributions.

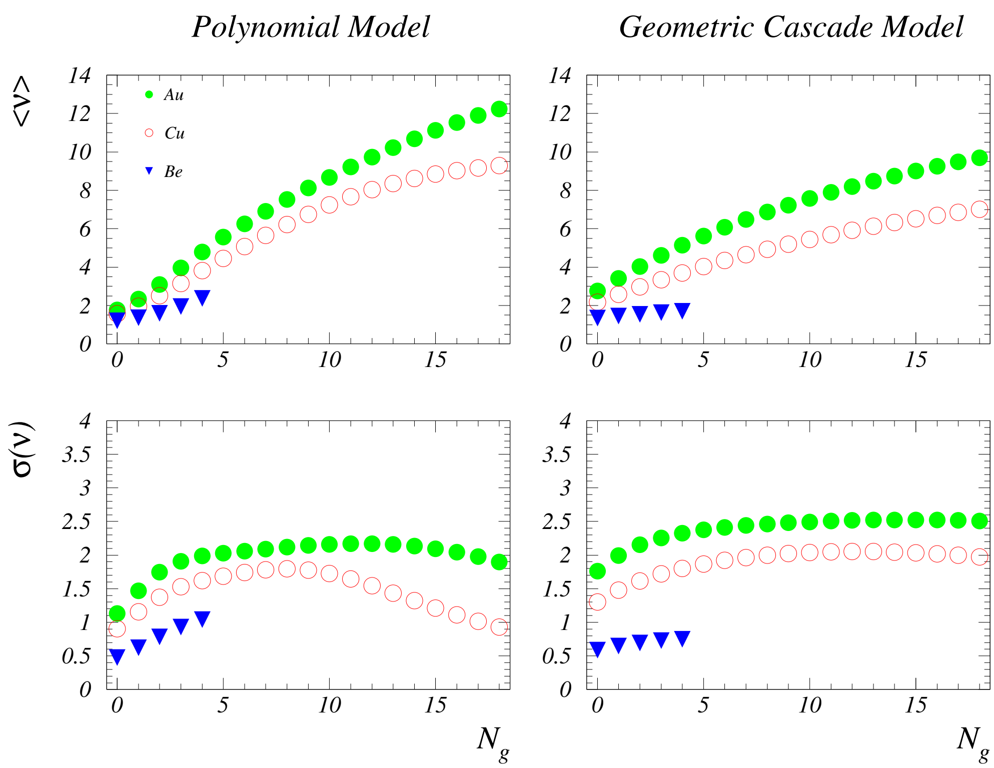

Figure 4.6: Extracted $\overline{\nu}(N_g)$.

Table 4.1: Mean values for N_g, ν and GCM fit parameters.

Target	$< N_g >$	$< \nu >$	$X(\frac{<N_g>}{<\nu>})$	$X_{\rm fit}$	χ^2/dof
Au	1.98	3.63	0.353	0.351 ± 0.001	$3.04 \cdot 10^4/15$
Cu	1.06	2.40	0.306	0.306 ± 0.001	910/12
Be	0.342	1.36	0.201	0.201 ± 0.001	4007/6

contradicts the linear relationship assumed in the GCM. It has also been successfully used to describe the data in some experiments [41, 35]. This model is applied differently than the GCM. The mean number of collisions for a given number of grey particles is given by,

$$\overline{\nu}(N_g) = \overline{\nu}\sqrt{N_g/\overline{N_g}}, \tag{4.7}$$

where $\overline{\nu}$ is the overall mean number of projectile collisions for a given target (the mean of $\pi_A(\nu)$) and $\overline{N_g}$ is the measured mean number of grey particles for a given target.

Motivated by the difference in these two models used in the literature, we proposed another model which allows for both a linear and quadratic dependence of N_g on ν in the form of a second degree polynomial [42]:

$$< N_g >_\nu = c_0 + c_1\nu + c_2\nu^2. \tag{4.8}$$

Contrary to the GCM, this "Polynomial Model" allows one collision to be unique and includes a ν^2 dependence. The other assumption of the Polynomial Model is that the distribution of "knocked out" grey particles is governed by binomial statistics. In a nucleus of Z target protons, each can be emitted and detected with probability $< N_g > /Z$,

$$P_\nu^A(N_g) = \begin{pmatrix} Z \\ N_g \end{pmatrix} \frac{< N_g >_\nu}{Z} \left(1 - \frac{< N_g >_\nu}{Z}\right)^{Z-N_g} . \tag{4.9}$$

The fits to $P_A(N_g)$ using the Polynomial Model are shown in Fig. 4.5 with the solid lines. This figure shows that the Polynomial Model fits the data better than the GCM. The fit results are given in Table 4.2. The quadratic coefficients of the fits for the Au and Cu targets were determined to be nearly zero. The distribution for the Be target does not have large enough values of N_g to allow both a linear and quadratic coefficient. Therefore, the quadratic component was constrained to be zero for the Be data.

The left panels of Fig. 4.6 show the mean number of collisions and the dispersions as a function of N_g for all targets calculated using the Polynomial Model. The extracted $\overline{\nu}(N_g)$ for the two different models agree within their calculated dispersions. The dispersions for both models are relatively large and reflect the width of the correlation. The calculated numbers of projectile collisions as a function of the number of grey particles using both models are shown for the Au target in Fig. 4.7. This figure shows that the relation between N_g and ν extracted from the data is not a tight correlation.

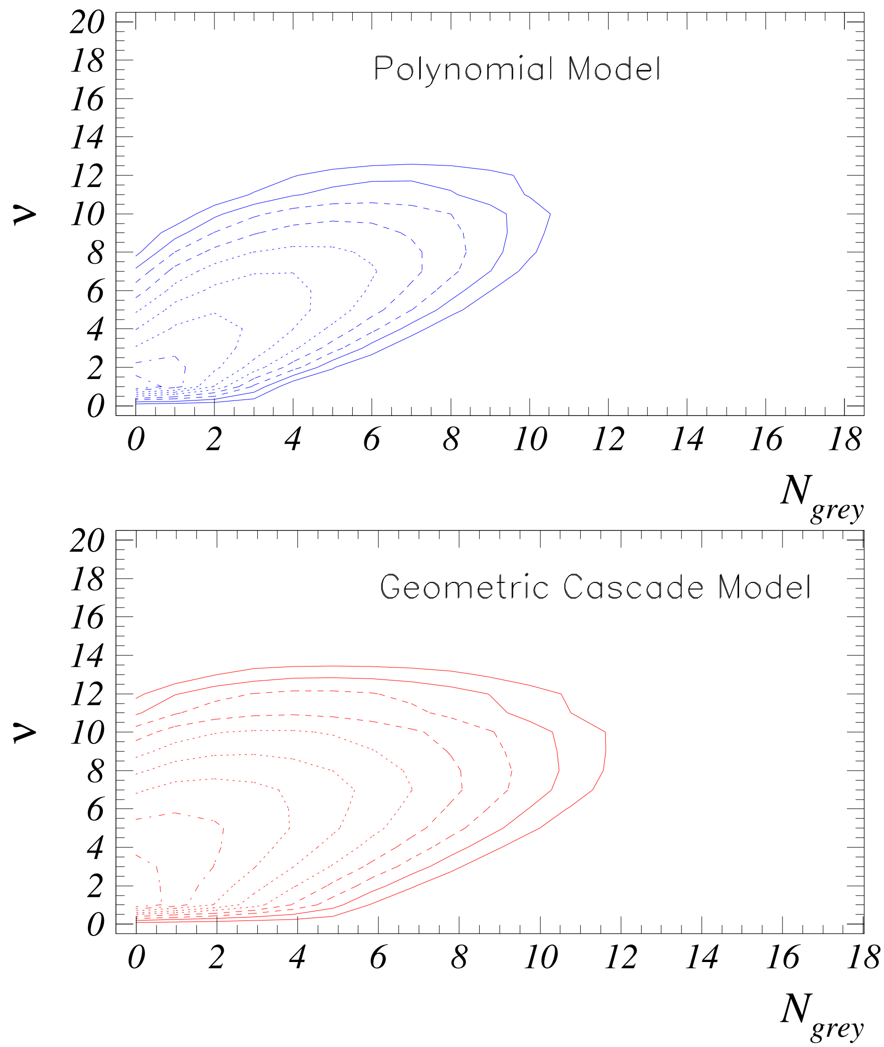

Figure 4.7: Extracted $\nu(N_g)$.

Table 4.2: Coefficients for polynomial fit to N_g.

Target	c_0	c_1	c_2	χ^2/dof
Au	-0.27 $\pm$ 0.02	0.63 $\pm$ 0.01	-0.0008 $\pm$ 0.0012	1639/13
Cu	-0.17 $\pm$ 0.02	0.51 $\pm$ 0.02	-0.00005 $\pm$ 0.00242	15/10
Be	-0.075 $\pm$ 0.008	0.306 $\pm$ 0.006	—	95/5

4.4 Model Comparisons

Of course, the number of collisions that the projectile undergoes in an event cannot be determined in the experiment. In a transport model, however, the number of projectile collisions is known. This makes it interesting to apply our simple models (the GCM and the Polynomial Model) to the $P(N_g)$ distribution produced by a transport model, such as RQMD, and compare our resulting $\overline{\nu}(N_g)$ to the actual $\overline{\nu}(N_g)$ inherent in RQMD. In this section, this analysis is performed on the output of RQMD.

First, the $P(N_g)$ distribution produced by RQMD is examined to determine whether RQMD is a reasonable model resembling the data. Figure 4.8 compares our measured $P(N_g)$ distribution to that obtained by imposing our experimental acceptance on the output of RQMD. In RQMD, there are no deuterons, so $P(N_g)$ is only the number of slow protons. Figure 4.8 shows that the distribution of slow protons in RQMD, with our experimental acceptance imposed, agrees well with the distribution of grey particles in our data.

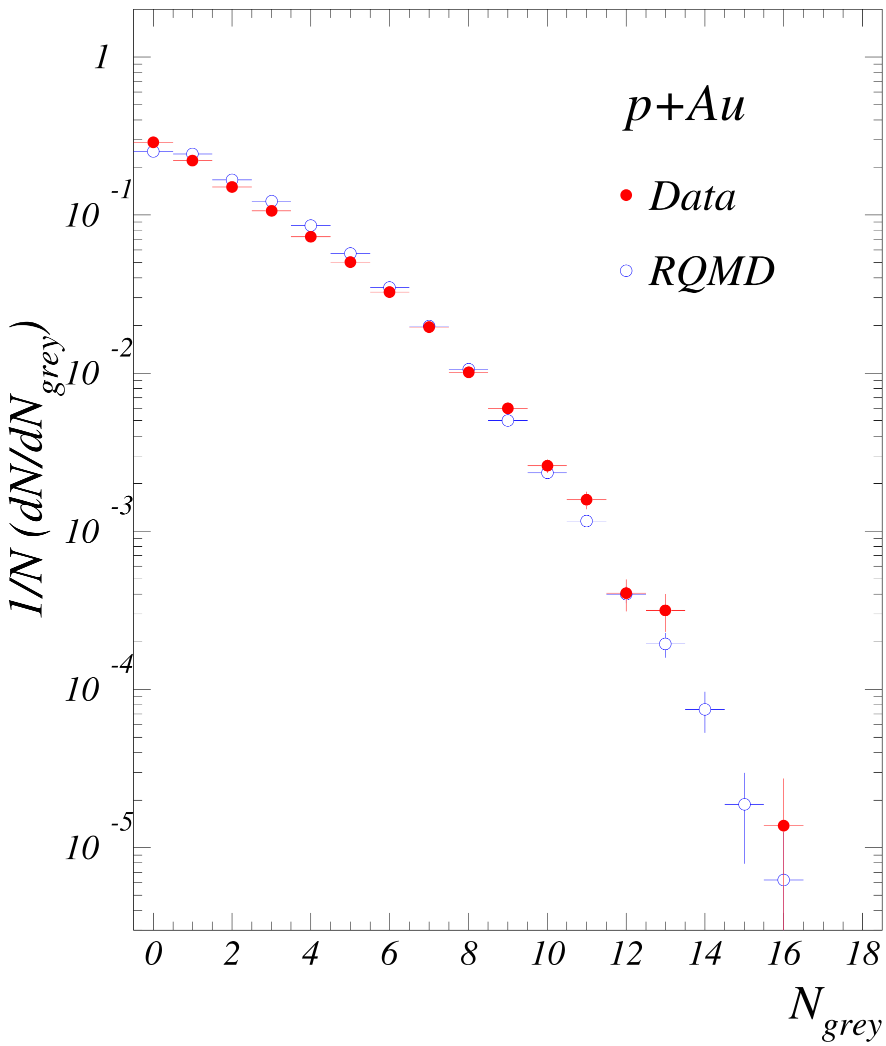

Figure 4.8: RQMD N_g multiplicity distribution for Au nucleus compared to data.

The RQMD $P(N_g)$ distributions both within our acceptance and for 4π acceptance (no acceptance cuts) are fit with the GCM and the Polynomial Model. The fits are done with the Hijing $\pi(\nu)$ distribution just as was done with the data. The results of the extracted $\overline{\nu}(N_g)$ are shown in Fig. 4.9. The left panels are those extracted for $P(N_g)$ within our acceptance and the right panels are for 4π acceptance. The extracted $\overline{\nu}(N_g)$ from the GCM and the Polynomial Model are compared to the intrinsic $\overline{\nu}(N_g)$, where the intrinsic ν is the number of projectile collisions that are counted in the RQMD history file (as described in Appendix A). For small values of N_g, the Polynomial Model agrees better with the RQMD inherent relation between N_g and ν. For larger values of N_g, the GCM has better agreement. Both models agree within the uncertainty given by the dispersion in $\nu(N_g)$, $\sigma(N_g)$, shown in the bottom panels.

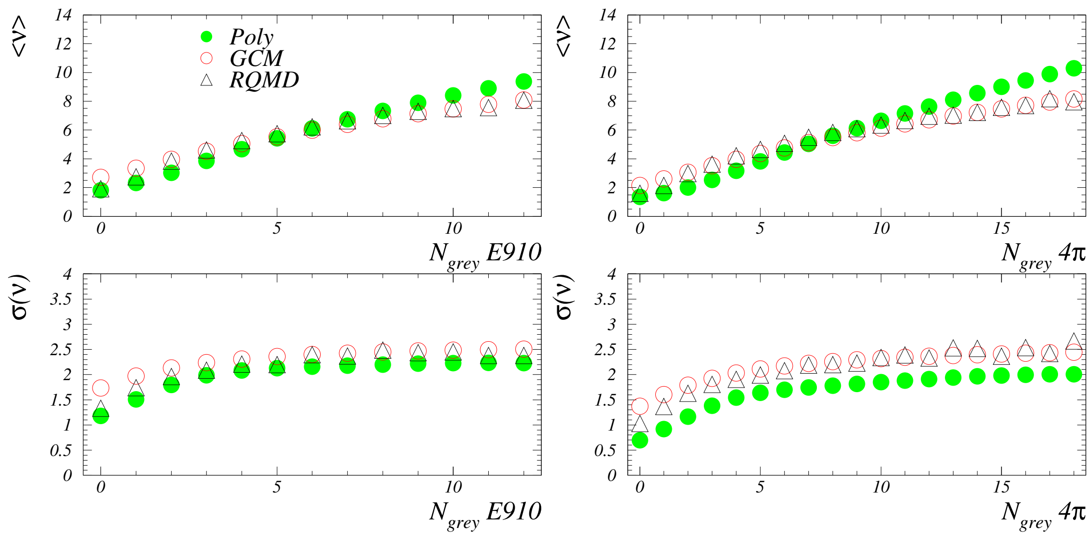

Figure 4.9: RQMD $\nu(N_g)$ for Au nucleus - intrinsic and as calculated by GCM and Polynomial Method.

Chapter 5

Antibaryon Production and Reabsorption

In this chapter, the antiproton yields are presented. The opposing processes contributing to these yields are addressed with the different target sizes and beam momenta available in the E910 data. Particularly important to untangling these processes is the dependence of antiproton yields on the number of projectile collisions, ν. First, results from past experiments will be reviewed.

5.1 Past Antiproton Measurements

Antiprotons were first measured in proton-nucleus collisions at subthreshold energies [9, 10, 11]. The threshold beam momentum is approximately 6.5 GeV/c in the lab frame. At the BNL-AGS, at energies above but near threshold, there are several experiments that measured antiproton production in $A + A$ collisions [43, 44, 45], but more relevant to this thesis are the $p + A$ antiproton measurements. Specifically, E802 [46] found no significant target dependence of antiproton yields at proton beam momentum of 14.6 GeV/c. At CERN energies (250-450 GeV/c), on the other hand, NA44 found the antiproton yields to increase with increasing target size in $p + A$ collisions [47], although by less than 50% from $p + Be$ to $p + Pb$. NA35 also found a weak increase in antiproton yields with increasing target size (less than 50% increase from $p + S$ to $p + Au$) [48]. It is interesting to note that at energies high enough, increased production due to a larger system wins over increased reabsorption. Presently, BNL Experiment 941 is making antiproton measurements comparable to E910. It is also a $p + A$ experiment at AGS energies.

5.2 Antiproton Yields as a Function of Beam Momentum

Antiproton production increases as the beam momentum gets farther above production threshold, and reabsorption is expected to become a less dominant effect as energy increases and the $p\overline{p}$ annihilation cross section decreases (see Fig. 1.1). Although, within the momentum range that we measure antiproton production, we do not expect a significant difference in the reabsorption of the antiprotons, we nevertheless expect the beam momentum dependence to be significant simply because of the increased available energy for production. Antiproton yields (corrected for acceptance and efficiency) are shown in Figs. 5.1 and 5.2 for beam momenta of 12 GeV/c and 18 GeV/c. As expected, there is a strong dependence of yields on the beam energy. Figure 5.1 shows the rapidity density of antiprotons for 10 MeV/c< p_T <800 MeV/c and $p < 3.5$ GeV/c. Overall, the yields are almost 4 times as large for the 18 GeV/c beam momentum than for the 12 GeV/c beam momentum within this $y - p_T$ range. Mid-rapidity is approximately 1.8 for the 18 GeV/c beam momentum and 1.6 for the 12 GeV/c beam momentum. Figure 5.2 shows the event-normalized transverse momentum distributions for $1.0 < y < 2.0$ and $p < 3.5$ GeV/c. Both tend to peak between 200 and 400 MeV/c, although the peak is only statistically significant for the 18 GeV/c data set.

The production of antiprotons in $p + p$ collisions was shown to depend on the available kinetic energy squared [49], $(KE)^2$, where the available kinetic energy is defined as,

$$KE = \sqrt{s} - 4m_p. \tag{5.1}$$

It is interesting to test whether the antiproton multiplicities in $p + Au$ can be described in the same manner. Assuming that antiproton production occurs in the first proton-nucleon collision, the available kinetic energy can be calculated for each beam momentum, 12.3 and 17.5 GeV/c. The produced and detected

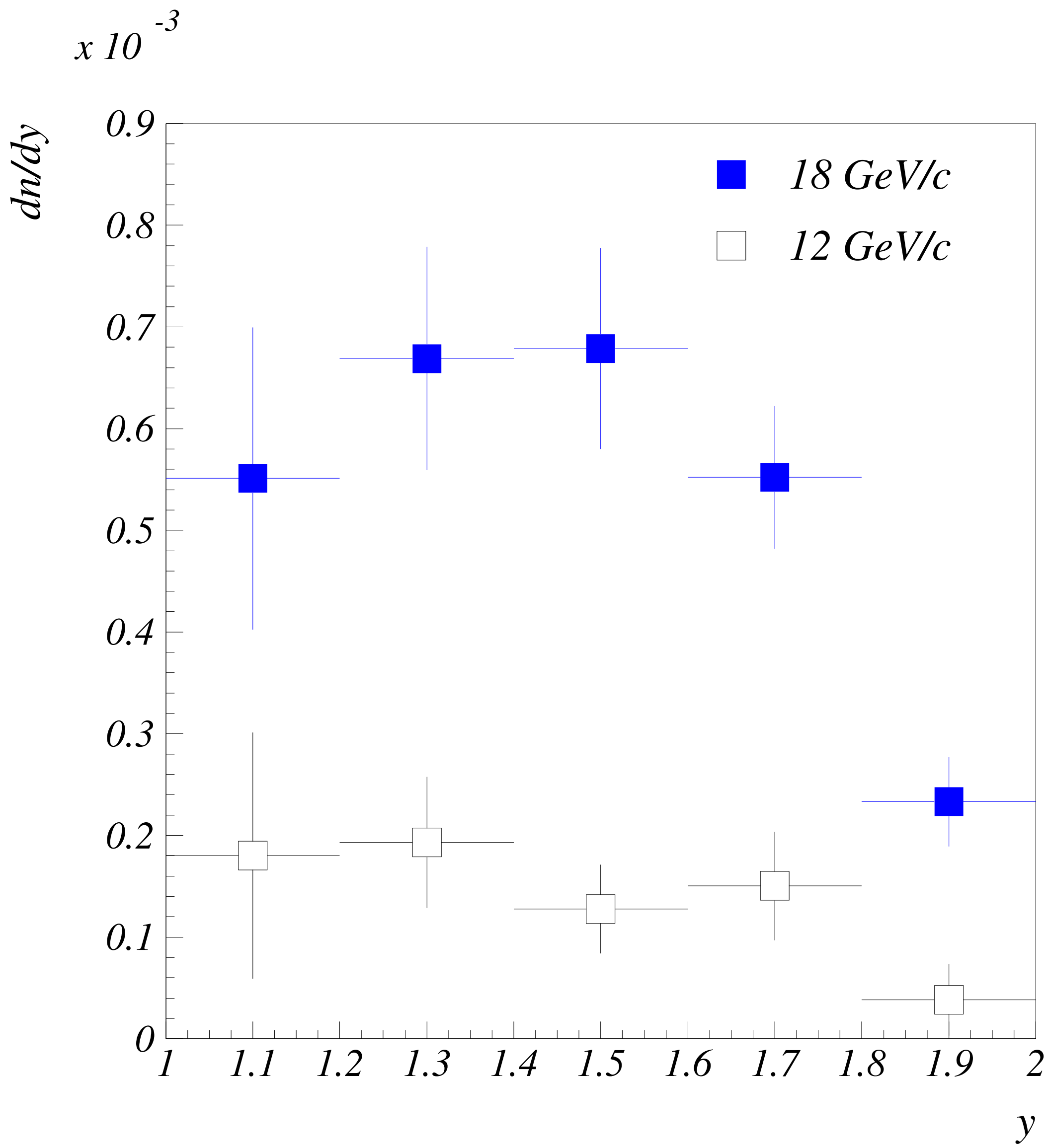

Figure 5.1: Beam energy dependence of antiproton rapidity density in $p + Au$ data for $10\ MeV/c < p_T < 800\ MeV/c$.

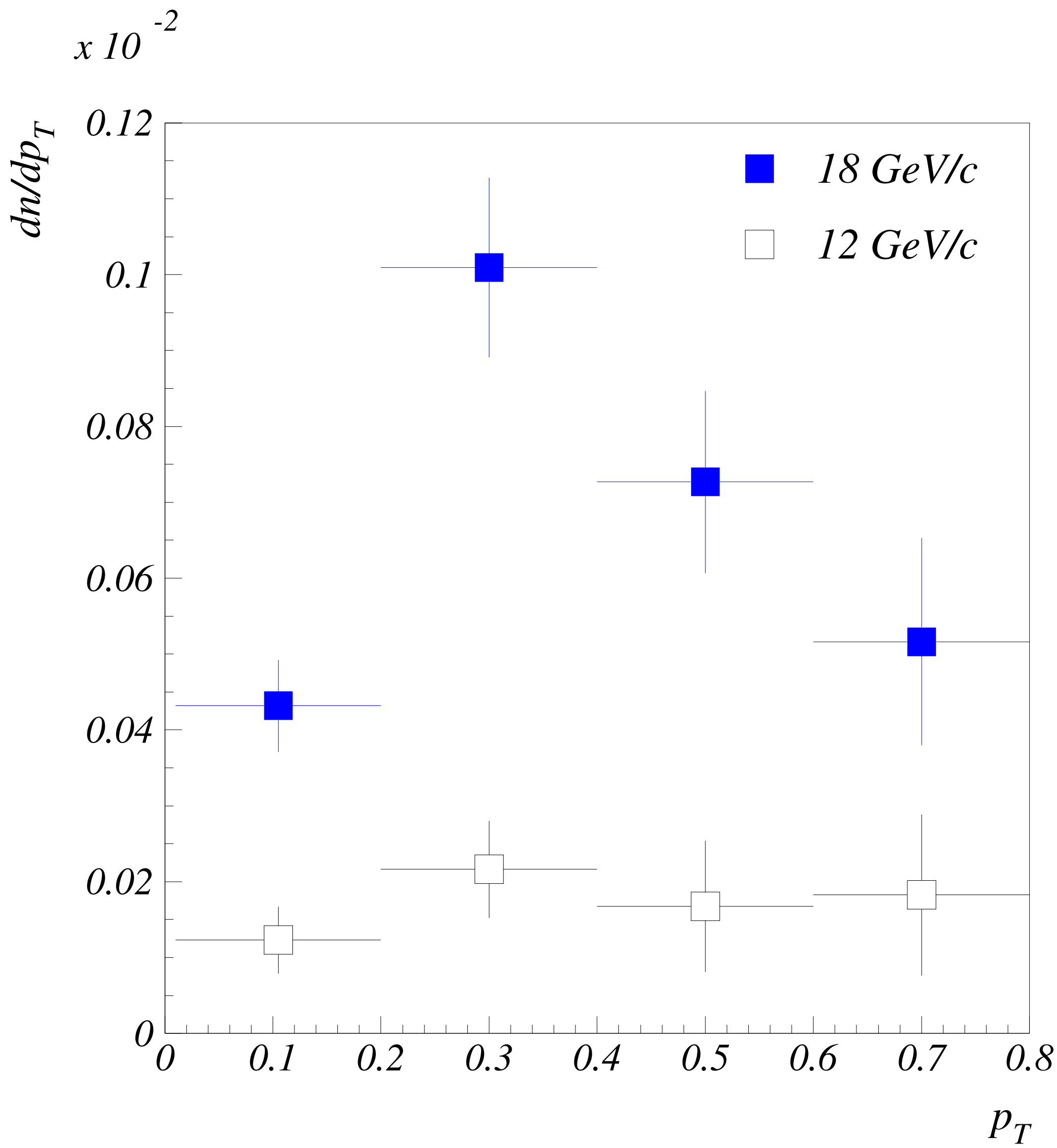

Figure 5.2: Beam energy dependence of event-normalized antiproton tranverse momentum distribution in $p + Au$ data for $1 < y < 2$, $p < 3.5$ GeV/c.

antiprotons have momenta larger than 50 MeV/c and a mean momentum, $< p >$, of 2.55 GeV/c. At these momenta, the annihilation cross section has already fallen somewhat and is not as sensitive to the momentum as at lower momenta (see Fig. 1.1). Thus, it is further assumed that the relative amount of reabsorption is the same at both beam energies. The integrated yields for both beam energies are shown in Fig. 5.3 with a curve proportional to $(KE)^2$. Within errors, the dependence on $(KE)^2$ is able to describe the $p + Au$ data. If either assumption were bad, then the point at $p = 18$ GeV/c would lie above the $(KE)^2$ curve. If the reabsorption were significantly different for the two beam momenta (making our second assumption false), then the 12 GeV/c yield would be more affected by reabsorption and thus lie below a $(KE)^2$ curve passing through the 18 GeV/c point. If, however, the first assumption were false, that the production were not dominated by first collision production, then the 18 GeV/c yield would lie above a $(KE)^2$ curve passing through the 12 GeV/c point. Within this statement is also included the assumption that production in the first $p + N$ collision is at least as great as the free $p + p$ cross section, which is currently believed to be true in the theoretical community [61]. With this last assumption, the $(KE)^2$ dependence of our $p + Au$ antiproton yields does not allow for much additional production in second collisions. This supports dominant antiproton production occuring in the first $p + N$ collision.

Figure 5.4 shows the transverse momentum density distributions again for

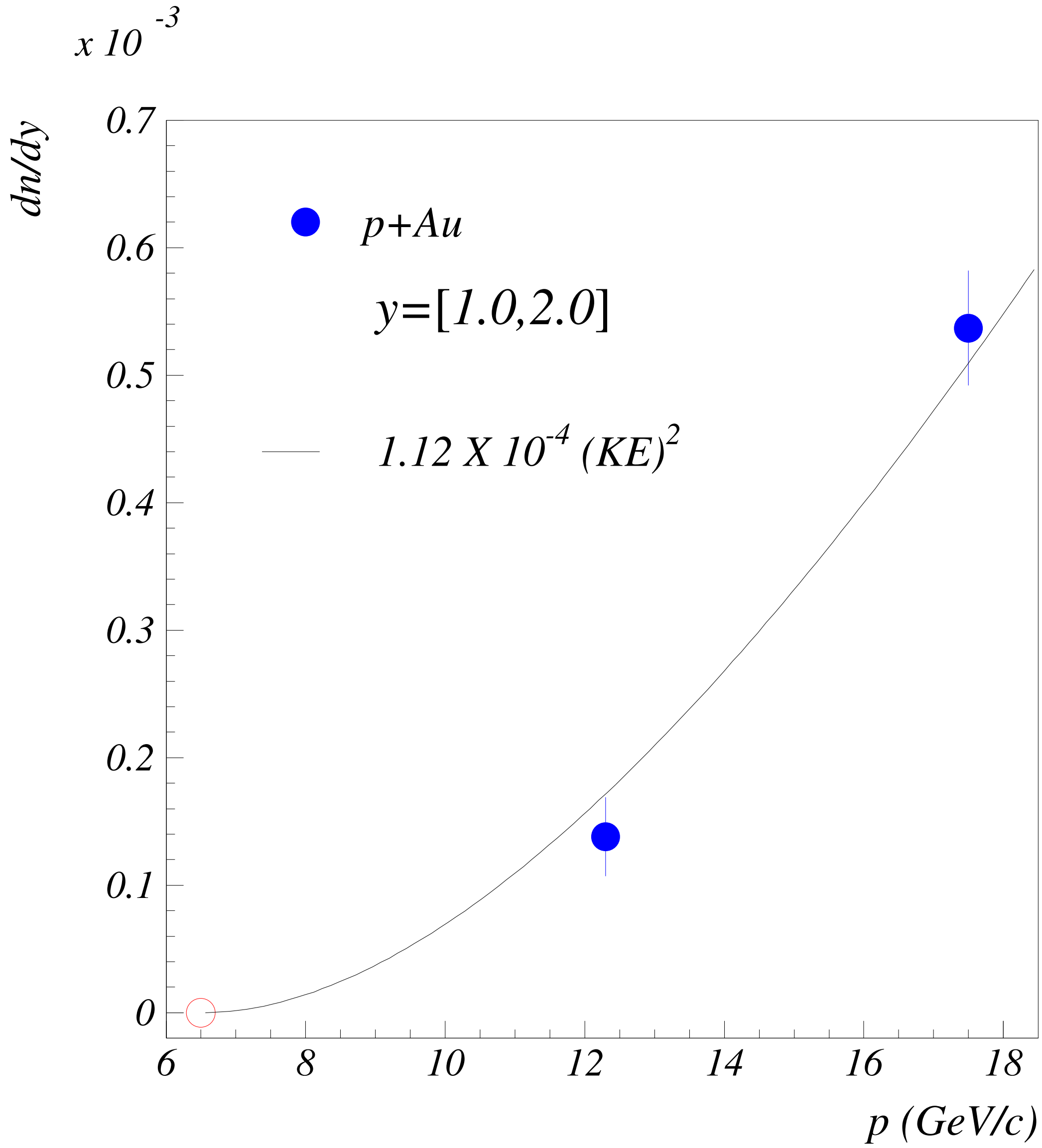

Figure 5.3: Integrated antiproton dn/dy for $p + Au$ as a function of beam momenta. The curve is proportional to the available kinetic energy squared. The open circle at $p = 6.5\ GeV/c$ is the $\overline{p}$ production threshold.

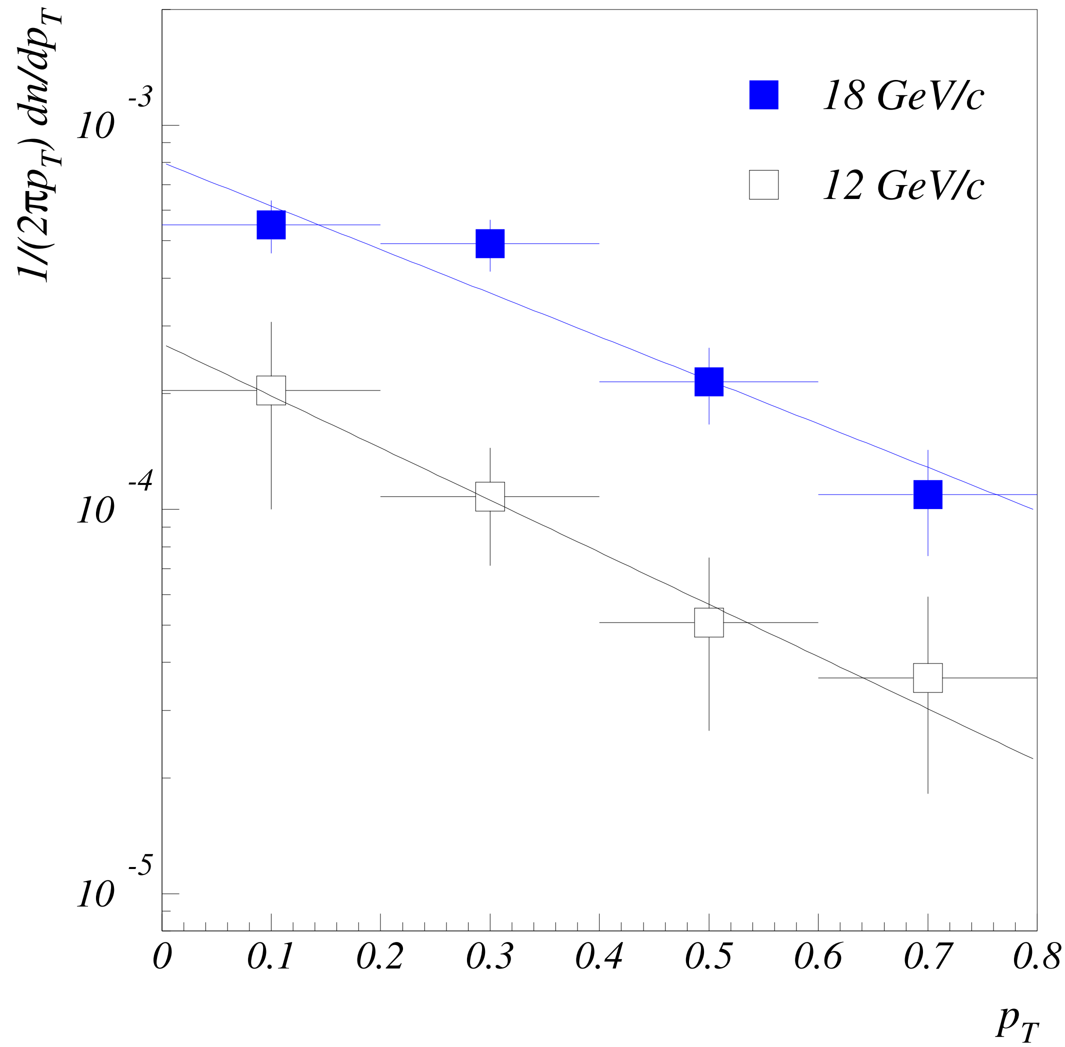

Figure 5.4: Beam energy dependence of tranverse momentum density in $p + Au$ data for $1 < y < 2$, $p < 3.5\ GeV/c$.

both beam energies fit to an exponential function. The transverse momentum distributions over the rapidity interval $y = [1.0, 2.0]$ are written as exponential functions of p_T,

$$\frac{1}{2\pi p_T}\frac{dn}{dp_T} = C_0 e^{\frac{-p_T}{T}}, \tag{5.2}$$

where C_0 and T are fit parameters. The fit parameters with errors are shown in Table 5.1. Although antiprotons are not expected to be thermally produced, it is interesting to note that the slopes for the different beam momenta on the Au target are similar.

5.3 Antiproton Yields as a Function of Target

Although the likelihood of producing antiprotons may be greater in a larger nucleus, [20, 21] the likelihood of reabsorption is also greater in the presence of more baryons. These two countervailing contributions to the overall yields can be studied by investigating the target dependence of antiproton yields. We show results for Be, Cu, and Au at beam momentum 12 GeV/c in Figs. 5.5 and 5.6 after correcting for acceptance and efficiency.

The transverse momentum densities (or invariant multiplicities over the rapidity interval $y = [1.0, 2.0]$) are shown for all 3 targets in Fig. 5.7. Again, the transverse momentum densities are fit with exponential functions according to Equation 5.2. The fit values are shown in Table 5.1. Although the errors on the

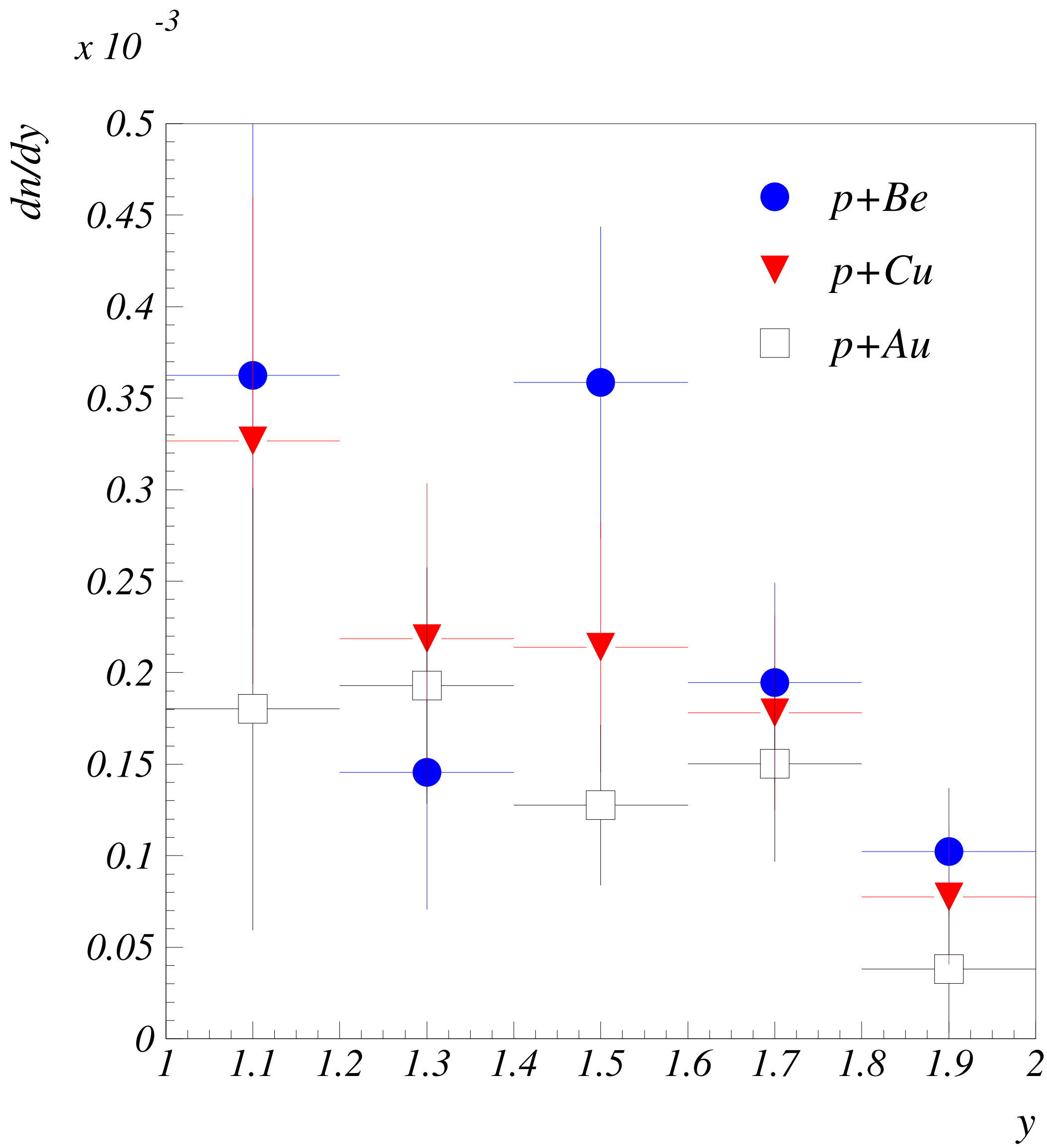

Figure 5.5: Target dependence of antiproton rapidity density in 12 GeV/c $p + A$ data for 10 $MeV/c < p_T < 800$ MeV/c, $p < 3.5$ GeV/c.

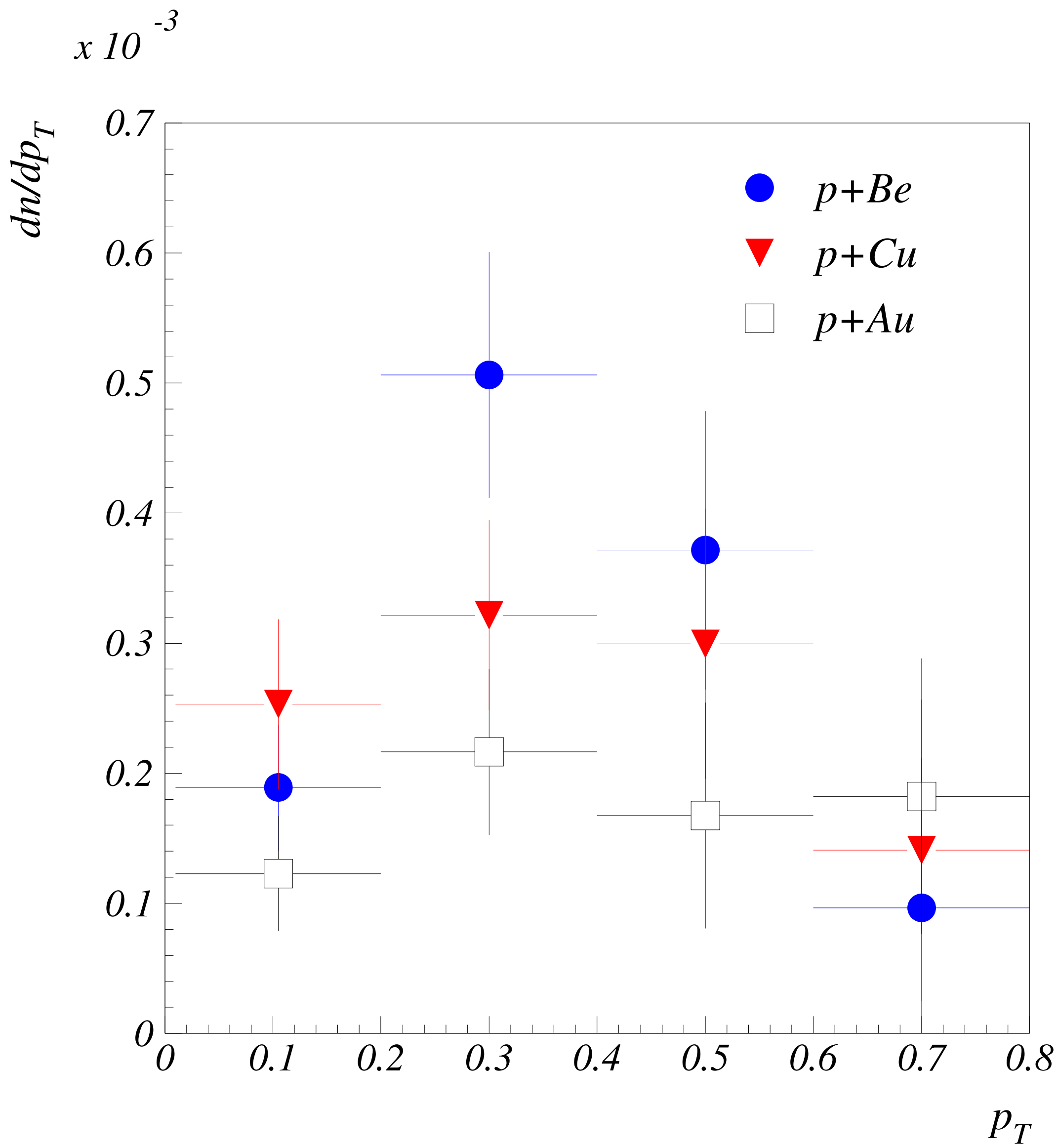

Figure 5.6: Target dependence of event-normalized antiproton tranverse momentum distribution in 12 GeV/c $p+A$ data for $1 < y < 2$, $p < 3.5$ GeV/c.

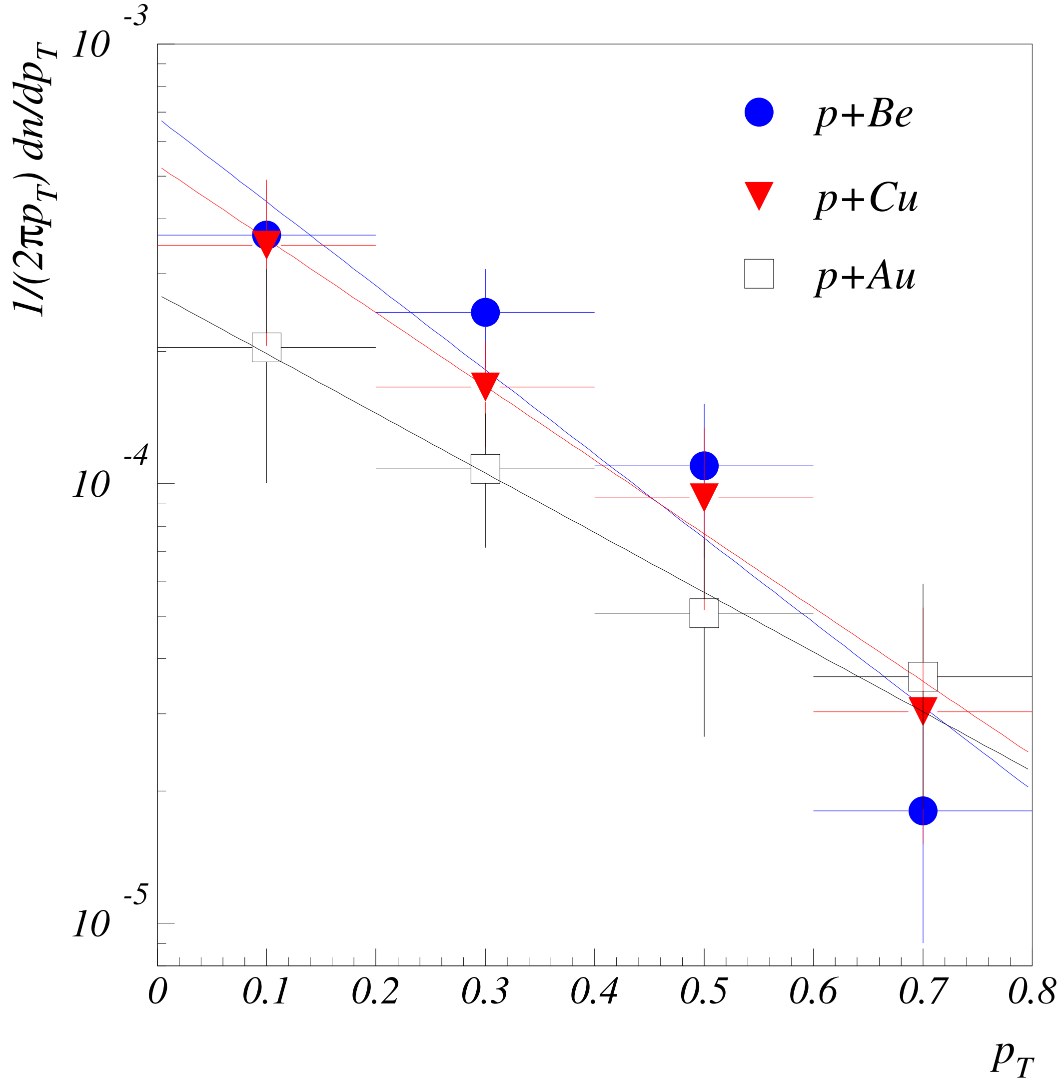

Figure 5.7: Target dependence of tranverse momentum density in 12 GeV/c $p + A$ data for $1 < y < 2$, $p < 3.5$ GeV/c.

Table 5.1: Fit parameters of exponential fits to rapidity densities.

Target	Beam momentum (GeV/c)	C_0 (GeV^{-2}c^2)	T (MeV/c)
Au	18	$8.0 \times 10^{-4} \pm 1.3 \times 10^{-4}$	383 ± 63
Au	12	$2.7 \times 10^{-4} \pm 1.6 \times 10^{-4}$	320 ± 150
Cu	12	$5.3 \times 10^{-4} \pm 2.3 \times 10^{-4}$	259 ± 77
Be	12	$6.8 \times 10^{-4} \pm 1.9 \times 10^{-4}$	227 ± 40

fit parameters are large, it is noteworthy that the rapidity distributions for the different targets have different shapes with different inverse slopes. The increasing inverse slopes, T, indicate the increasing amount of reabsorption as the target size increases.

The integrated rapidity densities are shown in Fig. 5.8. This figure shows that within our $y-p_T$ range, the target dependence of the overall yields is statistically significant, particularly between the Be target and the Au target. Table 5.2 shows the integrated yields over rapidity interval, $y = [1.0, 2.0]$ for each target and beam momentum. The yields over our $y - p_T$ coverage decrease by approximately 40% from the Be target to the Au target for beam momentum of 12 GeV/c.

5.4 Antibaryon Production as a Function of ν

An additional handle to disentangle the mechanisms of production and reabsorption is provided by the number of grey particles in an event. The acceptance and efficiency-corrected mean antiproton multiplicities as a function of the number of

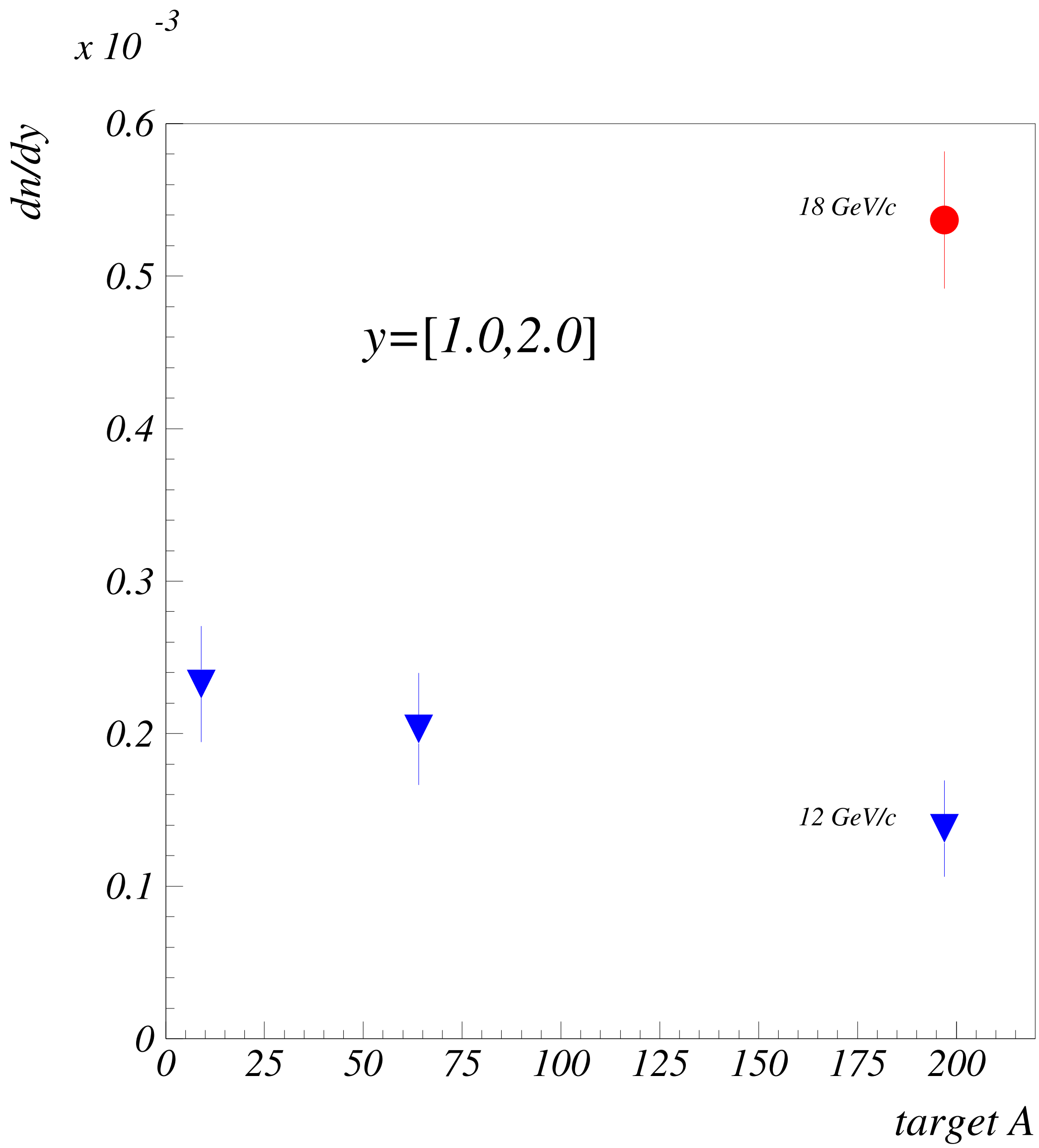

Figure 5.8: Integrated antiproton rapidity density over interval $y = [1.0, 2.0]$ for $10\ MeV/c < p_T < 800\ MeV/c$, $p < 3.5\ GeV/c$.

Table 5.2: Integrated antiproton dn/dy for $y = [1.0, 2.0]$ and 10 $MeV/c < p_T <$ 800 MeV/c.

Target	Beam momentum (GeV/c)	dn/dy over $y = [1.0, 2.0]$
Au	18	$5.37 \times 10^{-4} \pm 0.45 \times 10^{-4}$
Au	12	$1.38 \times 10^{-4} \pm 0.31 \times 10^{-4}$
Cu	12	$2.03 \times 10^{-4} \pm 0.37 \times 10^{-4}$
Be	12	$2.33 \times 10^{-4} \pm 0.38 \times 10^{-4}$

grey particles are shown in Figs. 5.9 and 5.10. Figure 5.9 shows the dependence on beam momentum of this distribution, while Fig. 5.10 shows the distribution for different target sizes at the same beam momentum, 12 GeV/c. Particularly in the 18 GeV/c $p+Au$ data, there seems to be an initial increase in the mean antiproton yield from $N_g = 0$ to $N_g = 1$. This may be a bias due to antiprotons often being produced with a proton. If this proton passes the grey particle cuts, then N_g is at least one. After the initial increase, the yields decrease with increasing N_g.

We calculate the mean number of projectile collisions, ν, in the nucleus for a class of events with a given number of grey particles, and then translate the number of grey particles for this class of events to ν. This analysis is described in detail in Chapter 4, and the values of $\overline{\nu}(N_g)$ for these particular data sets are shown in Appendix B. Figures 5.11 and 5.12 show the mean antiproton multiplicity as a function of the number of projectile collisions ν. Unfortunately, the statistics for the 12 GeV/c data are low in the individual bins of ν. However, a definite trend can be seen in the 18 GeV/c $p+Au$ data in Fig. 5.11, and the 12 GeV/c $p+Au$ data

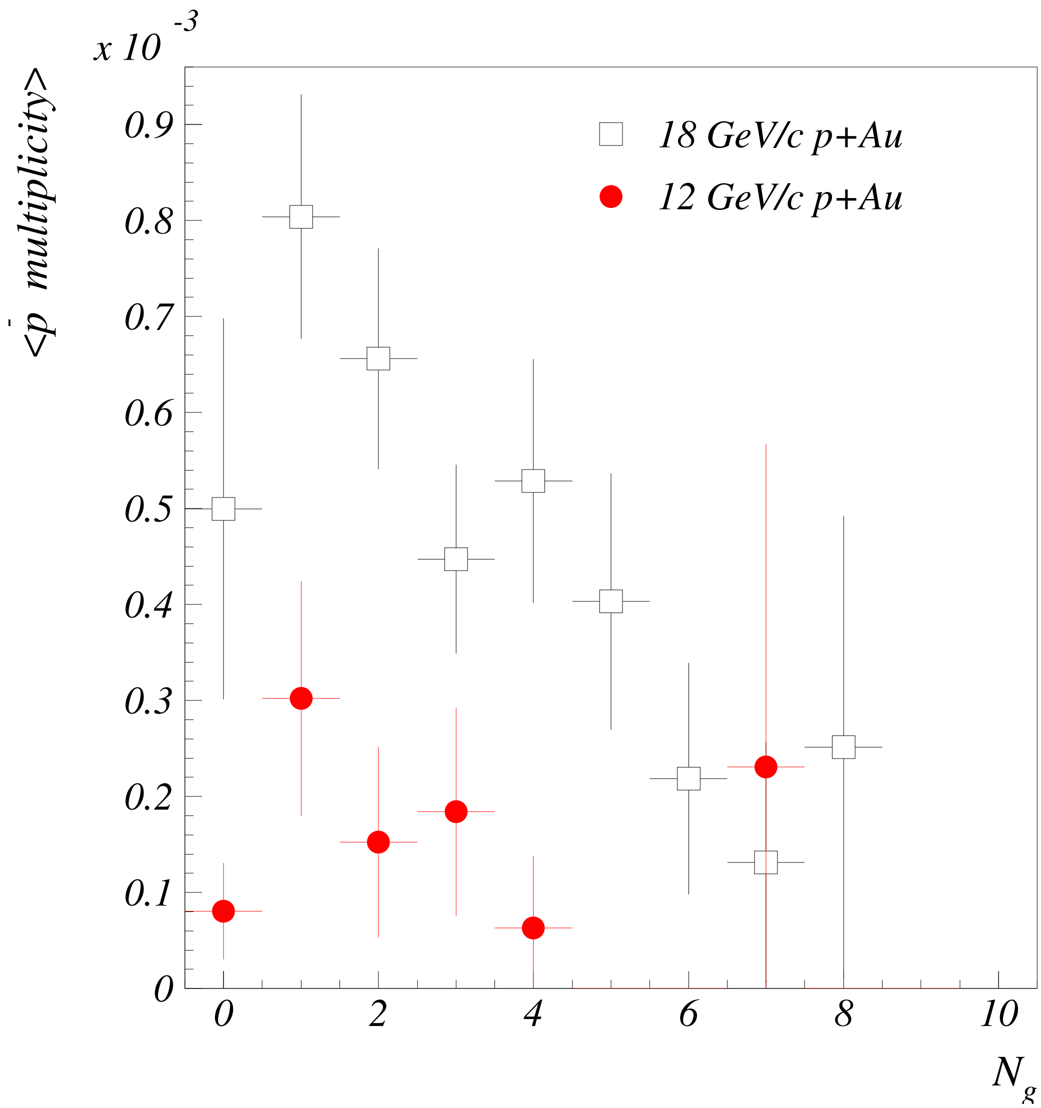

Figure 5.9: Dependence of mean number of $\overline{p}$ per event on N_g for 18 GeV/c and 12 GeV/c $p + Au$ data.

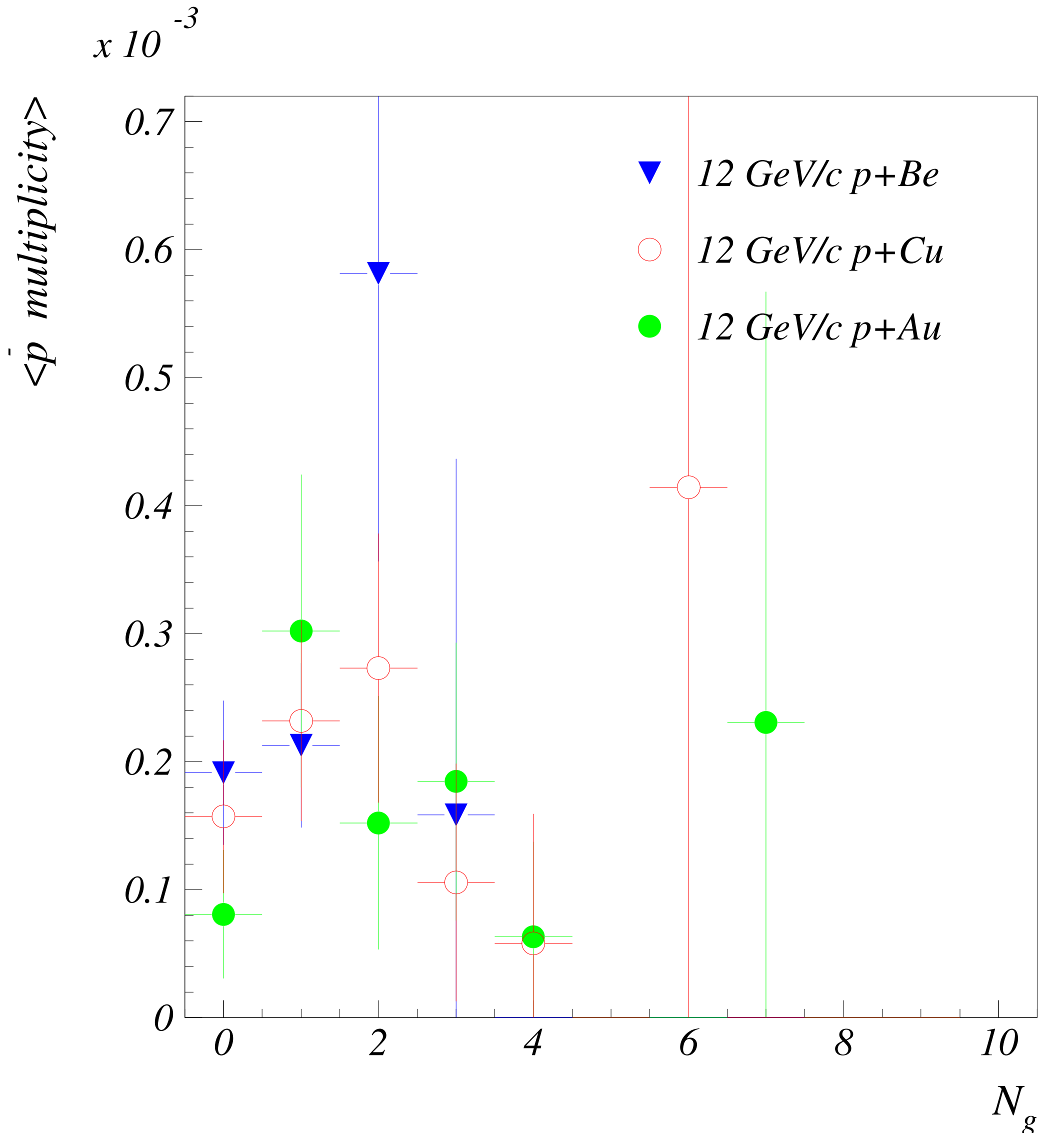

Figure 5.10: Dependence of mean number of $\overline{p}$ per event on N_g for 12 GeV/c $p + Au$, $p + Cu$, and $p + Be$ data.

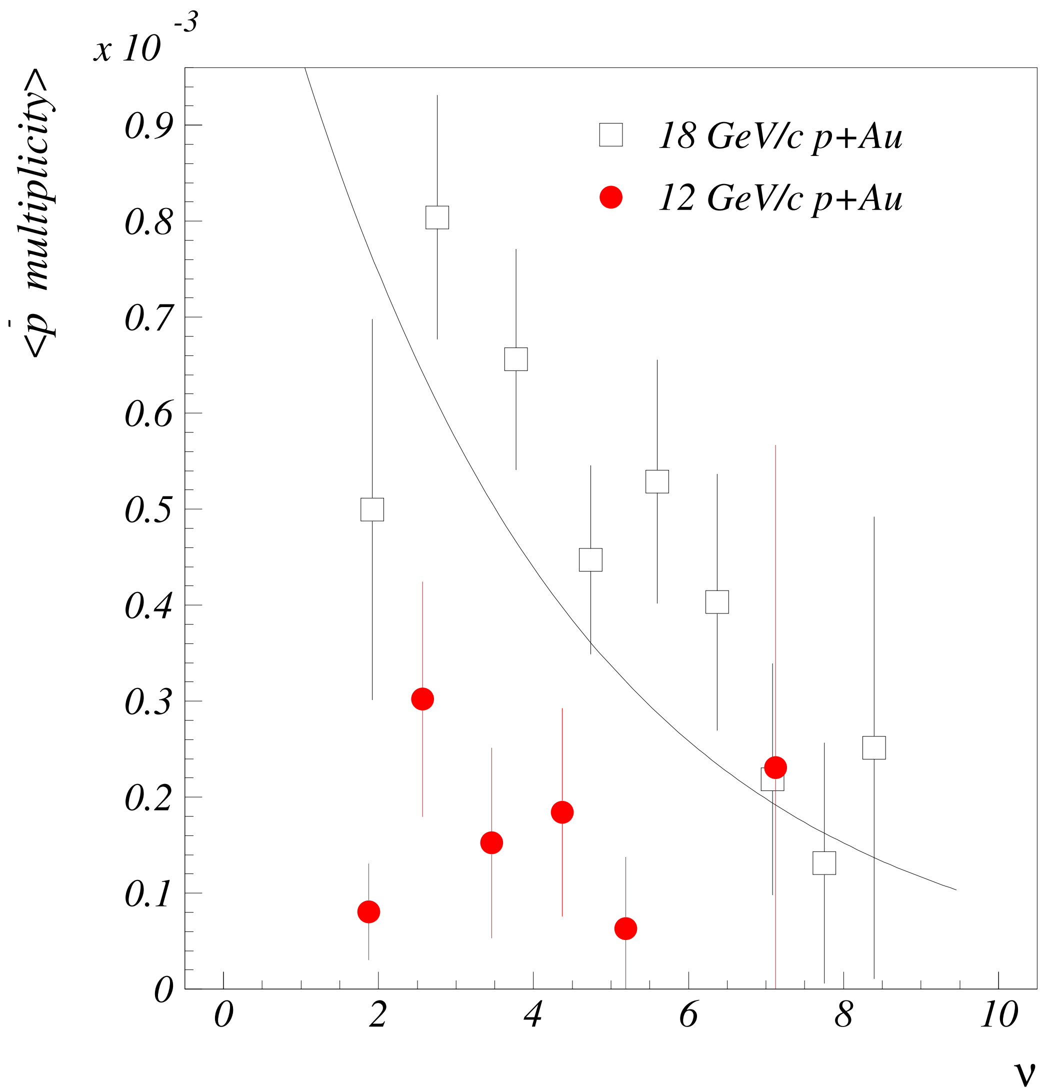

Figure 5.11: Dependence of mean number of $\overline{p}$ per event on ν for 18 GeV/c and 12 GeV/c $p + Au$.

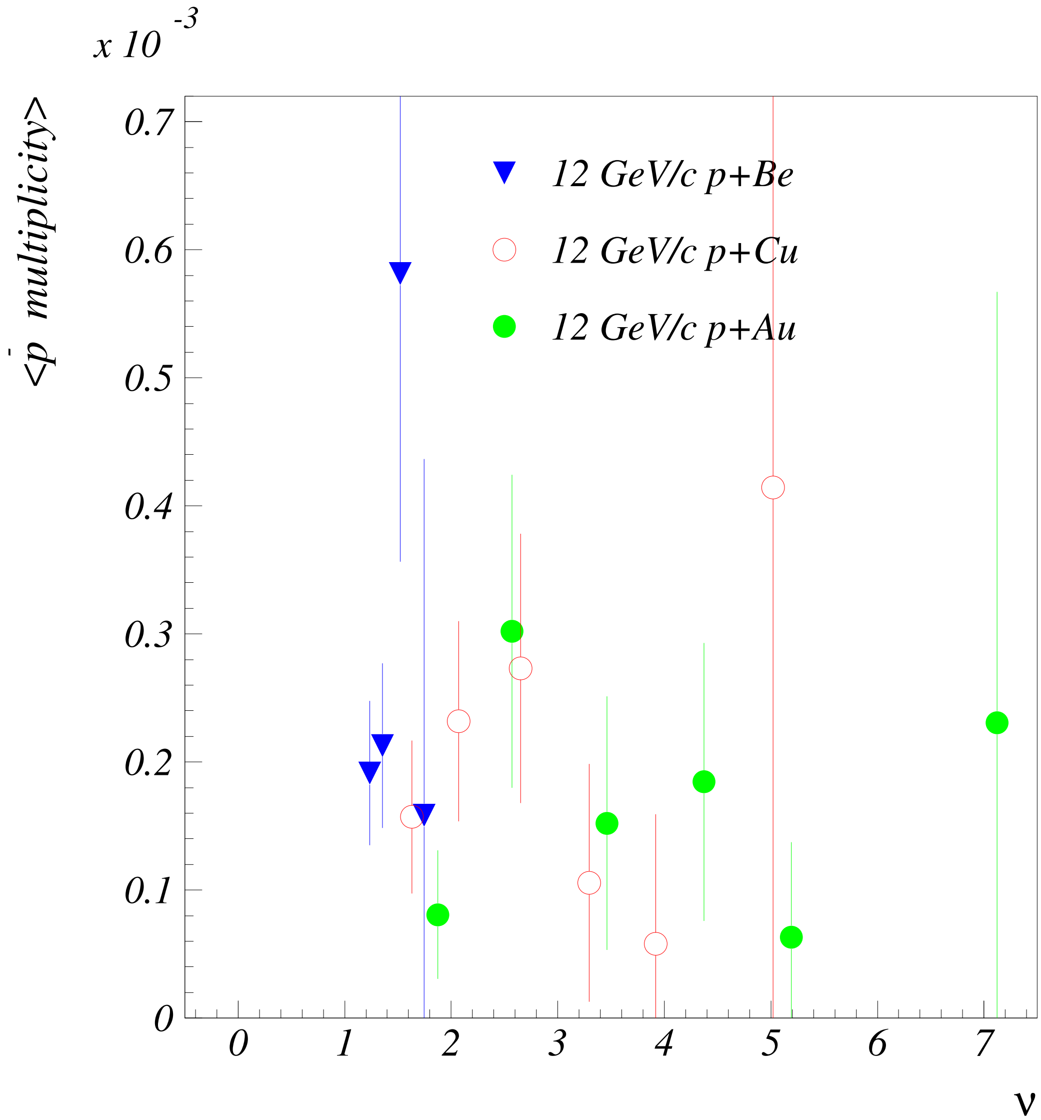

Figure 5.12: Dependence of mean number of $\overline{p}$ per event on ν for 12 GeV/c $p + Au$, $p + Cu$, and $p + Be$ data.

and $p+Cu$ data in Fig 5.12 can accomodate a similar trend. If we assume that the mean antiproton multiplicity depends only on the number of projectile collisions, we can combine the data in bins of ν for different targets. Additionally, we can scale the 18 GeV/c $p+Au$ data down by an overall factor, the ratio of the available kinetic energy squared, $(KE)^2$, for 18 GeV/c beam momentum to the $(KE)^2$ for 12 GeV/c beam momentum, if we assume that the shapes of the distributions for these two beam momenta are the same. With these assumptions, the combined data can reveal a trend in the ν dependence that is more statistically significant. Figure 5.13 shows that the mean antiproton multiplicity decreases as the number of projectile collisions increase. Events with only one projectile collision may represent the more peripheral $p+A$ collisions, thus there is less opportunity for an antiproton to be reabsorbed. Since the antiprotons are very forwardly produced, it is reasonable to assume that the produced antiproton follows the path of the projectile. Furthermore, since ν is a measure of the number of mean free paths that the projectile undergoes and since we have concluded that the dominant production occurs within the first proton-nucleon collision, we can also assume that $\nu - 1$ is a measure of the amount of nuclear material in which the antiproton can be reabsorbed. We can write the surviving antiproton yields as,

$$\begin{aligned} \sigma(p+A \to \overline{p}) &= \sigma(p+p \to \overline{p}) e^{-\sigma_{abs}\rho_0 L} \\ &= \sigma(p+p \to \overline{p}) e^{-(\sigma_{abs}/\sigma_{pN})(\nu-1)}. \end{aligned} \tag{5.3}$$

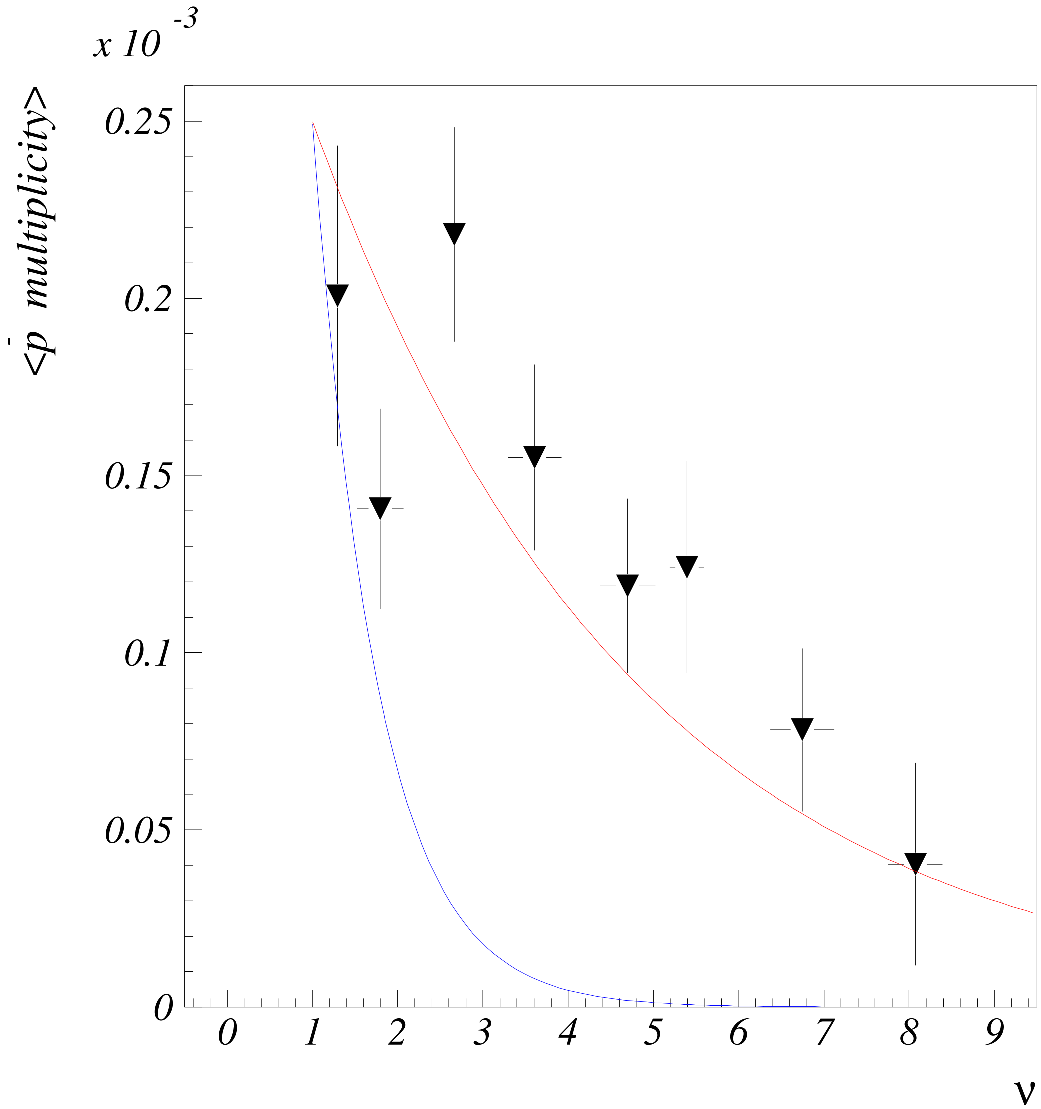

Figure 5.13: Dependence of mean number of $\overline{p}$ per event on ν for all targets combined.

Here, L is the amount of nuclear material the antiproton must traverse, which is equal to $\lambda(\nu - 1)$, where λ is the proton mean free path. The inelastic $p + N$ cross section, σ_{pN}, is equal to $1/(\rho_0\lambda)$, where ρ is the nuclear density. The more steeply falling curve in Fig. 5.13 is Eq. 5.3 with $\sigma_{abs} = \sigma_{anni}$, the $p\overline{p}$ annihilation cross section (for antiproton momentum $p = 2.55$ GeV/c). The curve which can accomodate the data is Eq. 5.3 with $\sigma_{abs} = 0.2\sigma_{anni}$. Without the assumptions neccessary to combine all data sets, this curve (scaled up to $(KE)^2$ for 18 GeV/c beam momentum) is shown to accomodate the 18 GeV/c $p + Au$ data set alone in Fig. 5.11. This seems to indicate that either the free annihilation cross section is altered within the nuclear medium or the amount of nuclear material the antiproton traverses is reduced possibly due to a formation time.

5.5 Comparison With Other Experiments

First we compare our $p + Be$ rapidity density to Allaby's measurement of $p + p$ collisions at 19.2 GeV/c [50]. Since this nucleus is very small and the mean number of projectile collisions from a Glauber calculation is only 1.36, we do not expect much reabsorption. We scale our yields at 12 GeV/c beam momentum to those measured at 19.2 GeV/c according to the available kinetic energy squared (described in Section 5.2). At 12 GeV/c, $(KE)^2 = 1.53$ GeV^2, while at 19 GeV/c, $(KE)^2 = 5.75$ GeV^2, thus we scale our yields up by a factor of 3.76. The rapidity axis of the Allaby data is scaled to our rapidity axis ($y_{beam}(19.2\ GeV/c) \rightarrow y_{beam}(12.3\ GeV/c)$), and the Allaby data is reflected about mid-rapidity. Figure 5.14 shows that our $p + Be$ data agrees reasonably with the Allaby $p + p$ data. Please, note that this supports the assumption made in Section 5.2 that the production cross section in the first $p + N$ collision within the nucleus is comparable to the free $p + p$ production cross section.

We also compare our 12 GeV/c $p + A$ yields with those measured by E802 [46]. The beam momentum for E802 is 14.6 GeV/c. Again, we scale our yields according to the available kinetic energy squared. We also constrain our measurement to a rapidity interval from $y = 1.0$ to $y = 1.6$ to directly compare to the measurement by E802. Figure 5.15 shows the comparison. Our measured antiproton yield for the Be target agrees with E802's measurement. The measurements for the Cu and Au target do not agree very well, and the discrepancy between the E802 measurement and the E910 measurement gets larger from Cu to Au. Since the conclusion regarding target dependence of antiproton yields is different for E910 than for E802, it is important to understand this discrepanacy. A possible explanation is that E802 has overestimated in a region where they have no measurement. The antiproton acceptance for E802 is $1.0 < y < 1.6$ and $300 < p_T < 800$ MeV/c. Because they do not measure in the low p_T region, they assume the p_T distribution is exponential, fit the distribution, and extrapolate to estimate what they do not measure. Because of very low statistics, they combine all of their data sets (Be,

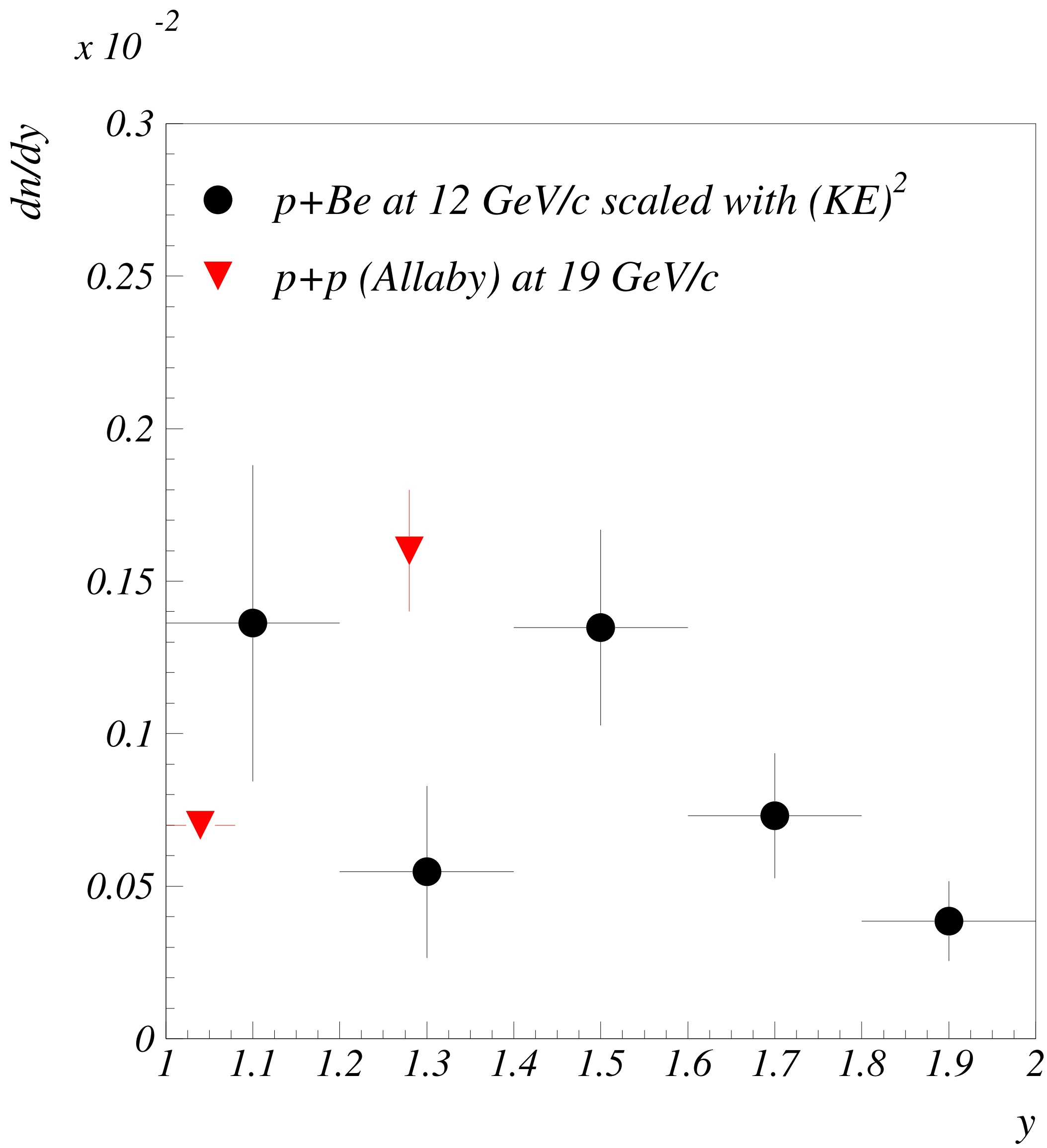

Figure 5.14: Comparison of E910 $p + Be$ rapidity density with Allaby $p + p$ rapidity density (reflected about mid-rapidity).

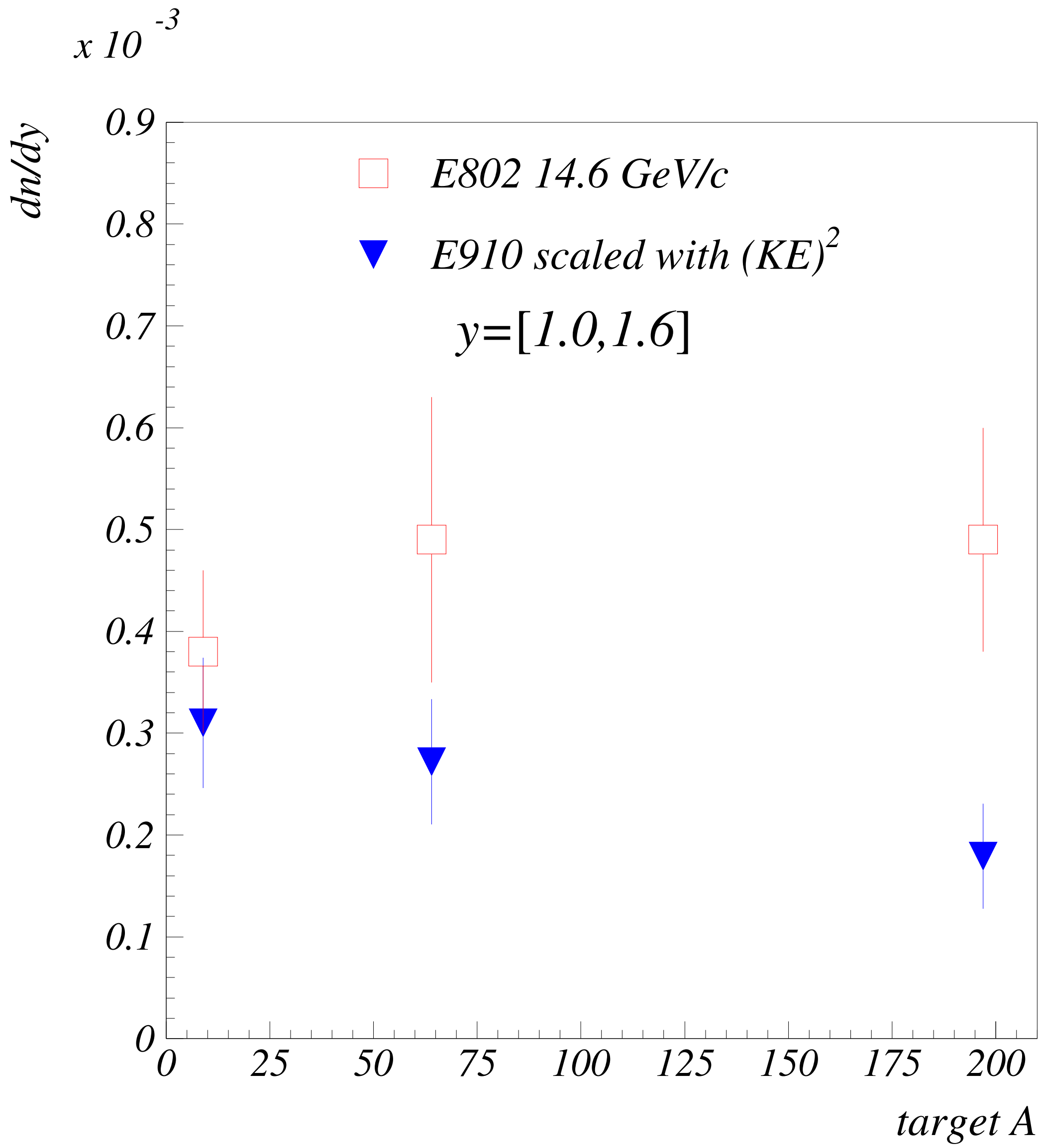

Figure 5.15: Comparison of E910 $p+A$ rapidity density for $y = [1.0, 1.6]$ with E802 [46].

Al, Cu, and Au targets) to determine the inverse slope of the p_T distribution. We have shown that the inverse slope becomes larger as the target size increases, and since the largest data set for E802 is the $p + Al$ data set (a smaller target), it is reasonable to conclude that the yields have been overestimated in the low p_T region for larger targets.

Chapter 6

Theoretical Background

6.1 Theoretical Foundation of Transport Models

Both Relativistic Quantum Molecular Dynamics and Ultra-relativistic Quantum Molecular Dynamics are microscopic transport models that simulate nuclear collisions in the (incident beam) energy range from 200 MeV/nucleon up to 200 GeV/nucleon. They are microscopic because the transport equations are solved for microscopic degrees of freedom, i.e. hadrons. In macroscopic models, the transport equations are solved for macroscopic degrees of freedom, which are energy, momentum, and baryon number decribing the entire system. RQMD and UrQMD are both motivated by transport models of the VUU type [51, 52, 53, 54]. VUU type models are based on the solution of a transport equation for the one-body distribution function $f_1(\vec{q}, \vec{p}, t)$. The function f_1 contains information of all positions and momenta of all hadrons in the system. The following equation,

$$\frac{df_1}{dt} = \left(\frac{df_1}{dt}\right)_{coll}, \tag{6.1}$$

states that the collisions alone cause the distribution function f_1 to change over time. The left-hand side of equation 6.1 can be written as [55],

$$\begin{aligned}\frac{df_1}{dt} &= \frac{\partial f_1}{\partial t} + \dot{q}\frac{\partial f_1}{\partial q} + \dot{p}\frac{\partial f_1}{\partial p} \\ &= \frac{\partial f_1}{\partial t} + \vec{v} \cdot \vec{\nabla}_q f_1 - \vec{\nabla}_q f_1 \cdot \vec{\nabla}_p f_1 = 0,\end{aligned} \tag{6.2}$$

where $\vec{\nabla}_q$ is the gradient in coordinate space, $\vec{\nabla}_p$ is the gradient in momentum space and the force $\dot{p}$ is rewritten as the negative gradient of a potential U. This is the Vlasov equation.

The right-hand side of equation 6.1 can be rewritten as a Boltzmann collision integral with modifications given by Nordheim, $\ddot{U}$hling, and Uhlenbeck [56, 57, 58].

$$\begin{aligned}\left(\frac{df_1}{dt}\right)_{coll} &= -\frac{1}{(2\pi)^6}\int d^3p_2' d^3p_1' d^3p_2 \; \sigma v_{12} \\ &\times [f_1 f_2 (1-f_1')(1-f_2') - f_1' f_2' (1-f_1)(1-f_2)] \\ &\times \delta^3(p_1 + p_2 - p_1' - p_2'),\end{aligned} \tag{6.3}$$

where σ is the reaction cross section for the collision, v_{12} is the relative incoming velocity, p_1 and p_2 are the momenta of the incoming particles and p_1' and p_2' are the momenta of the outgoing particles. The terms such as $(1 - f_1)$ are the Nordheim, Ühling, Uhlenbeck modifications taking care of Fermi statistics (these lead to Pauli blocking), and $\delta^3(p_1 + p_2 - p_1' - p_2')$ is momentum conservation. Setting the left-hand side of equation 6.1, which is given by equation 6.2, equal to the right-hand side of 6.1, given by 6.3, yields the VUU equation. The VUU equation is the time evolution of the distribution function through binary collisions (governed by the cross section σ) and an interaction potential U. The simplest ansatz for the potential U is a Skyrme type potential [59],

$$U = \alpha \frac{\rho}{\rho_0} + \beta \left(\frac{\rho}{\rho_0} \right)^{\gamma}, \tag{6.4}$$

where ρ_0 is the nuclear density and α, β, and γ are parameters used to model the nuclear equation of state. The VUU equation is commonly solved with a test particle method. As mentioned previously, f_1 contains coordinate and momentum information of all hadrons in the system. Each hadron is represented by N point-like test particles which are given by delta functions in coordinate and momentum space,

$$f_1(\vec{q}, \vec{p}) = \frac{1}{N(A_P + A_T)} \sum_{i=1}^{N(A_P+A_T)} \delta(\vec{q_i} - \vec{q})\delta(\vec{p_i} - \vec{p}), \tag{6.5}$$

where A_P and A_T are the mass numbers of the projectile and target respectively. Inserting f_1 into the Vlasov equation (6.2) yields Hamilton's equations of motion for q_i and p_i, which are solved numerically. The density ρ needed for the potential

U in Eq. 6.4 can be obtained from f_1 (Eq. 6.5) by integrating over momentum,

$$\rho(\vec{q}) = \int d\vec{p} f_1. \tag{6.6}$$

To generate initial conditions and to solve the Boltzmann collision integral, Monte Carlo methods are used. Although the VUU equation is the progenitor of most transport models for heavy ion collisions, it is limited by describing the physics accessible by one-body distribution functions only (e.g., production of deuterons, tritons, and larger fragments cannot be described in the VUU approach). RQMD and UrQMD go beyond the VUU model by treating all higher order correlations, using the full N-body distribution function f_N rather than f_1. In addition, the discretized representation of a hadron by N point-like test particles is replaced by a gaussian.

6.2 Implementation and Features of Transport Models

6.2.1 Initialization

The nucleons are initialized randomly in coordinate space within the radius of the nucleus and in momentum space giving them a Fermi momentum.

6.2.2 Propagation

Hadrons are propagated either in curved trajectories, if the real part of the nucleon self-energy is included, or on straight lines, if this potential interaction is neglected. In the calculations shown in this thesis to compare with E910 data, straight line trajectories are used (i.e., the potential interaction is neglected).

6.2.3 Scattering

Two hadrons collide if their distance of closest approach is less than or equal to $\sqrt{\sigma/\pi}$. The cross sections σ are species and energy dependent. The particles may scatter elastically or can be excited into resonance states or strings.

6.2.4 Particle Production

At AGS energies, the dominant mechanism for particle production is through string fragmentations of high mass resonance states or decays of Δ, N^* baryon resonances. In the case of antiproton production, it is always through high mass resonance states.

6.2.5 Antiproton Reabsorption

When a particle is produced in such a string fragmentation, there is a formation time associated with it. The formation time is the time in which the quarks coalesce into hadrons. It is generally around $1-2\ fm/c$ depending on the energy and momentum of the formed hadron in its rest frame. For larger formation times, the produced hadron finds itself farther outside of baryon rich matter. Therefore, the formation time can reduce the reabsorption of antiprotons.

Some of the specifics/differences between the two models are outlined in the following sections.

6.3 RQMD

Inspecting the RQMD history file (only for $p + A$ collisions at AGS energies), antiproton production can be found both in first collisions and in the "multi-step" process (see Section 1.3.1). However, the dominant production is from first collisions. For both cases, the production mechanism is the string fragmentation of high mass baryonic resonances (or excited states of baryons). Denoting high mass baryonic resonances with X^*, Y^*, and Z^* and a doubly excited baryonic state with X^{**}, I will show a few examples. The first two are examples of production in a first collision:

$$p + n \longrightarrow X^* + n,$$
$$X^* \longrightarrow \Delta^{++} + n + \overline{p}.$$

$$p + p \longrightarrow X^* + Y^*,$$

$$Y^* \longrightarrow p + p + \overline{p}.$$

The last is an example of the "multi-step" process.

$$p + n \longrightarrow X^* + Y^*,$$

$$X^* + p \longrightarrow X^{**} + Z^*,$$

$$X^{**} \longrightarrow p + \Delta^+ + \overline{p}.$$

Baryon-antibaryon annihilation occurs through a diquark-antidiquark annihilation. In addition to the formation time that reduces antiproton reabsorption, RQMD has another mechanism that allows one of the proton/antiproton to reinteract before annihilation would occur. This additional mechanism is quasi-nuclear $p - \overline{p}$ state with a lifetime of approximately 1 fm/c [60].

6.4 UrQMD

Antiproton production in UrQMD is similar to that in RQMD. However, UrQMD also has full particle-antiparticle symmetry. For example, if one were to use UrQMD to collide antinuclei $\overline{Au} + \overline{Au}$, the resulting particles would be the same as $Au + Au$ with all antiparticles.

Annihilation occurs through a quark-antiquark annihilation. The remaining quarks can produce other hadrons. This is a slightly different annihilation mechanism than in RQMD (which annihilates diquark-antidiquark). There is also a difference in the definition of the hadron formation time between the two models resulting in a larger formation time in UrQMD (by perhaps 30%) [61]. However, the largest difference is perhaps that UrQMD does not contain the $p-\overline{p}$ molecule that RQMD has.

Chapter 7

Theoretical Comparisons

7.1 Comparisons of Antiproton Yields with RQMD and UrQMD

In this section, we compare our results to those predicted by the Monte Carlo transport models RQMD [23] and UrQMD [24]. In these cascade models, the production of antiprotons occurs through high mass resonance states, efficiently allowing antiproton production at energies otherwise suppressed by phase-space constraints. It is, therefore, of interest to test this hypothesis by comparing data to the predicted yields of these cascade models. Comparisons of data with Monte Carlo can also help give information about the formation time of antiprotons.

7.1.1 Antiproton Distributions in Models (y and p_T)

The following figures compare our yields to those predicted by transport models. Yields from the models have been confined to our $y - p_T$ coverage and have a cut in momentum of 3.5 GeV/c. Figure 7.1 shows reasonable agreement between the rapidity density of the data and both models. RQMD seems to have somewhat larger yields than both the data and UrQMD. The data at mid-rapidity (~1.8) is lower than both model predictions (even though the 3.5 GeV/c momentum cut has been applied to the models as well as the data). Figure 7.2 also shows that the shape in the event-normalized p_T distribution is especially well reproduced by UrQMD. Comparisons between models and data are shown for all targets and energies. Figures 7.3 and 7.4 show comparisons for the 12 GeV/c $p + Au$ data, which show a similar discrepancy between the two models as do the 18 GeV/c comparisons. The data lies between the predictions of RQMD and UrQMD, although closer to the UrQMD prediction. Figures 7.5 and 7.6 show comparisons for the 12 GeV/c $p+Cu$ data to UrQMD only. Again, the agreement is reasonably good. Figures 7.7 and 7.8 (12 GeV/c $p+Be$ data) show that even in the smallest target, there is still a discrepancy in the yields predicted by the two models. This suggests that the differences in the models do not reveal themselves only in the amount reabsorption of antiprotons, but in the amount of production as well.

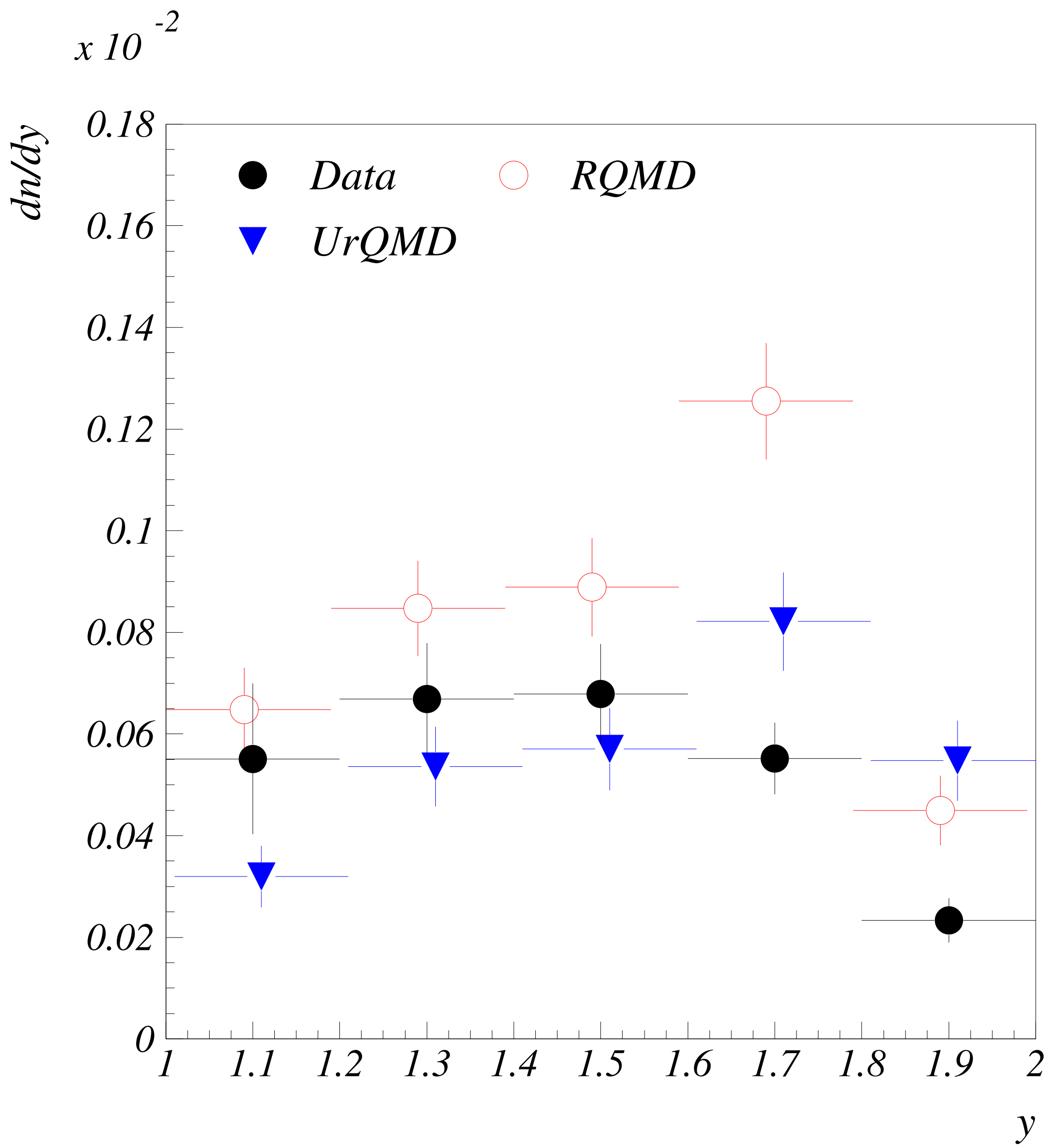

Figure 7.1: Comparison of rapidity density of 18 GeV/c $p + Au$ data to RQMD and UrQMD.

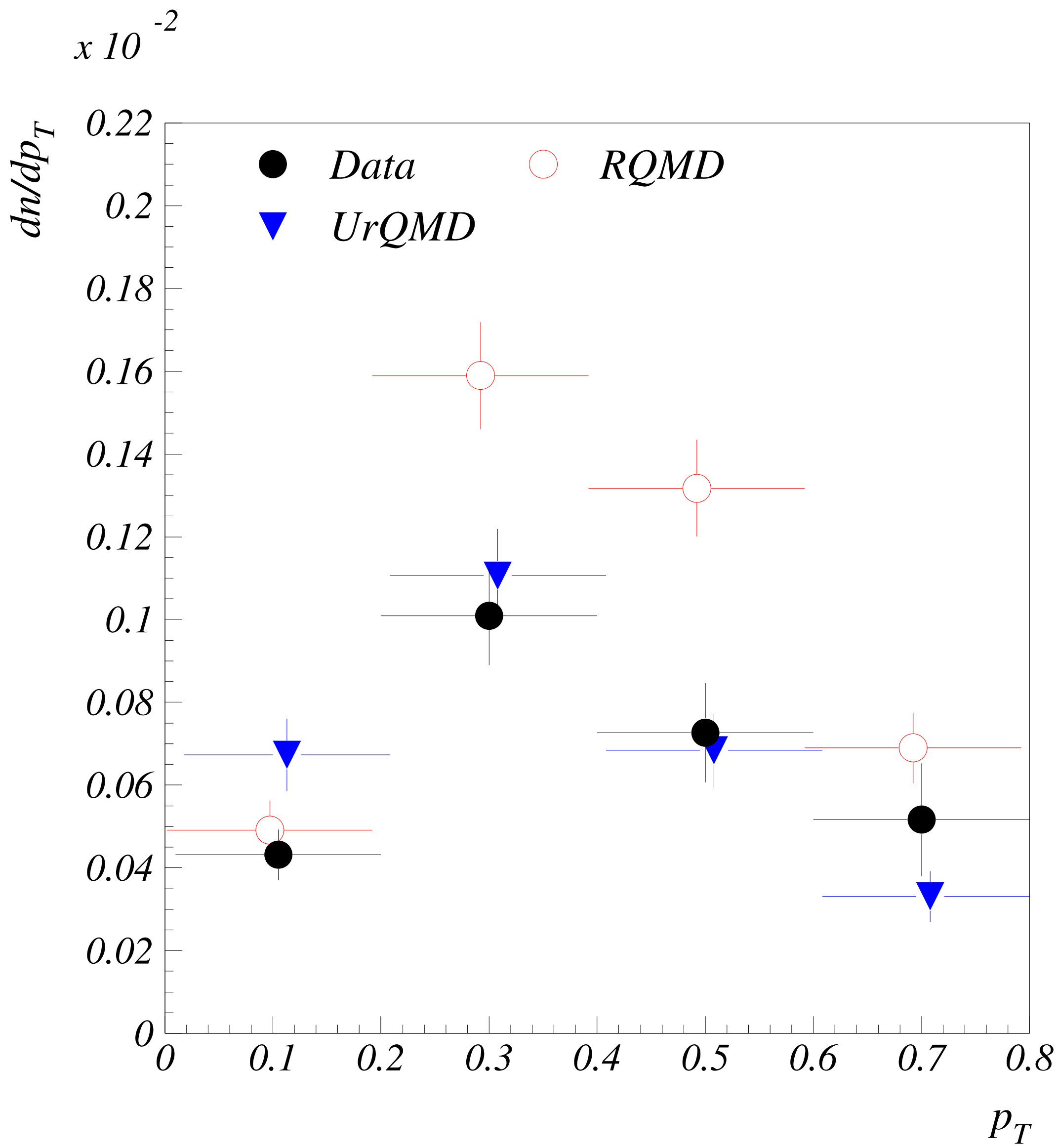

Figure 7.2: Comparison of event-normalized transverse momentum distribution of 18 GeV/c $p + Au$ data to RQMD and UrQMD.

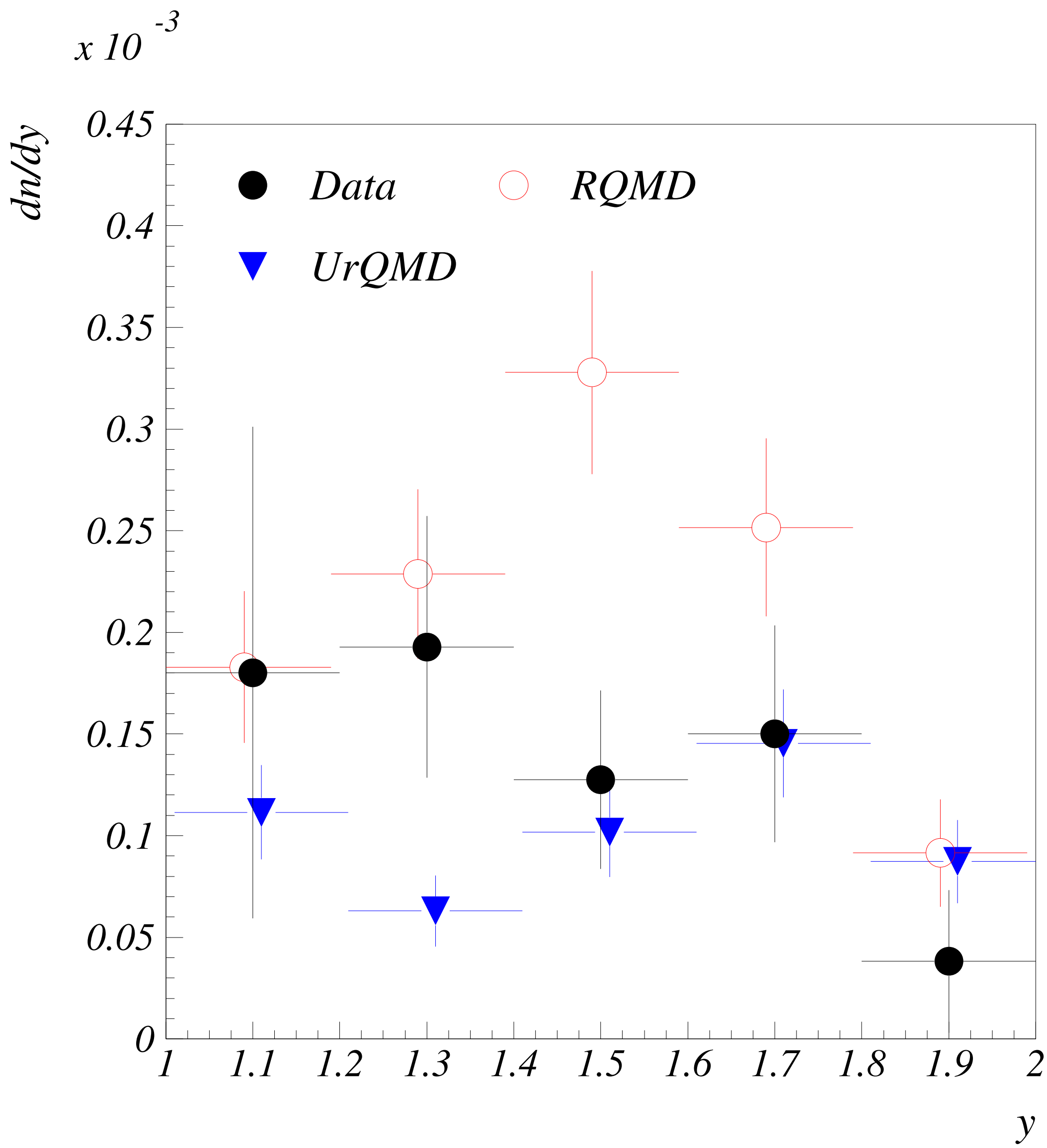

Figure 7.3: Comparison of rapidity density of 12 GeV/c $p + Au$ data to RQMD and UrQMD.

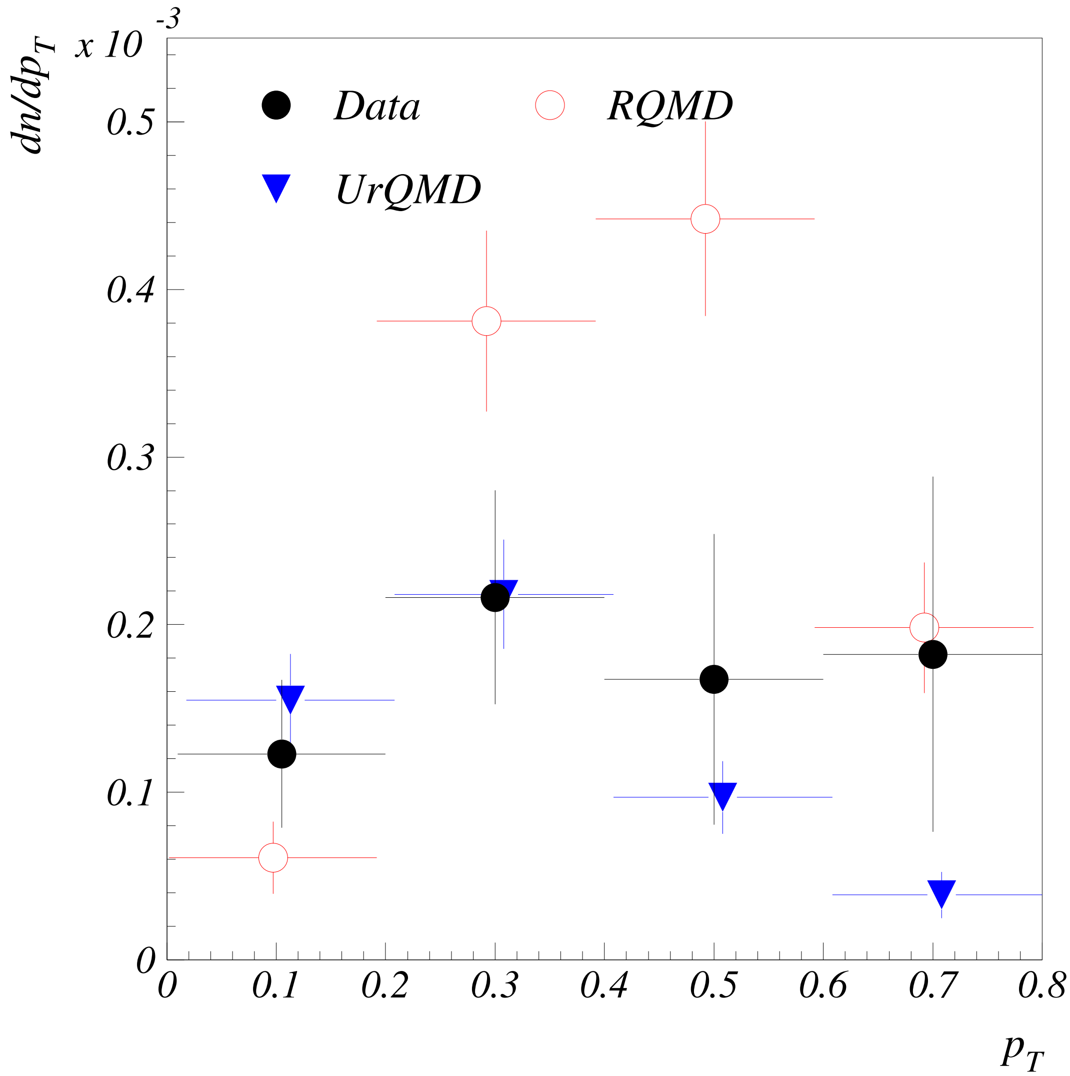

Figure 7.4: Comparison of event-normalized transverse momentum distribution of 12 GeV/c $p + Au$ data to RQMD and UrQMD.

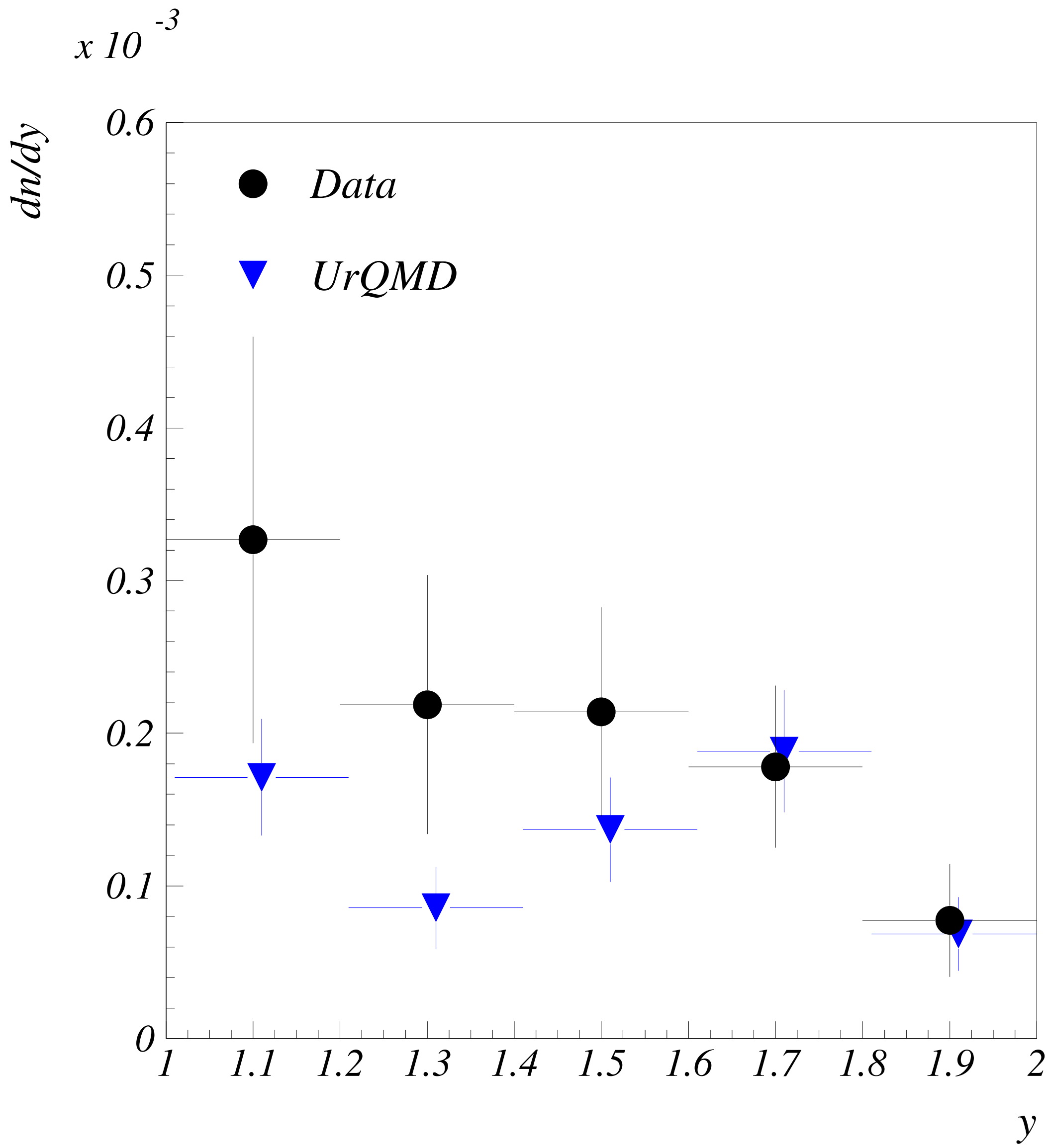

Figure 7.5: Comparison of rapidity density of 12 GeV/c $p + Cu$ data to UrQMD.

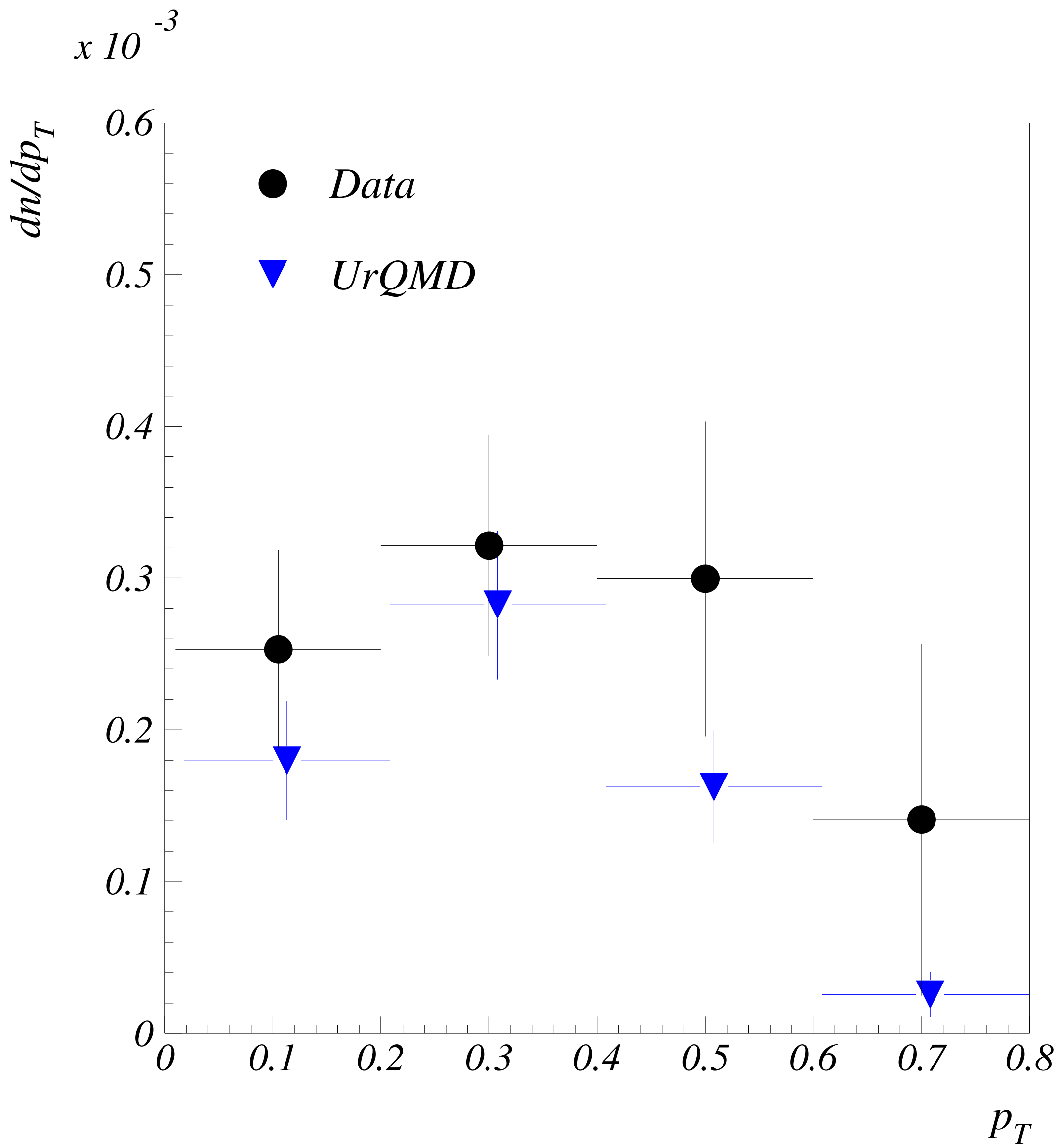

Figure 7.6: Comparison of event-normalized transverse momentum distribution of 12 GeV/c $p + Cu$ data to UrQMD.

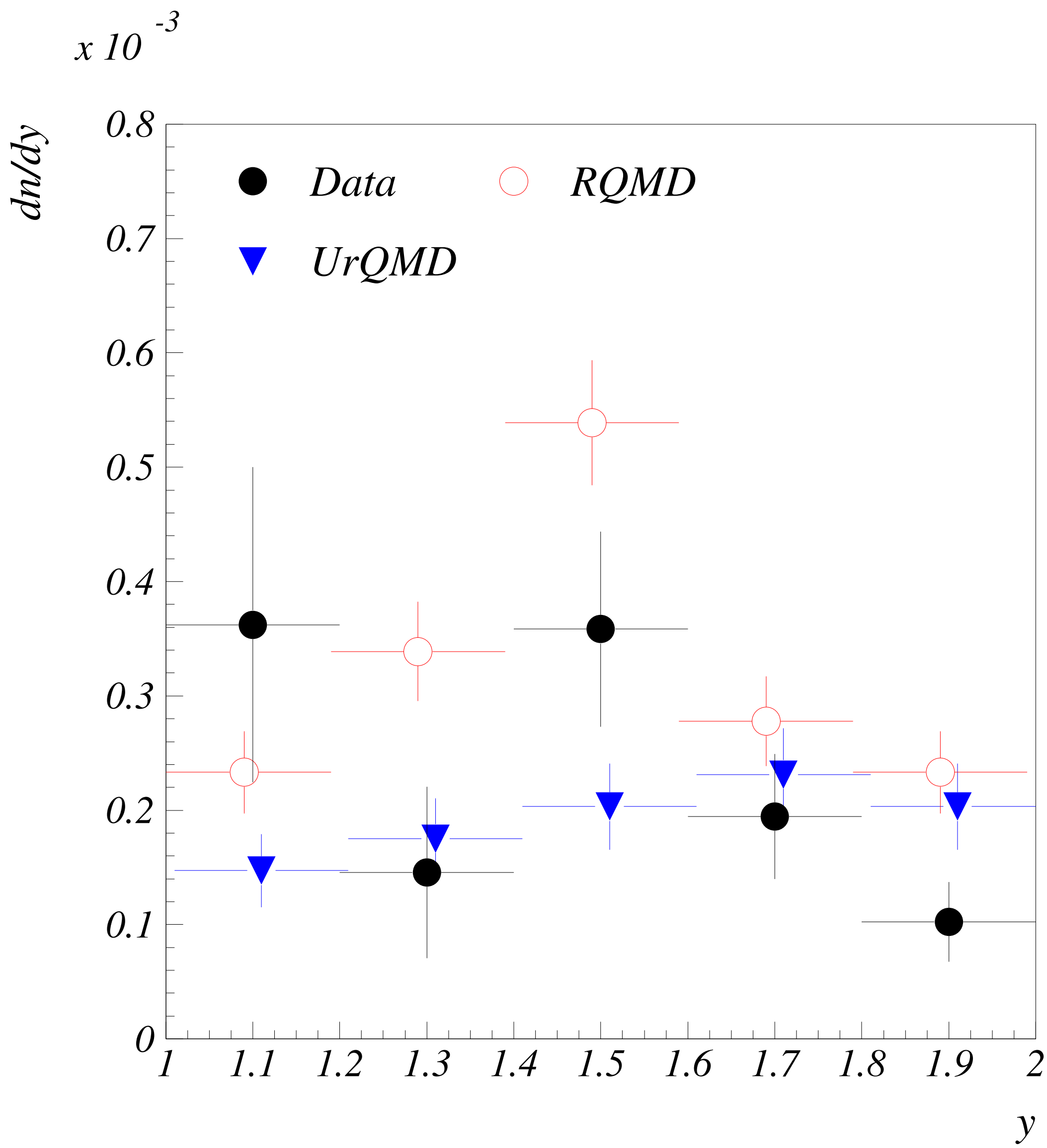

Figure 7.7: Comparison of rapidity density of 12 GeV/c $p + Be$ data to RQMD and UrQMD.

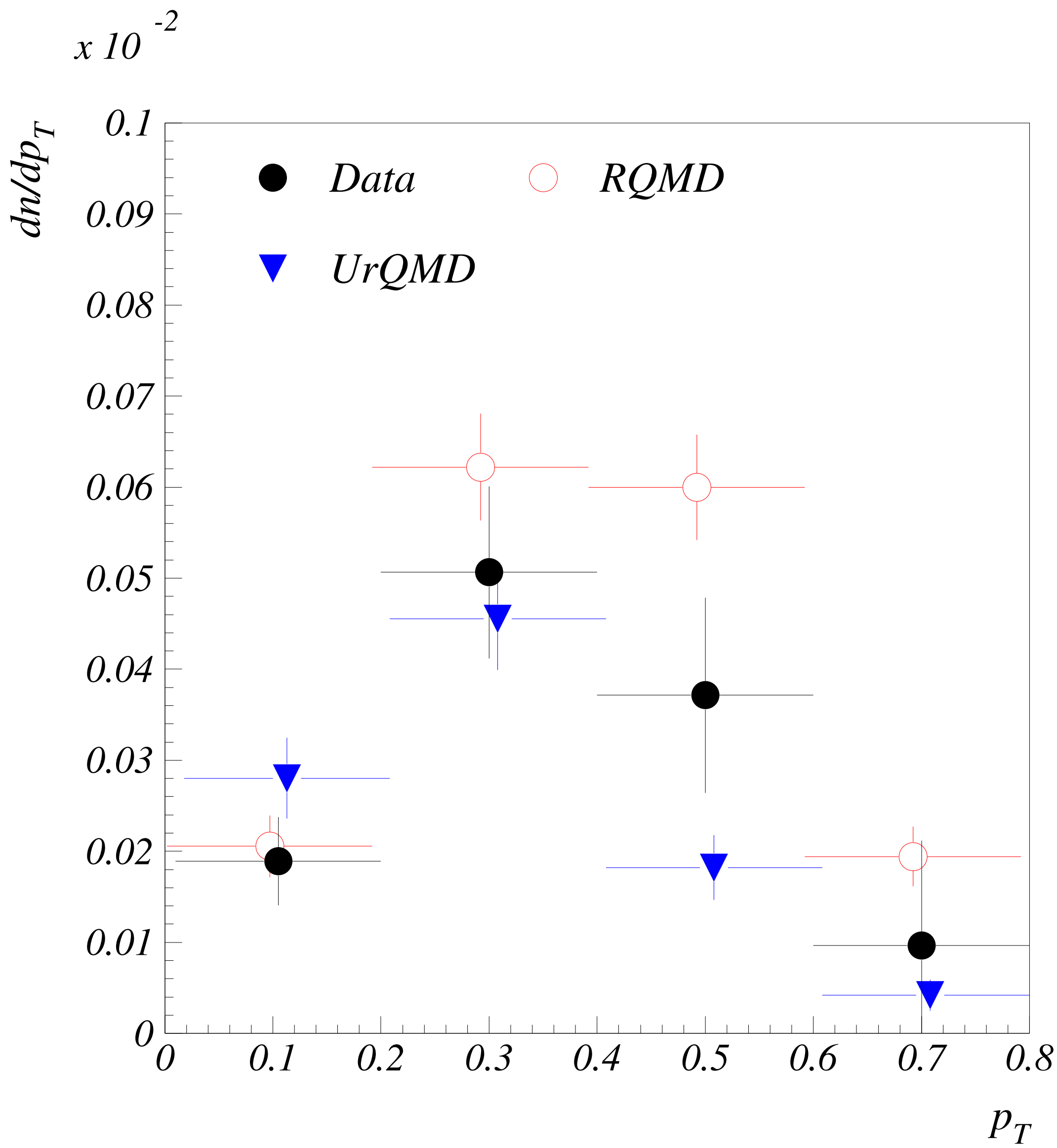

Figure 7.8: Comparison of event-normalized transverse momentum distribution of 12 GeV/c $p + Be$ data to RQMD and UrQMD.

7.1.2 Antiproton Multiplicities as a Function of Centrality

We compare our mean antiproton multiplicities both as a function of N_g and as a function of ν to the model predictions. Figure 7.9 shows good agreement in the mean antiproton yield for any given bin in N_g. Figure 7.10 shows the dependence of the mean antiproton yields on the number of projectile collisions ν. For the data, ν is the extracted $\overline{\nu}$ for a class of events with a given N_g (see Appendix B). For the models, ν is the counted number of projectile collisions (as described in Appendix A). The dependence of the mean antiproton multiplicities on the number of projectile collisions that we see in the data is also well reproduced by the models. The antiproton yields decrease with increasing ν.

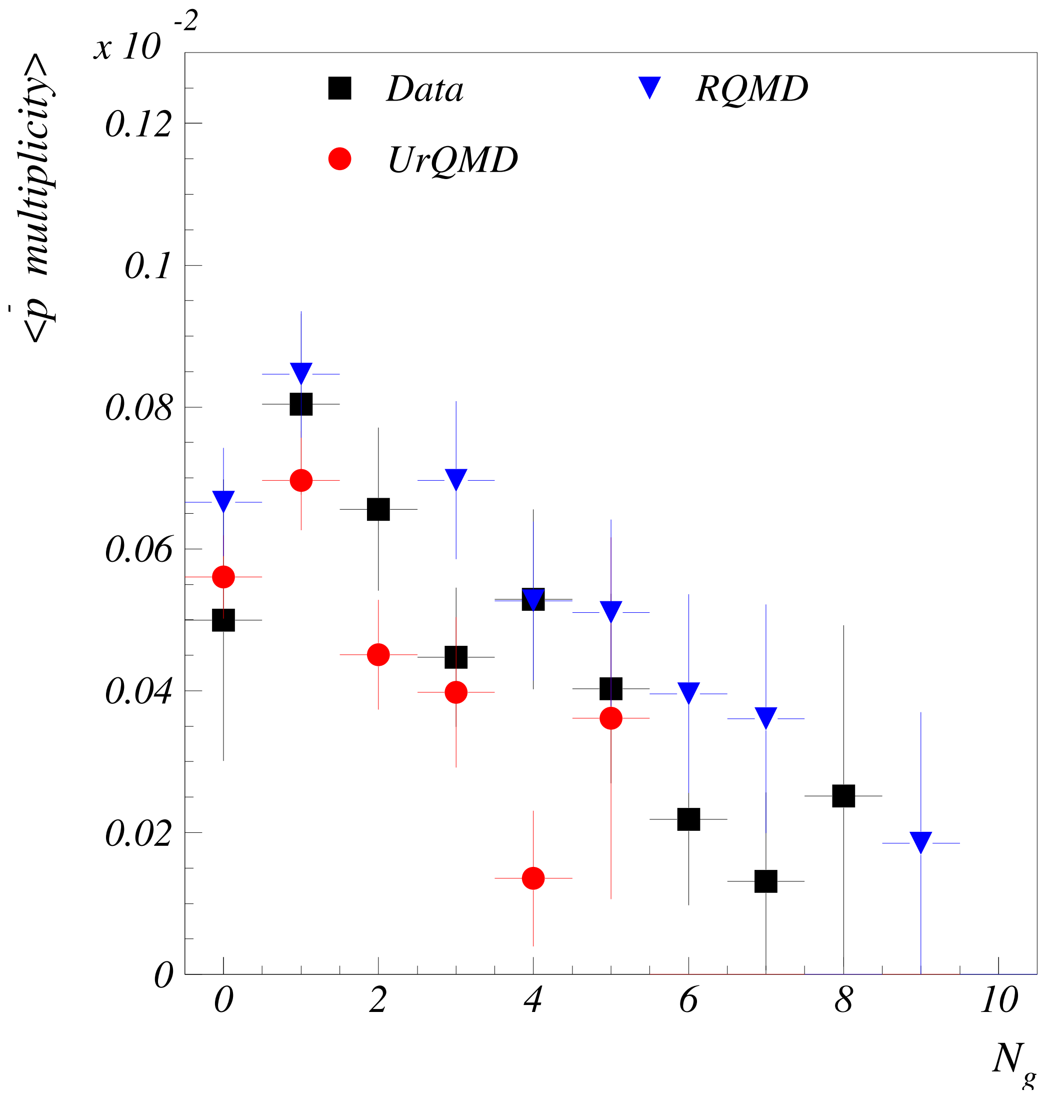

Figure 7.9: Comparison of mean number of antiprotons as a function of N_g in UrQMD and RQMD to 18 GeV/c p+Au data.

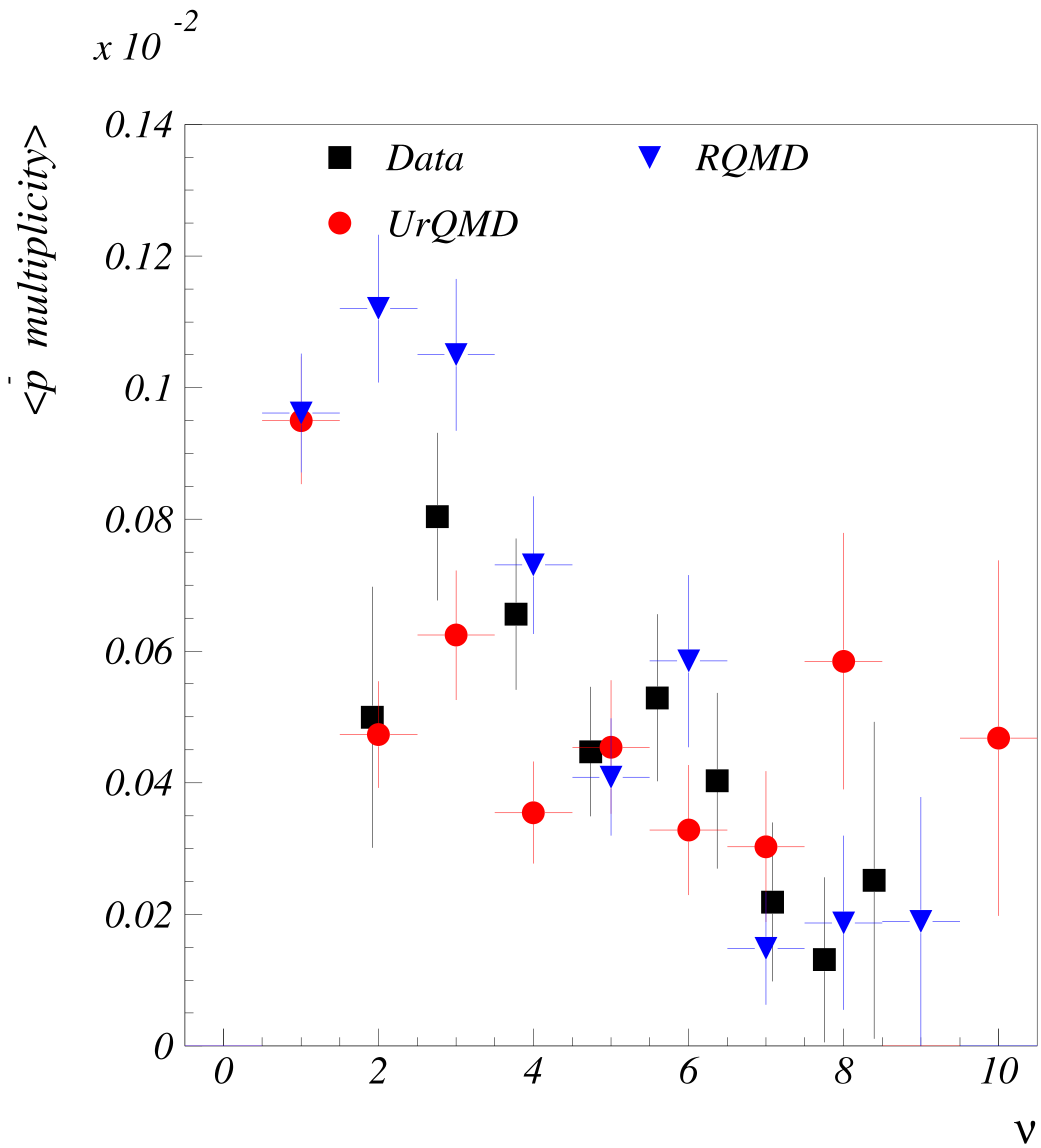

Figure 7.10: Comparison of mean number of antiprotons as a function of ν in UrQMD and RQMD to 18 GeV/c p+Au data.

Chapter 8

Summary and Conclusions

E910 has measured antiproton yields in the phase space region of $10 < p_T <$ 800 MeV/c, $1.0 < y < 2.0$, and $p < 3.5$ GeV/c. Measurements were made for different targets and beam momenta to determine the dependence of antiproton yields on target size and available energy. E910 has also established a relationship to extract the number of projectile collisions based on the measured number of grey particles. Using a new model, we have explored the dependence of $\overline{N_g}$ on the number of projectile collisions ν. We found that the mean number of grey particles can be described by a constant plus a linear dependence on ν; the quadratic dependence on ν was found to be negligible. With this relation, for the first time, mean antiproton multiplicities as a function of the number of projectile collisions have been presented. Based on the analysis presented in this thesis, the following observations and conclusions are made about antiproton production in

$p + A$ collisions.

- The more energy available above production threshold, the greater the yields. Yields for 18 GeV/c $p + Au$ data are almost 4 times as large as for 12 GeV/c $p + Au$ data.

- The beam energy dependence of the $p+Au$ antiproton yields can be described with a function proportional to the available kinetic energy squared, which can also describe $p + p$ antiproton yields.

- Antiprotons seem to be predominantly produced in the first $p + N$ collisions. There is no evidence for significant contribution due to second collisions.

- Yields decrease with increasing target size, specifically a $40 \pm 17\%$ decrease from $p + Be$ to $p + Au$ data is observed. This suggests that reabsorption of antiprotons is significant at these energies and naturally is greater in a larger nucleus.

- The different shapes of the transverse momentum densities for different target sizes indicate the effects of reabsorption. The larger target size has a larger inverse slope. The reabsorption is more significant in the low p_T region.

- Yields decrease with the number of projectile collisions.

- In order to accomodate the dependence of the yields on the number of projectile collisions, the effective absorption cross section within the nucleus must be a fraction of the free $p\overline{p}$ annihilation cross section.

- The transport models (UrQMD and RQMD) which include a formation time for antiprotons effectively reducing the free annihilation cross section can reproduce the data reasonably well.

Bibliography

Bibliography

[1] J. C. Collins and M. Perry. *Phys. Lett.*, 34:1353, 1975.

[2] T. D. Lee and G. C. Wick. *Phys. Rev.*, D9:2291, 1974.

[3] H. Mueller W. Scheid and W. Greiner. *Phys. Rev. Lett.*, 32:741, 1974.

[4] K. Wilson. *Phys. Rev.*, D10:2445, 1974.

[5] M. Creutz. *Quarks, gluons, and lattices.* (Cambridge University Press, Cambridge, 1983).

[6] C. Bernard et al. *Phys. Rev.*, D45:3854, 1992.

[7] R. Glauber. *High Energy Physics and Nuclear Structure*, page 311. edited by A. Gideon (North-Holland Publishing Company, Amsterdam, 1967).

[8] H. Stoecker U. Heinz, P. R. Subramanian and W. Greiner. *J. Phys. G:Nucl. Phys.*, 12:1237, 1986.

[9] O. Chamberlain et al. *Il Nuovo Cimiento*, 3:447, 1956.

[10] T. Elioff et al. *Phys. Rev.*, 128:869, 1962.

[11] D. E. Dorfan et al. *Phys. Rev. Lett.*, 14:995, 1965.

[12] V. Perez-Mendez A. Shor and K. Ganezer. *Nucl. Phys.*, A514:717–733, 1990.

[13] J. B. Carroll et al. *Phys. Rev. Lett.*, 62:1829, 1989.

[14] B.D. Serot and J.D. Walecka. *Advances in Nuclear Physics*, volume 16. edited by J.W. Negele and E. Vogt (Plenum, New York, 1986).

[15] G. E. Brown X. S. Fang, C. M. Ko and V. Koch. *Phys. Rev.*, C47:1678, 1993.

[16] T. Maruyama S. Teis, W. Cassing and U. Mosel. *Phys. Rev.*, C50:388, 1994.

[17] G. Batko et al. *J. Phys. G:Nucl. Phys.*, 20:461–468, 1994.

[18] G. E. Brown V. Koch and C. M. Ko. *Phys. Lett.*, B265:29, 1991.

[19] C. Spieles et al. *Phys. Rev.*, C53:2011, 1996.

[20] W. Greiner A. Jahns, H. Stoecker and H. Sorge. *Phys. Rev. Lett.*, 68:2895, 1992.

[21] P. Koch and C.B. Dover. *Phys. Rev.*, C40:145, 1989.

[22] M. Pluemer S. Gavin, M. Gyulassy and R. Venugopalan. *Phys. Lett.*, B234:175, 1990.

[23] H. Stoecker H. Sorge and W. Greiner. *Ann. Phys.*, 192:266, 1989.

[24] S. A. Bass et al. *Prog. Part. Nucl. Phys.*, 41:225, 1998.

[25] G. Rai et al. *IEEE Trans. Nucl. Sci.*, 37:56, 1990.

[26] J. Hauger et al. *Phys. Rev.*, C57:764, 1998.

[27] K. Nakai et al. *Phys. Lett.*, B121:373, 1983.

[28] N. Porile et al. *Phys. Rev.*, C39:1914, 1989.

[29] Xihong Yang. *Semi-Inclusive Measurements of Strangeness Production in pA Collisions at AGS Energies.* PhD thesis, Columbia University, in progress.

[30] J. Babecki and Nowack. *Acta. Phys. Pol*, B9:401, 1978.

[31] R. Albrecht et al. *Z. Phys.*, C57:37, 1993.

[32] K. Braune et al. *Z. Phys.*, C13:191, 1982.

[33] C. Rees et al. *Z. Phys.*, C17:95, 1983.

[34] C. DeMarzo et al. *Phys. Rev.*, D29:2476, 1984.

[35] J. Bailly et al. *Z. Phys.*, C35:301, 1987.

[36] D.H. Brick et al. *Phys. Rev.*, D39:2484, 1989.

[37] X. Wang and M. Gyulassy. *Phys. Rev.*, D44:3501, 1991.

[38] I. Otterlund B. Andersson and E. Stenlund. *Phys. Lett.*, B73:343, 1978.

[39] E. Brucker et al. *Phys. Rev.*, D32:1605, 1985.

[40] M.K. Hegab and J. Hüfner. *Phys. Lett.*, B105:103, 1981.

[41] M.K. Hegab and J. Hüfner. *Nucl. Phys.*, A384:353, 1982.

[42] I. Chemakin BNL E910 Collab. et al. *Phys. Rev.*, C, 1999.

[43] T.A. Armstrong et. al. (E864 Collab.). *Phys. Rev. Lett.*, 79:3351, 1997.

[44] M. J. Bennett E878 Collab. et al. *Phys. Rev.*, C56:1521, 1997.

[45] J. Barrette E814 Collab. et al. *Phys. Rev. Lett.*, 70:1763, 1993.

[46] T. Abbott et al. *Phys. Lett.*, B271:1351, 1993.

[47] I. G. Bearden NA44 Collab. et al. *Phys. Rev.*, C57:837, 1998.

[48] T. Alber NA35 Collab. et al. *Phys. Lett.*, B 366:56–62, 1996.

[49] Paul Stankus. *Production of Antinuclei and Rare Particles in Si+A Collisions at 14.6 A·GeV/c at the BNL AGS.* PhD thesis, Columbia University, 1993.

[50] J.V. Allaby et al. CERN Report No. 70-12. Unpublished, 1970.

[51] J.J. Molitoris et al. *Phys. Rev. Lett.*, 53:899, 1984.

[52] B.V. Jacak H. Kruse and H. Stöcker. *Phys. Rev.*, C31:1770, 1985.

[53] S.D. Gupta G. Bertsch and H. Kruse. *Phys. Rev.*, C29:673, 1984.

[54] J. Aichelin and G. Bertsch. *Phys. Rev.*, C31:1730, 1985.

[55] A. Vlasov. *Zh. Eksp. Teor. Fiz.*, 8:291, 1938.

[56] L. Nordheim. *Proc. Roy. Soc. London*, A119:689, 1928.

[57] E.A. Ühling and G.E. Uhlenbeck. *Phys. Rev.*, 43:552, 1933.

[58] E.A. Ühling and G.E. Uhlenbeck. *Phys. Rev.*, 44:917, 1934.

[59] T.H.R. Skyrme. *Nucl. Phys.*, 9:615, 1956.

[60] James Lawrence Nagle. *Antiproton Production and Search for Antideuterons and Negatively Charged Strange Quark Matter in Relativistic Heavy Ion Collisions.* PhD thesis, Yale University, 1997.

[61] Steffen A. Bass. Private communication.

[62] Heinz Sorge. Private communication.

Appendices

Appendix A

Determination of ν in RQMD and UrQMD

Since these transport models are not just simple billiard ball models, counting the number of projectile collisions is not straightforward [61, 62]. At AGS energies, the dominant mechanism for particle production is through high mass resonances which decay through string fragmentation. When the projectile undergoes such a string fragmentation, its cross section is divided among the constituent quarks according to the "additive quark model." Therefore, all collisions undergone by particles carrying the constituent quarks of the projectile must be counted. The resulting $\pi(\nu)$ distributions for both RQMD and UrQMD for 18 GeV/c $p + Au$ are shown in Fig. A.1 compared to the distribution obtained from the Glauber

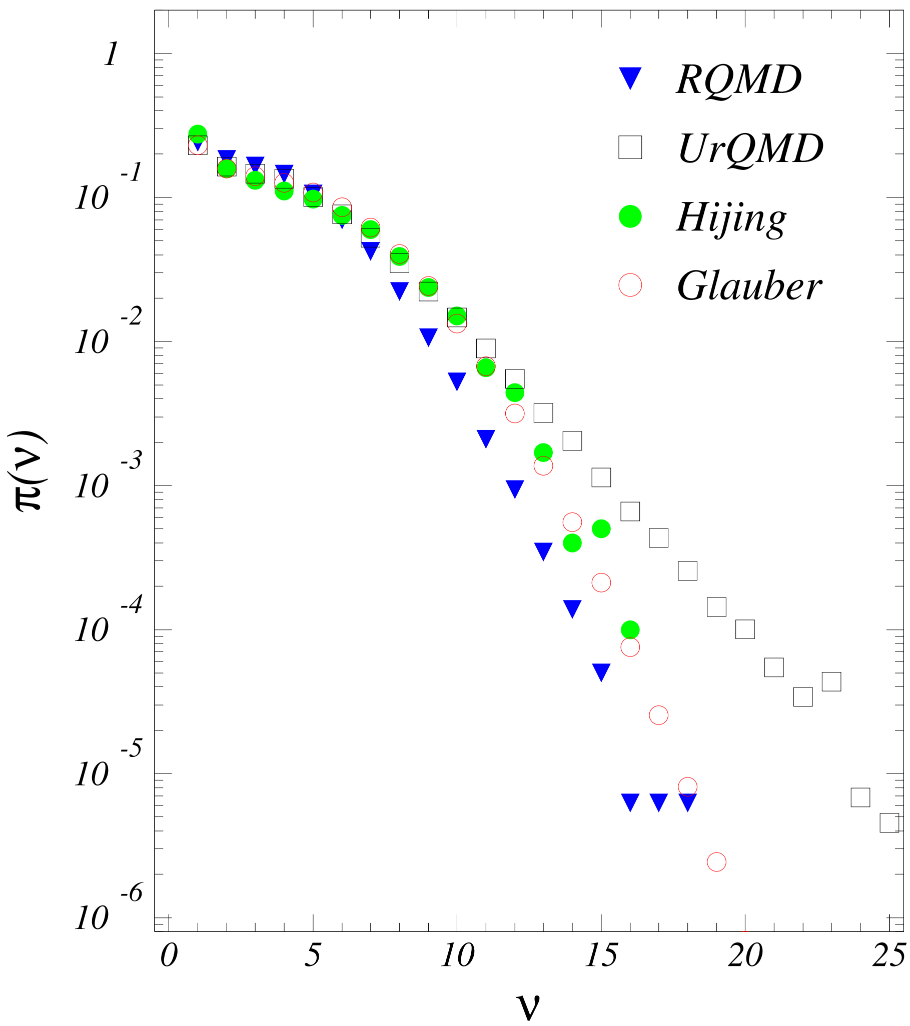

Figure A.1: RQMD ν distribution for Au nucleus compared to Glauber calculation and Hijing Model.

model and Glauber within the framework of Hijing (semi-log scale). The $\pi(\nu)$ distribution differs from the other models at large values of ν, but all are in reasonable agreement for smaller values of ν.

Appendix B

Extraction of $\overline{\nu}(N_g)$ for Scintillating Fiber Trigger Data

The scintillating fiber trigger data sets have slightly different grey particles multiplicity distributions than the bullseye trigger data sets. Therefore, the analysis to calculate $\overline{\nu}(N_g)$ using the Polynomial Model is performed on the scintillating fiber data sets relevant to the antiprotons analysis, the 18 GeV/c $p + Au$ and the 12 GeV/c $p + Au$, $p + Cu$, and $p + Be$ data. The results of the fits to $P(N_g)$ are shown in Fig. B.1 and the extracted values of $\overline{\nu}(N_g)$ are shown in Fig. B.2.

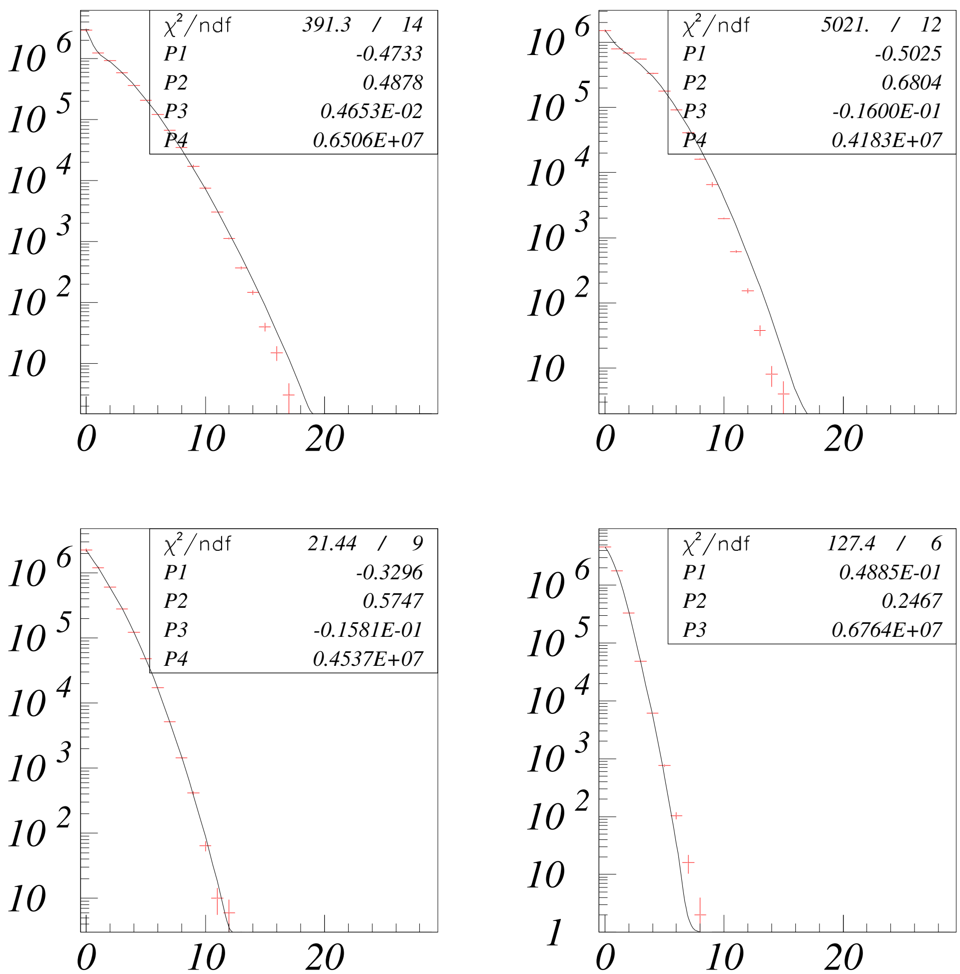

Figure B.1: Fits to N_g distributions for scintillating fiber trigger data sets. The top left panel is the 18 GeV/c $p + Au$ $P(N_g)$ dsitribution, the top right panel is 12 GeV/c $p + Au$, and the bottom panels are 12 GeV/c $p + Cu$ and $p + Be$, respectively.

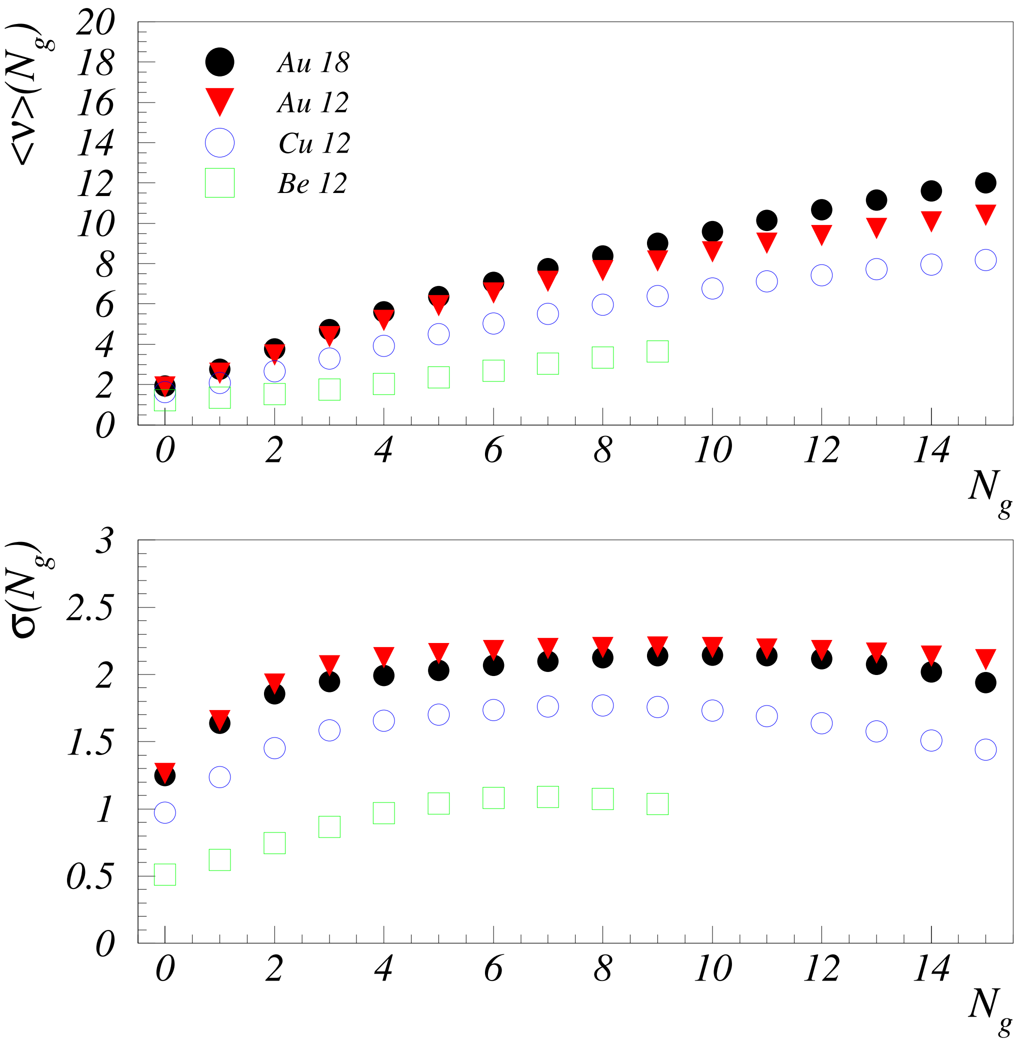

Figure B.2: Extracted $\bar{\nu}(N_g)$ for scintillating fiber trigger data sets.

Vita

Saskia Mioduszewski was born on March 7, 1972 in Jülich, Germany. She graduated from Oak Ridge High School, Oak Ridge, Tennessee, in June 1990. From August 1990 to May 1994, she attended North Carolina State University to study mathematics and physics. During the summer of 1992, she was first introduced to the field of relativistic heavy ion physics while working for Prof. Soren Sorensen simulating the motion of charged particles in a magnetic field for the PHENIX experiment. In the summer of 1993, Ms. Mioduszewski worked at Triangle Universities Nuclear Laboratory under the direction of Prof. Christopher Gould and Dr. Scott Wilburn developing a method to determine the concentration of SF_6 in a gas by measuring the speed of sound in the gas. She graduated with honors in 1994 with Bachelor of Science degrees in physics and mathematics.

In August 1994, she began her graduate studies in physics at the University of Tennessee and began Science Alliance Fellowship research with Prof. Kenneth Read. This research concerned simulations for the design of the Muon Identifier of the BNL PHENIX experiment.

Ms. Mioduszewski pursued doctoral research in experimental nuclear physics on BNL Experiment 910 analyzing slow proton production and antiproton production in proton-nucleus collisions. In 1998, she received the University of Tennessee Paul H. Stelson Fellowship awarded for her research in nuclear physics. Her thesis adviser was Prof. Kenneth Read. She received her doctoral degree in December

1999.

In January 2000, she will begin work in the Physics Department of Brookhaven National Laboratory as a postdoctoral research associate in the PHENIX group led by Dr. Samuel Aronson.